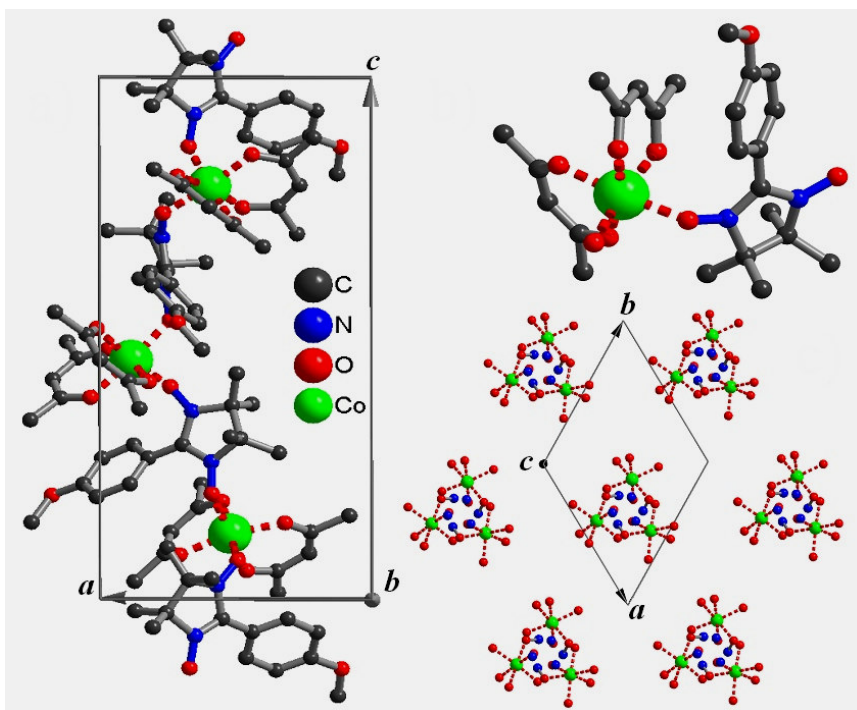


Spin Dynamics in One-Dimensional and Quasi One-Dimensional Molecular Magnets

Manuel Mariani



Supervisor: Prof. F. Borsa



Università
degli Studi
di Pavia

Dipartimento
di Fisica
“A. Volta”



DOTTORATO DI RICERCA IN FISICA – XX CICLO

Spin Dynamics in One-Dimensional and Quasi One-Dimensional Molecular Magnets

dissertation submitted by

Manuel Mariani

to obtain the degree of

DOTTORE DI RICERCA IN FISICA

Supervisors: Prof. F. Borsa, Prof. A. Lascialfari

Referee: Prof. A. Rettori (Dept. of Physics, University of Firenze)

Cover: Pictorial sketch of $\text{Co}(\text{hfac})_2\text{NITPhOMe}$ 1D molecular magnet with the indication of the atoms composing the sample.

**Spin Dynamics in One-Dimensional and Quasi One-Dimensional
Molecular Magnets**

Manuel Mariani

PhD thesis – University of Pavia

Printed in Pavia, Italy, December 2007

ISBN 978-88-95767-10-0

*To my parents,
to my brother
and to Linda*

*Ai miei genitori,
a mio fratello
e a Linda*

Table of Contents

1. Introduction	5
1.1 Low Dimensional Molecular Magnets	5
1.2 Thesis Outline	10
 2. Fundamental Aspects of NMR and μSR Techniques	 13
2.1 NMR	13
2.1.1 Introduction	13
2.1.2 NMR Pulsed Technique	17
2.1.3 Hamiltonian of Interaction	20
2.1.4 Spin-Lattice Relaxation Time(T_1)	23
2.1.5 Spin-Spin Relaxation Time(T_2)	26
2.2 μ SR	28
2.2.1 Introduction	28
2.2.2 Production and Decay of Muons	29
2.2.3 Experiments in Longitudinal and Transverse Fields	35
2.2.4 Depolarization Functions	38
2.2.5 μ SR Study of Magnetic Powder Systems	45
 3. One Dimensional Magnetic Systems and Models	 47
3.1 Introduction	47
3.2 1D Magnetic Systems	47
3.2.1 The Spin Hamiltonian Formalism	47
3.2.2 Spin Chains: General Properties	49
3.2.3 Spin Chains: Real Systems	52
3.2.4 Spin Dynamics in 1D Magnetic Systems	56
3.3 1D Magnetic Models	59
3.3.1 Glauber Kinetic Ising Model	59
3.3.2 Transfer Matrix Method	69
3.3.2.1 Application to the Ising Model	72
3.3.2.2 Application to the Planar Model in Zero Field	74

3.4 Frustrated Spin Systems	77
4. Pure and Zinc-Doped CoPhOMe	89
4.1 General Features	89
4.1.1 Introduction	89
4.1.2 Structure	90
4.1.3 Interactions and Electronic Configuration	93
4.2 Macroscopic Measurements on Pure CoPhOMe	95
4.2.1 Measurements in the Monomeric Compound	96
4.2.2 Susceptibility Measurements	97
DC Susceptibility	97
AC Susceptibility	99
4.2.3 Magnetization Decay Method	103
4.2.4 Isothermal Magnetization	105
4.3 NMR Measurements	108
4.3.1 Introduction	108
4.3.2 ^1H NMR Spectra	108
4.3.3 Spin-Spin Relaxation Time T_2	113
4.3.4 Spin-Lattice Relaxation Time T_1	116
4.4 μSR Measurements	119
4.5 Conclusions	123
4.6 Zinc-Doped CoPhOMe	125
4.6.1 Introduction	125
4.6.2 General Features	125
4.6.3 DC Susceptibility Measurements	127
4.6.4 AC Susceptibility Measurements	129
NMR MEASUREMENTS	136
4.6.5 Introduction	136
4.6.6 ^1H NMR Spectra	137
4.6.7 Spin Lattice Relaxation Rate T_1^{-1}	143
4.7 Conclusions	153
5. $\text{Gd}(\text{hfac})_3\text{NITR}$ Chains	157
5.1 $\text{Gd}(\text{hfac})_3\text{NITR}$	157

5.1.1	Introduction	157
5.1.2	Structural and Magnetic Properties	157
5.1.3	Hamiltonian and Model of Interpretation	162
5.1.4	DC Susceptibility Measurements	165
5.1.5	Specific Heat Measurements	167
5.2	Spin Dynamics	169
5.2.1	Gd(hfac) ₃ NITPh	169
	Specific Heat	169
	μSR	171
5.2.2	Gd(hfac) ₃ NITiPr	173
	Susceptibility	173
	Specific Heat	174
	μSR	178
5.2.3	Gd(hfac) ₃ NITet	181
	Susceptibility	181
	Specific Heat	182
	μSR	186
5.3	Conclusions	190
 General Conclusions		 197
 Appendix A		 203
A.1	NMR Pulsed Sequences	203
A.1.1	T ₂ Sequences	203
A.1.2	T ₁ Sequences	205
 Appendix B		 209
B.1	NMR Experimental Equipment	209
B.1.1	NMR Spectrometer	209
B.1.2	NMR Probe	210
B.1.3	Cryogenic Equipment	211
B.1.4	Field Source Equipment	215
B.2	μSR Experimental Equipment	219
B.2.1	Introduction	219

B.2.2 Muon Beamline and GPS Instrument	219
B.2.3 Cryogenic Equipment	222
B.2.4 Magnets in GPS Instrument	225
B.2.5 Computers	227
Bibliography	229
Aknowledgements	239
Ringraziamenti	241

CHAPTER 1

Introduction

1.1 Low-Dimensional Molecular Magnets

The interest in magnetism and in *low-dimensional systems* has been always strong although, in the course of the years, the focus of the interest has changed many times. In fact, at the beginning, these kinds of systems were studied both from a theoretical and an experimental point of view, because they afforded a model system of many body problems which could be treated and understood in a relatively simple way. Later, researchers realized that low-dimensional systems possessed peculiar properties not present in higher dimensionality systems such as, for instance, magnetic soliton excitations, quantum critical point and the slowing down of the magnetization for 1D chains predicted by Glauber [1] for *Ising spin chains*, the last being one of the subjects of the present thesis.

This great theoretical ferment was not immediately followed by an experimental development; in fact many theoretical predictions formulated could not be immediately verified experimentally due to lack of real systems approximating the low-dimensional case. These predictions served as a stimulus to chemists in researching new methods for synthesizing compounds with the new desired characteristics. Nowadays many techniques have been improved and, starting from 70s, a lot of *1D*, *quasi-1D* and *2D systems* are available. Chemists even have been able to confine magnetic interactions in *zero-dimensional structures*.

Among the most investigated low-dimensional magnetic structures there are the *molecular clusters* (see for instance [2-7]): they consist of crystals constituted by large organic

1. Introduction

molecules containing several transition metal ions with strong exchange interaction among them. In these systems each molecule is not affected by the magnetic interaction with the surrounding ones so that a molecule behaves as a *single molecule magnet* (SMM) i.e. a model system of zero-dimensionality. Of particular interest are SMM which have a large total spin ground state and a high single axis anisotropy. As a result the two degenerate ground states corresponding to opposite projections of the magnetic moment along the anisotropy direction are separated by a large energy barrier. At low temperatures, when thermal energy is not sufficient for overcoming this barrier, the system behaves as a *superparamagnet*. The magnetic freezing suggested the possibility of using SMM as memory storage bits: however, up to now no system with sufficiently high anisotropy for room temperature applications has been discovered. Even without applications, SMM have offered a model system for study of many fascinating new phenomena involving both classical and quantum effects such as slowing down of the magnetization, molecular magnetic hysteresis [8], Berry phase [9] and quantum tunnelling of the magnetization [10-11]. The efforts generated in chemical synthesis made available a large number of quasi-one-dimensional systems, where the interactions between spins are restricted mostly in one dimension, so that they undergo a 3D transition only at very low temperatures when the very weak interchain interactions are no longer negligible. One of the most important and studied systems synthesized is the so-called TMMC [12-16], acronym for the $[(\text{CH}_3)_4\text{N}]\text{MnCl}_3$ compound, which consists in an antiferromagnetic chain with spin $S=5/2$ which develops along c crystallographic axis. This system is made up of Mn^{2+} ions and $(\text{CH}_3)_4\text{N}^+$ centres: the former are responsible for the magnetic behaviour of the compound while the latter serve for separating neighbour chains. This

1. Introduction

sample is a quasi-ideal 1D system thanks to the fact that the distance between two Manganese ions along the chain is of about 3.25Å, while the interchain distance is 9.15Å: the result is that the ratio between interchain and intrachain interactions is of the order of 10^{-4} and, as a consequence, the 3D transition occurs at very low temperature ($T_N \cong 0.8\text{K}$).

A fundamental step was taken in the last twenty years with the discovery of new techniques and materials for the synthesis of new samples which are quasi-1D: ligands particularly important for this purpose have been and still are *nitronyl-nitroxide* stable *organic radicals* which, despite their lability, have made possible a new synthesis approach: in fact the new 1D and quasi-1D systems are characterized by the alternation of transition-metal or lanthanide ions and the radical *building blocks*. The results have been amazing: in fact with the substitution of the radical in these centres, the properties of these systems change completely. One of the most important example is provided by the so-called Dysprosium chains: this compound is constituted by the alternation of Dysprosium ions and of the mentioned nitronyl-nitroxide radical centres. It has been demonstrated that working on the radical inserted in these building blocks it is possible, for instance, to obtain from a quasi one-dimensional system like $[\text{Dy}(\text{hfac})_3\{\text{NIT}(\text{Et})\}]$ [17-20], where the shortest interchain distance is of about 10.76Å and with a 3D transition temperature $T_N \cong 4.3\text{K}$, a compound like $[\text{Dy}(\text{hfac})_3\{\text{NIT}(\text{C}_6\text{H}_4\text{OPh})\}]$ [21]. The latter can be considered a *single chain magnets* (SCM) where theoretically $T_N = 0$, since the position of the ligands permits a larger separation between neighbour chains of the sample. This opens up new perspectives in the search of ideal one-dimensional systems: the starting point are quasi-one dimensional magnets which can be simply manipulated in their radical centres for the creation of new single chain magnets.

1. Introduction

Thanks to the deep knowledge of the properties of these radicals and of their interactions with the magnetic centers, chemists in Firenze could also create a family of rare-earth-based single chain magnets whose general formula is $[M(\text{hfac})_3\text{NITPhOPh}]$ [22] where $M=\text{Eu, Gd, Tb, Dy, Ho, Er, Yb}$. With the substitution of the magnetic centre they have been able to control the anisotropy of each system and to point out the different magnetic properties for compounds which are similar from a topological point of view.

Also in this thesis we will discuss two systems which display a different magnetic behaviour although the systems are similar from a chemical point of view. The first sample studied is $[\text{Co}(\text{hfac})_2\text{NITPhOMe}]$ [23] which has been synthesized at the end of the 80s by the Dante Gatteschi's group in Firenze. It presents the characteristics already observed for single molecule magnets [24], i.e. the molecular clusters discussed before: in fact this compound is characterized by the slowing down of the magnetization and it has been the first system displaying the Kinetic Ising Model of Glauber [1] predicted theoretically almost thirty years before for 1D Ising systems. An issue of considerable interest is the study of the Glauber dynamics in chains broken into finite segments by doping with diamagnetic impurities. With this aim in mind we have investigated, by means of DC susceptibility and NMR measurements, Zinc-doped ($\text{Zn}=1.9\%, 5.4\%$) powder samples in the temperature range $1.5\text{K}<\text{T}<300\text{K}$ in two different static applied magnetic fields ($H=0.35\text{T}; 1.65\text{T}$). The second kind of samples investigated consists in a family of *quasi-one dimensional helical frustrated systems*, whose chemical formula is $[\text{Gd}(\text{hfac})_3\text{NITR}]$ where $\text{R}=\text{Me, Ph, iPr, Et}$. They have been studied in collaboration with the University of Firenze and the University of Modena. In this work we have focussed our attention on Gd-Ph, Gd-iPr and Gd-Et derivatives.

1. Introduction

In particular we have performed, in the temperature range where the phase transitions were supposed to occur ($20\text{mK} < T < 100\text{K}$), susceptibility measurements in a vanishing field and, for the first time on this kind of samples, μSR measurements in Zero and in 500Oe longitudinal fields.

These compounds have been synthesized thanks to development of innovatory synthesis techniques which allowed a great control on interchain and intrachain distances and the possibility to introduce different kinds of anisotropies, depending on the magnetic centre inserted in the compounds, with the creation of systems characterized by several competing interactions. Also in this case, even if many scientists have studied in the past these systems from a theoretical point of view, no real sample was available before these complex compounds were synthesized. The most important theorists who studied these materials, have been, in the last thirty years, I. Harada [25-27] and J. Villain [28-29]. They examined quasi-one dimensional systems where the order of magnitude of the intrachain interactions is the same. They had to take into account the competitions between nearest-neighbour and next-nearest-neighbour exchange interactions evaluating the degree of frustration of each system and found out in these materials many new features such as *excitations of domain walls* separating regions with opposite chirality (Harada [25-27]) and the presence of a *chiral phase* between the paramagnetic one and the *3D helical long range phase* (Villain [28-29]). The family of quasi one-dimensional systems cited above and studied in this thesis, is one of the best example of frustrated helimagnetic systems. In fact these compounds are characterized by nearest-neighbour interactions and two different next-nearest-neighbour interactions: depending on the strength of the magnetic interactions, together with the influence of the intrachain dipolar interactions, these compounds can be divided

1. Introduction

into “*weakly frustrated*” systems (Gd-Ph and Gd-Me derivatives), which are characterized simply by a 3D transition of ferromagnetic nature and into “*fully frustrated*” systems, which fulfil Villain’s complex phase diagram [28-29].

1.2 Thesis Outline

Following the introductory chapter, the work is organized in four additional chapters and two appendices.

In Chapter 2 we will describe the NMR and μ SR experimental techniques, which have been the main tool of investigation we have adopted for the study of the samples treated in this thesis.

In Chapter 3 we will treat the most important theoretical methods and models for one-dimensional and quasi one-dimensional systems used for the interpretation of the experimental results. Among them we will describe Transfer Matrix Method applied to Ising Model and Planar Model in Frustrated Systems and Glauber Model for Ising spin chains.

In Chapter 4 the *CoPhOMe* single chain magnet will be investigated: after a summary of the physical characteristics and the experimental results obtained previously on pure sample, we will emphasize Zinc-doped samples which have been studied here for the first time also from a microscopic point of view for the purpose of comparing their magnetic properties with the ones of the pure compound.

In Chapter 5 we will discuss the complex features of the *Gadolinium-Radical chains* with a comparison among the four derivatives of this family with the corresponding classification in “weakly frustrated” and “fully frustrated” systems and some conclusions will be drawn regarding the results obtained in this work.

Finally in Appendix A the most used sequences in NMR pulse

1. Introduction

technique both for T_1 and T_2 measurements will be explained, while in Appendix B NMR and μ SR experimental equipment used in laboratories of University of Pavia and of Paul Scherrer Institute in Villigen (CH), respectively, will be described.

CHAPTER 2

Fundamental Aspects of NMR and μ SR Techniques

In this Chapter the fundamental aspects regarding NMR and μ SR techniques, used for low-dimensional systems investigation, will be given.

2.1 NMR

2.1.1 Introduction

Nuclear Magnetic Resonance technique can be described from two main different points of view: through a semi-classical theory and through a quantum theory. For an introduction to the subject, vectorial semi-classical description will be used.

Most of the nuclei in their ground state present a *nuclear spin* angular momentum $\vec{I}\hbar$ different from zero and a corresponding *dipole magnetic moment* $\vec{\mu} = \gamma\vec{I}\hbar$ where γ is the *gyromagnetic ratio* of the nucleus. Let us consider an *isolated free spin* subject to a *static and uniform magnetic field* $\vec{H} = H_0\hat{z}$ applied along z direction of a fixed reference frame called *laboratory reference frame* (Σ_{LAB}).

The purpose of this section is to investigate the time evolution of the magnetic moment under the influence of the uniform static magnetic field \vec{H}_0 : the equation to be solved is [30]

$$d\vec{\mu}/dt = \gamma\vec{\mu} \wedge \vec{H}_0 \quad (2.1)$$

2. Fundamental Aspects of NMR and μ SR Techniques

which describes the reaction of the magnetic moment to the moment of the forces acting on it.

Projecting the equation along the Cartesian axes, the result is

$$d\mu_x / dt = \gamma H_0 \mu_y \quad (2.2a)$$

$$d\mu_y / dt = -\gamma H_0 \mu_x \quad (2.2b)$$

$$d\mu_z / dt = 0. \quad (2.2c)$$

These equations clearly show that magnetic moment precesses around z direction, where magnetic field is applied, with a frequency $\omega_L = \gamma H_0$ called *Larmor frequency*.

Now let's take into account the effect of a *Radio Frequency (RF) Field* \vec{H}_1 rotating with frequency ω in the x - y plane of Σ_{LAB} , i.e. perpendicular to the static magnetic field direction.

The RF field \vec{H}_1 can be generated by a coil (oriented for instance along x direction in Σ_{LAB}) in which an alternate electrical current at radio frequency flows, creating an oscillating field. This field can be considered as the sum of two rotating fields clockwise and counterclockwise respectively. When the so-called *resonance conditions* are reached, the component rotating with frequency equal to $-\omega_L$ can be neglected, because it is so far from the resonance frequency that its effect on the precession of the magnetic moment is really weak.

We assume in the following that the RF field must have intensity much smaller than the static magnetic field i.e.:

$$|\vec{H}_1| \ll |\vec{H}_0| \quad (2.3)$$

2. Fundamental Aspects of NMR and μ SR Techniques

For a better understanding of the system under discussion it is useful to introduce a new frame of reference, named Σ_{ROT} , x' , y' , z' with $z'=z$, and rotating with the same frequency ω as the RF field \vec{H}_1 . Working in Σ_{ROT} the time evolution equation becomes

$$d\vec{\mu}/dt = \gamma\vec{\mu} \wedge (\vec{H}_0 + \vec{\omega}/\gamma + \vec{H}_1) \quad (2.4)$$

The use of a *non-inertial reference frame* causes the introduction of an *effective field*: eq.(2.4) has the same form as eq.(2.1) if we assume as effective field

$$\vec{H}_{\text{eff}} = \vec{H}_0 + \vec{\omega}/\gamma + \vec{H}_1 \quad (2.5)$$

so that eq.(2.4) becomes

$$d\vec{\mu}/dt = \gamma\vec{\mu} \wedge \vec{H}_{\text{eff}} \quad (2.6)$$

When the rotational frequency is $\vec{\omega} = \vec{\omega}_L = -\gamma\vec{H}_0$, the *resonance conditions* are reached and the only field felt by nuclear moments in the rotating frame is \vec{H}_1 , with a subsequent precession around \vec{H}_1 of the nuclear magnetization. Working on \vec{H}_1 the relative position between $\vec{\mu}$ and $z=z'$ axis can be varied.

This procedure describes the main principle of NMR technique: thanks to an oscillating field at radio frequency, caused by a RF current, a free spin in a uniform magnetic field \vec{H}_0 can be driven in different positions in the space.

Let's consider now an ensemble (for instance of the order of the *Avogadro number*), of *non-interacting nuclei* of the same species, interacting with the lattice and subject to a uniform static magnetic field \vec{H}_0 along z axis.

2. Fundamental Aspects of NMR and μ SR Techniques

From a quantum point of view as a consequence of the presence of \vec{H}_0 the levels degeneracy will be split and the spins will arrange themselves on the *Zeeman levels* whose energy is $E_{m_I} = -\hbar m_I H_0$ where $m_I = I, I-1, \dots, -I+1, -I$. Once the thermal equilibrium is reached, spin arrangement will obey *Maxwell-Boltzmann statistics*, and a nuclear magnetization results. This is related to the fact that most of the magnetic moments of nuclei will arrange themselves along field direction: magnetization value is $M = (N/V) \langle \mu_z \rangle$, with $\langle \mu_z \rangle$ representing the thermal mean value of the component of the magnetic moment along field direction and N the number of the spins considered.

After easy calculations [30] the expression of the magnetization for a paramagnetic system is

$$M = \frac{N}{V} g \mu_B I B_I \left(\frac{g \mu_N I H_0}{k_B T} \right) \quad (2.7)$$

where $B_I = (2I+1)/(2I) \text{ctnh}[(2I+1)x/2I] - 1/(2I) \text{ctnh}[x/(2I)]$, with $x = g \mu_N I H_0 / (k_B T)$, is the *Brillouin Function*, g the *nuclear Landé factor*, $\mu_N = 5.0508 \cdot 10^{-24}$ erg/gauss the *nuclear magneton* and $k_B = 1.380662 \cdot 10^{-16}$ erg/K is the *Boltzmann constant*.

If $\hbar H_0 \ll k_B T$, a condition verified in most cases, and $I=1/2$, the magnetization can be written

$$M = \frac{N}{V} \frac{\mu^2}{3 k_B T} H_0 \quad (2.8)$$

which is the classical result, with $\mu^2 = g^2 \mu_N^2 I(I+1)$.

Let us now study the time evolution of the nuclear magnetization in Σ_{LAB} when the *Zeeman levels* populations are perturbed by the

2. Fundamental Aspects of NMR and μ SR Techniques

application of the RF field. The result consists in the so-called *Bloch Equations* [30]

$$dM_x / dt = \omega_L M_y + \omega_1 M_z \sin(\omega t) - M_x / T_2 \quad (2.9a)$$

$$dM_y / dt = -\omega_L M_x + \omega_1 M_z \cos(\omega t) - M_y / T_2 \quad (2.9b)$$

$$dM_z / dt = -\omega_1 M_x \sin(\omega t) + \omega_1 M_y \cos(\omega t) - M_z / T_1 \quad (2.9c)$$

with $\omega_L = \gamma H_0$ and $\omega_1 = \gamma H_1$.

In the equations above, where it has been supposed that M_z reaches this value with a rate proportional to the distance from it, $M_0 = \chi_0 H_0$ is the equilibrium value of the magnetization. In the phenomenological *Bloch Equations* T_1 and T_2 quantities have been introduced: they are named respectively *spin-lattice relaxation time* and *spin-spin relaxation time*. These two quantities represent the times it takes to reach the equilibrium conditions. In particular T_1 measures how fast the longitudinal (z) component of the nuclear magnetization reaches its equilibrium value M_0 , instead T_2 represents the rate the transverse components takes (x, y) to decay to zero. These are the physical properties mainly investigated in NMR technique, because they give many information on the system studied as will be shown later in the text.

2.1.2 NMR Pulsed Technique

After the application of the uniform steady magnetic field \vec{H}_0 , m_I degeneracy of Zeeman nuclear levels is removed and the sample is characterized by a measurable magnetization along the field direction. NMR pulsed technique is based on the application

2. Fundamental Aspects of NMR and μ SR Techniques

of one or more RF pulses close to the resonance frequency ω_L and on the subsequent detection of the response of the nuclear magnetization. The spin system is driven out of equilibrium by applying the RF pulse for a time τ of the order of microseconds. The pulse length sets the position of the magnetization in space: for instance the pulse is named $\pi/2$ if after $\tau = (\pi/2)(1/\gamma H_1)$ the magnetization is rotated by an angle $\pi/2$ from its initial position along z axis (i.e. in the x - y plane). Another common angle used is π and the magnetization is subsequently reversed in the negative direction of z axis.

After the RF pulse, the same coil used for the generation of \vec{H}_1 ,

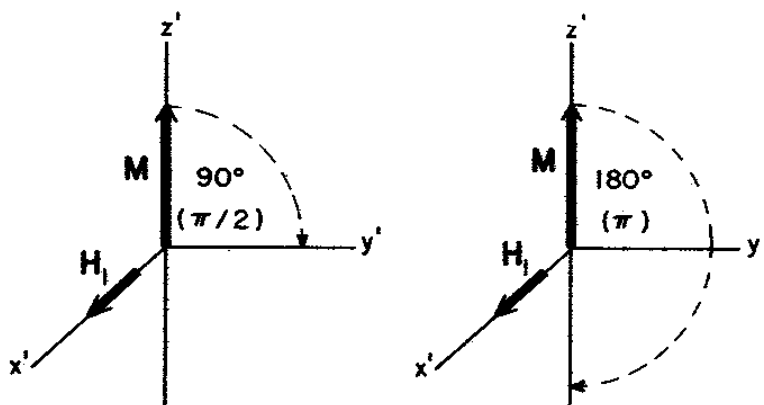


FIG.2.1 Trajectories of nuclear magnetization after $\pi/2$ and π RF pulses.

placed perpendicularly to the static magnetic field direction, detects the signal created by the transverse components of the magnetization. The signal consists in an *electromotive force* induced in the coil caused by a variation of the flux linkage to the

2. Fundamental Aspects of NMR and μ SR Techniques

coil itself. This signal, called *Free Induction Decay* (FID), is then filtered, amplified and displayed by the spectrometer.

As can be inferred by the third Bloch Equation (2.9c) [30] the restoration of the equilibrium value of M_z is expressed by

$$M_z(t) = M_0[1 - \exp(-t/T_1)]. \quad (2.10)$$

The recovery of the nuclear magnetization can also be obtained from a quantum mechanical treatment of the problem in terms of transition probabilities among Zeeman nuclear levels and a master equation approach to describe the dynamics [31]. For $I = 1/2$ one finds an exponential recovery as in eq.(2.10). If $I > 1/2$ eq.(2.10) is replaced by a weighted linear combination of exponential functions which must be obtained through the solution of the so-called *Master Equations* [31] of the form:

$$\frac{dN_n}{dt} = W_{m \rightarrow n} N_m - W_{n \rightarrow m} N_n \quad (2.11)$$

for each couple of levels mn . The *Master Equations* represent the population variation on the nuclear hyperfine levels caused by the irradiation due to the electromagnetic RF field.

In the equation above, W is the probability transition between levels considered, while N represents the levels populations.

The reason of the more complex behaviour is due to the fact that Zeeman levels are not equally spaced, because of the perturbation of the electric quadrupolar interaction, which characterizes nuclei with $I > 1/2$. Under this condition there are many cases to be taken into account depending on many factors. A discriminant parameter consists, for instance, in the selection rules driving the magnetic interactions in the system studied; in fact a system undergoing interactions characterized by magnetic

2. Fundamental Aspects of NMR and μ SR Techniques

interactions with selection rules $\Delta m = \pm 1$ must be treated differently with respect to the case when both $\Delta m = \pm 1$ and $\Delta m = \pm 2$ are present, since in this case the recovery of the nuclear magnetization is even much more complicated [31].

As regards the transverse component of the nuclear magnetization, spins are driven to their equilibrium value by the characteristic time T_2 which is shorter or of the same order as T_1 : again from Bloch Equations [30] results

$$M_{\perp}(t) = M_{\perp} \exp(-t/T_2) \quad (2.12)$$

which describes the decay to zero of the transverse magnetization, where M_{\perp} is the initial value of magnetization in the x - y plane.

2.1.3 Hamiltonian of Interaction

In this section the connection between the relaxation parameters described above and the microscopic properties of the system will be shown.

The time evolution of nuclear magnetization is driven by various kinds of hyperfine interactions which act over the ensemble of the nuclei. In general the contributions in the Hamiltonian of the system are four and can be summed up by the total Hamiltonian

$$H = H_Z + H_{nm} + H_{ne} + H_Q \quad (2.13)$$

where

$$H_Z = -\gamma \hbar \sum_j \vec{I}_j \cdot \vec{H}_0 \quad (2.14)$$

is the *Zeeman Hamiltonian* where \vec{I}_j is the j -th nuclear spin, H_{nm}

2. Fundamental Aspects of NMR and μ SR Techniques

represents the *dipolar interactions* between nuclear magnetic moments while

$$H_{ne} = \sum_j H_{ne}^j = \sum_j \sum_i \vec{I}_j \cdot \vec{\bar{A}}_{ji} \vec{S}_i \quad (2.15)$$

describes the *interaction between nuclear and electronic spins* surrounding each nucleus where H_{ne}^j is the Hamiltonian related to nucleus at the j -th site.

In this case the *Hyperfine tensor* $\vec{\bar{A}}_{ij}$ is supposed to be the sum of a dipolar contribution and a *contact scalar term* A'_{ij} with $[A'_{ij}, H_z] = 0$. The total expression of the Hyperfine tensor is

$$\vec{\bar{A}}_{ji} = -\gamma_n \gamma_e \hbar^2 \left(\frac{r_{ji}^2 \vec{\bar{I}} - 3 \vec{r}_{ji} \cdot \vec{r}_{ji}}{r_{ji}^5} \right) - A'_{ji}, \quad (2.16)$$

where $\vec{\bar{I}}$ is the identity tensor.

The first contribution in eq.(2.16) has a classical origin and it can be thought as the classical interaction between two magnetic dipoles localized at a relative distance \vec{r} . The second term instead, called also *Fermi term*, has a quantum origin: it represents the interaction between I and the component s of the electronic wavefunction, which has a probability of presence $|\psi_s(0)|^2$ different from zero also at the nucleus position. This interaction is proper of a system with delocalized electrons but also for localized electrons in the case when external s levels of the ion which I belongs to, are polarized.

Let us introduce now the *hyperfine field* defined as

$$\vec{h}_j = \left(\frac{1}{\gamma_n \hbar} \right) \sum_i \vec{\bar{A}}_{ji} \cdot \vec{S}_i \quad (2.17)$$

2. Fundamental Aspects of NMR and μ SR Techniques

which represents the field created by electrons and felt at nuclear sites. The interactions between nuclei and electrons can be rewritten

$$H_{ne}^j = -\gamma_n \hbar \vec{I}_j \cdot \vec{h}_j \quad (2.18)$$

in a form that reminds an effective Zeeman interaction.

Dipolar interaction among nuclei is much weaker than nucleus-electrons interaction ($\gamma_n / \gamma_e \cong 10^{-3}$) and can be written

$$H_{nn} = \sum_{i < j} \vec{I}_j \vec{\vec{D}}_{ji} \vec{I}_i \quad (2.19)$$

with

$$\vec{\vec{D}}_{ji} = \gamma_n \gamma_n \hbar^2 \left(\frac{r_{ji}^2 \vec{\vec{I}} - 3 \vec{r}_{ji} \cdot \vec{r}_{ji}}{r_{ji}^5} \right). \quad (2.20)$$

H_{nn} is the responsible for a broadening of the absorption line called homogeneous.

The contribution just described is the so-called *direct dipolar interaction* between two nuclei characterized by a different spin I : this term is relevant especially when the protons of a system are studied, as in our case (see Chapter 4), since they have a high gyromagnetic ratio γ . It is possible also another kind of nucleus-nucleus interaction, called *indirect dipolar interaction*: it consists in an effective interaction which uses as intermediaries the electrons. In practice a nucleus I polarizes the electronic system through hyperfine coupling, a spin in the n -th site interacts through exchange interaction J with another electronic spin at m -th site, which, in its turn, polarizes another nucleus still through hyperfine interactions.

2. Fundamental Aspects of NMR and μ SR Techniques

In practice two nuclei can interact in two different ways: if (i) the hyperfine coupling among them is strong enough and if (ii) two nearest-neighbour electronic spins are strongly coupled.

The fourth term in the general Hamiltonian of Interaction is related to systems whose nuclei have $I > 1/2$ and thus possess an *electric quadrupole moment*.

The interaction between electric quadrupole moment and *electric gradient field tensor* $\vec{\vec{V}}$, related to charge distribution around each nucleus, is described by [32]

$$H_Q^j = \frac{h\nu_Q}{2} \left[I_z^2 - \frac{I(I+1)}{3} + \frac{\eta}{6} (I_+^2 + I_-^2) \right] \quad (2.21)$$

where

$$\nu_Q = \frac{3e^2QV_{zz}}{2I(2I-1)h} \quad (2.22)$$

is the *quadrupolar frequency*, $I_+ = I_x + iI_y$ and $I_- = I_x - iI_y$, $V_{\alpha\beta} = \partial^2 V / \partial x_\alpha \partial x_\beta$ are the components of the $\vec{\vec{V}}$ tensor in a reference frame where $|V_{zz}| \geq |V_{yy}| \geq |V_{xx}|$; $\eta = (V_{xx} - V_{yy})/V_{zz}$ is named *asymmetry parameter*.

2.1.4 Spin-Lattice Relaxation Time (T_1)

In this paragraph and in the following one *relaxation times* measured in NMR experiments will be discussed from a theoretical point of view making use of quantum theory.

As already mentioned, the *spin* ensemble after the RF pulse is not in an equilibrium condition. In the case of nuclei with $I = 1/2$,

2. Fundamental Aspects of NMR and μ SR Techniques

calling W the transition probabilities between $|+\rangle = |m_I = +1/2\rangle$ and $|-\rangle = |m_I = -1/2\rangle$, *spin-lattice relaxation time* T_1 is defined, from Master Equations [31] as [33]

$$\frac{1}{T_1} \equiv 2W. \quad (2.23)$$

The most important effect on spin-lattice relaxation rate is due to the hyperfine interaction between nuclei and electronic spins and referred as H_{ne} in the Hamiltonian of interaction previously described. Taking into account the fluctuations of the hyperfine field at the nucleus due to these interactions and treating them theoretically with time-dependent perturbation theory, $1/T_1$ expression can be written [34-35] in the form

$$\frac{1}{T_1} = 2W = \frac{\gamma^2}{2} \int_{-\infty}^{+\infty} dt e^{i\omega_0 t} \langle \{h_+(t), h_-(0)\} \rangle \quad (2.24)$$

In the equation above, $\omega_0 = \mathcal{H}_0$ is the resonance frequency, $h(t)$ represents the fluctuating part of the hyperfine magnetic field, $h_{\pm} = h_x + ih_y$, $\{A, B\} = (AB + BA)/2$ is the anticommutator of A and B operators and $\langle \rangle$ is the statistical average.

In particular:

$$\langle h_+(t), h_-(0) \rangle = \text{Tr} \left\{ e^{-\beta H_e} e^{itH_e/\hbar} h_+ e^{-itH_e/\hbar} h_- \right\} / \text{Tr} \left(e^{-\beta H_e} \right) \quad (2.25)$$

where H_e is the Hamiltonian of the electronic system. Making the anticommutator explicit, results

$$\frac{1}{T_1} = 2W = \frac{\gamma^2}{2} \int_{-\infty}^{+\infty} dt e^{i\omega_0 t} \left(\langle h_x(0), h_x(t) \rangle + \langle h_y(0), h_y(t) \rangle \right) \quad (2.26)$$

2. Fundamental Aspects of NMR and μ SR Techniques

This equation shows that just the transverse component of the fluctuating field at nuclei is responsible for spin-lattice relaxation: this behaviour derives from the magnetic dipole selection rules.

Writing

$$\vec{h}(t) = \vec{A} \vec{S}(t) \quad (2.27)$$

and expressing the time evolution of the spin $\vec{S}(t)$ in terms of collective components $\vec{S}_{\vec{q}}(t)$

$$\vec{S}(t) = \frac{1}{\sqrt{N}} \sum_{\vec{q}} e^{i\vec{q} \cdot \vec{r}} \vec{S}_{\vec{q}}(t) \quad (2.28)$$

where the number of spins is indicated with N and \vec{q} is a vector of the first Brillouin zone, the fluctuating hyperfine field becomes

$$\vec{h}(t) = \frac{1}{\sqrt{N}} \sum_{\vec{q}} \vec{A} e^{i\vec{q} \cdot \vec{r}} \vec{S}_{\vec{q}}(t) \quad (2.29)$$

and $1/T_1$ can be written

$$\frac{1}{T_1} = \frac{\gamma^2}{2} A^2 \int_{-\infty}^{+\infty} dt e^{i\omega t} \sum_{\vec{q}} \left\{ \langle S_{\vec{q}}^x(0), S_{-\vec{q}}^x(t) \rangle + \langle S_{\vec{q}}^y(0), S_{-\vec{q}}^y(t) \rangle \right\}. \quad (2.30)$$

Defining the components of the dynamical structure factor as

$$S^{\alpha\alpha}(\vec{q}, \omega) = \int_{-\infty}^{+\infty} dt e^{i\omega t} \langle S_{\vec{q}}^{\alpha}(0), S_{-\vec{q}}^{\alpha}(t) \rangle, \quad (2.31)$$

where $\alpha = x, y, z$, results

2. Fundamental Aspects of NMR and μ SR Techniques

$$\frac{1}{T_1} = \frac{\gamma^2}{2} A^2 \sum_{\vec{q}} [S^{xx}(\vec{q}, \omega_0) + S^{yy}(\vec{q}, \omega_0)]. \quad (2.32)$$

The quantity $S^{xx}(\vec{q}, \omega)$ is proportional to the component xx of the imaginary part of the susceptibility $\chi''_{xx}(\vec{q}, \omega)$; under the condition $\hbar \omega_0 \ll k_B T$, which represents the high temperature limit, the equation for $S''_{xx}(\vec{q}, \omega_0)$ is

$$S(\vec{q}, \omega_0) = \frac{k_B T}{\hbar \omega_0} \chi''(\vec{q}, \omega_0) \quad (2.33)$$

The final expression for spin-lattice relaxation time is thus:

$$\frac{1}{T_1} = 2W = \frac{\gamma^2}{2} A^2 \frac{k_B T}{\hbar \omega_0} \sum_q \chi''_{\perp}(\vec{q}, \omega_0) \quad (2.34)$$

where the symbol \perp means that just the transverse (x, y) components are considered.

2.1.5 Spin-Spin Relaxation Time (T_2)

Spin-spin relaxation time T_2 measures the irreversible decay of the transverse magnetization. The measure of T_2 can be done only after the use of specific *spin echo sequences* which are able to eliminate the reversible contribution to the decay of the transverse magnetization which arises from inhomogeneous broadening effects. (See Appendix A)

Considering again relaxation processes due to hyperfine field fluctuations at the nuclear sites one has (see for instance [36]):

$$\frac{1}{T_2} = \gamma^2 \left[\frac{1}{2} J_{zz}(0) + \frac{1}{4} J_{\pm}(\omega_0) \right] \quad (2.35)$$

2. Fundamental Aspects of NMR and μ SR Techniques

where $J_{zz}(0)$ is the *spectral density* at zero frequency and it is defined:

$$J_{zz}(0) = \int_{-\infty}^{+\infty} \langle h_z(t), h_z(0) \rangle dt. \quad (2.36)$$

Making explicit the expression of the spectral density as follows

$$J_{\pm}(\omega_0) = \int_{-\infty}^{+\infty} \langle h_{\pm}(t), h_{\pm}(0) \rangle e^{i\omega_0 t} dt \quad (2.37)$$

results also:

$$\gamma^2 / 4J_{\pm}(\omega_0) = 1/(2T_1) \quad (2.38)$$

It must be remarked that this treatment of spin-spin relaxation rate as a function of spectral density $J(\omega)$, is valid only in the so-called *fast motions regime*, i.e. when the hyperfine coupling or the nuclear dipolar coupling fluctuates faster with respect to the energy scale of the interaction itself (in frequency units). In the *slow motions regime* case, i.e. when the “lattice” is rigid, T_2 cannot be defined from Bloch Equations [30], predicted mainly for fluids, but *Redfield theory* [37] must be used. In the case of a *rigid lattice* one can still define a spin-spin relaxation time T_2 through the second moments of the resonance line. In this case one speaks of a *nuclear dipolar contribution* $(1/T_2)_{\text{dip}}$.

2. Fundamental Aspects of NMR and μ SR Techniques

2.2 μ SR

2.2.1 Introduction

In this work μ SR spectroscopy has been used as a tool to obtain information on *local spin dynamics* (muons are local probe contrarily to what happens in the measurements of quantities like χ or C/R), complementary to the ones obtained by means of NMR spectroscopy.

μ SR (Muon Spin Rotation or Relaxation) was developed after the discovery of *parity violation in muon decay* (1957) by Garwin, Ledermann and Weinrich. It makes use of μ^+ as local probe to investigate the microscopic properties of the system, in fact this particles, of the family of Leptons, are sensitive to very low magnetic fields (till $\sim 10^{-5}$ T), both static and fluctuating and thus they are useful to understand structural, dynamic and magnetic properties of the physical systems. The main characteristics of the muons are:

- 1) $S=1/2$
- 2) $q=\pm e$
- 3) $\gamma_\mu/2\pi=13.5\text{kHz} \cdot \text{G}^{-1}$
- 4) $m_\mu=207m_e$

μ SR experiments can be performed in *longitudinal or transverse geometrical configuration* with magnetic fields applied parallel or perpendicular to the direction of muon polarization

2. Fundamental Aspects of NMR and μ SR Techniques

($\vec{P}_\mu = \sum_i \vec{m}_i$ with \vec{m}_i the muon magnetic moments). The muon

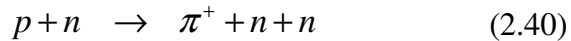
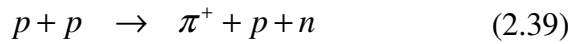
sources for μ SR experiments can be either pulsed or continuous, depending on the way muon bunches are produced.

The aim of this technique is the implantation in the sample investigated of a great number of polarized muons and the study of the time evolution of their magnetic moments ($\mu_\mu = 4.84 \cdot 10^{-3} \mu_B$).

$\vec{P}_\mu(t)$ is governed by the interactions of the muons with the local fields due to electronic and nuclear magnetic moments. After the average lifetime $\tau_\mu = 2.21 \mu s$, the muons decay emitting *positrons* with inhomogeneous asymmetric probability peaked along the beam direction (the muon spin is opposite to the velocity): monitoring the time evolution of the number of the positron emitted in a portion of solid angle around the sample, where a number of detectors are placed, $\vec{P}_\mu(t)$ can be revealed.

2.2.2 Production and Decay of Muons

The production of polarized muons derives from a mechanism characterized by many decays. First, a beam of protons is accelerated through a linear accelerator and reaches energies of the order of 500-800 MeV; the subsequent collision on a target made up of Beryllium or Carbon leads to the production of *positive pions* as the result of the reactions:



whose threshold energy is around 180 MeV. After a very short lifetime $\tau_\pi = 26 ns$, pions decay through the process

2. Fundamental Aspects of NMR and μ SR Techniques

$$\pi^+ \rightarrow \mu^+ + \nu_\mu. \quad (2.41)$$

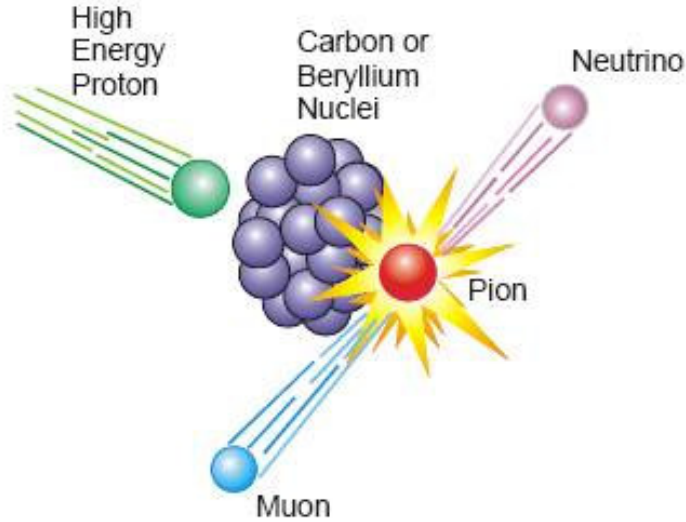


FIG.2.2 Sketch of the collision of the high energy proton beam with a Carbon or Beryllium target.

Positive muons can derive from both motionless pions and pions in motion. The first condition is preferable, because in that case the so-called “*stopping rate*” of the muons inside the sample is optimized.

The muons produced by pions in motion are not polarized but they can be polarized with a percentage varying from 60% to 80%, using focusing magnets.

The muons created from the decay of motionless pions, instead, are 100% polarized (the velocity direction is opposite to the spin one) and possess an energy of about 4.1MeV; their moment is about 29MeV/c.

2. Fundamental Aspects of NMR and μ SR Techniques

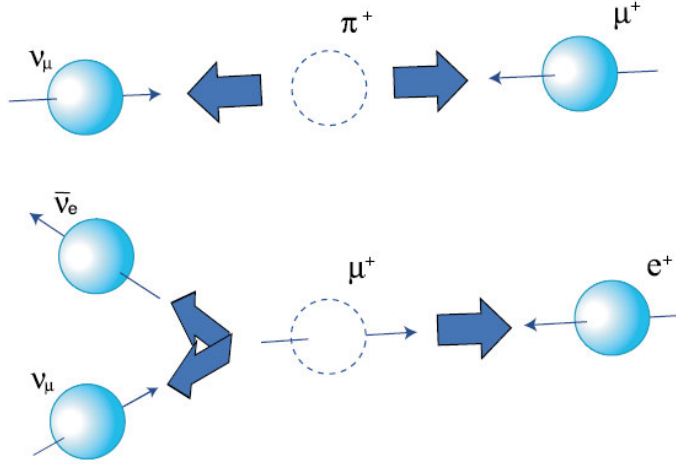


FIG.2.3 Pictorial description of π^+ and μ^+ decay process.

The experimental results in this work have been collected in two different laboratories: at ISIS Facility of Rutherford Appleton Laboratory, Oxford (England), and at Paul Scherrer Institute (PSI) Laboratory, Villigen (Switzerland).

At ISIS the *pulsed source* produces muons bunches containing 10^4 - 10^5 unities for a total 80ns duration and a 50Hz frequency rate. The periodic trigger of the pulses is used as clock and consequently the time limit of an acquisition is related to the length of the muon pulses. The relaxation of $\vec{P}_\mu(t)$ is recorded in the time interval between two adjacent muon bunches.

At PSI, instead, muons are produced by a *continuous source* and so they can be considered as continuously implanting in the sample: this technique is suitable to obtain a very good short times resolution, limited just by the electronics of the detector which can be as fast as 1ns: as a consequence also very fast relaxation rates can be detected. The limiting condition in the continuous technique is related to the distinction between two different positron decays.

2. Fundamental Aspects of NMR and μ SR Techniques

Once the muon enters the experimental region, it is detected and a clock starts; only after the revelation of the positron by one of the scintillators the clock is stopped. The problem is that if a muon arrives in the experimental area before the previous one has decayed, it's impossible to understand if the positron revealed by the detector comes from the first or the second muon present in the area. Such an event, therefore, must be disregarded. This situation sets the time limit to about $7\mu\text{s}$ for the observation of a relaxation process.

Once the muons μ^+ , possessing a positive charge, enter the sample, they tend to stop in electric potential wells i.e. negatively charged regions. Some of them also diffuse into the sample after the implantation but they remain far from regions where muon beam collision takes place and some lattice defects are created. After stopping, muons thermalize in few picoseconds, due to their interaction with electrons. The high speed of this process does not affect the muon polarization.

The final reaction which leads to positron relaxation detection consists in the decay of the muons through weak interaction, in three particles: a *positron*, an *electronic neutrino* and a *muonic anti-neutrino*:

$$\mu^+ \rightarrow e^+ + \nu_e + \bar{\nu}_\mu \quad (2.42)$$

In this kind of process the parity is violated and the cross section is not homogeneous as a function of the angle of emission. If $\varepsilon = E / E_{\text{max}}$ with $E_{\text{max}} \cong m_\mu c^2 = 105.66 \text{ MeV}$ and E the energy of the positron, the probability of emission of e^+ is expressed by the equation [38]:

$$dW^+ = W^+(\theta, \varepsilon) d\varepsilon d(\cos\theta) = \left(G^2 m_\mu^2 (3 - 2\varepsilon) \left[1 - \frac{1 - 2\varepsilon}{3 - 2\varepsilon} \cos\theta \right] \frac{\varepsilon^2}{192\pi^2} \right) d\varepsilon d(\cos\theta) \quad (2.43)$$

2. Fundamental Aspects of NMR and μ SR Techniques

where θ is the angle between the muon spin direction and the direction of emission of the positron detected and G is an interaction constant whose dimension is $[\text{m}^{-2}]$.

The probability distribution as a function of θ can be written as [39]:

$$W(\theta, \varepsilon) \propto 1 + A(\varepsilon) \cos \theta \quad (2.44)$$

where the so-called *asymmetry factor* $A(\varepsilon)$ is

$$A(\varepsilon) = \frac{(2\varepsilon - 1)}{(3 - 2\varepsilon)} \quad (2.45)$$

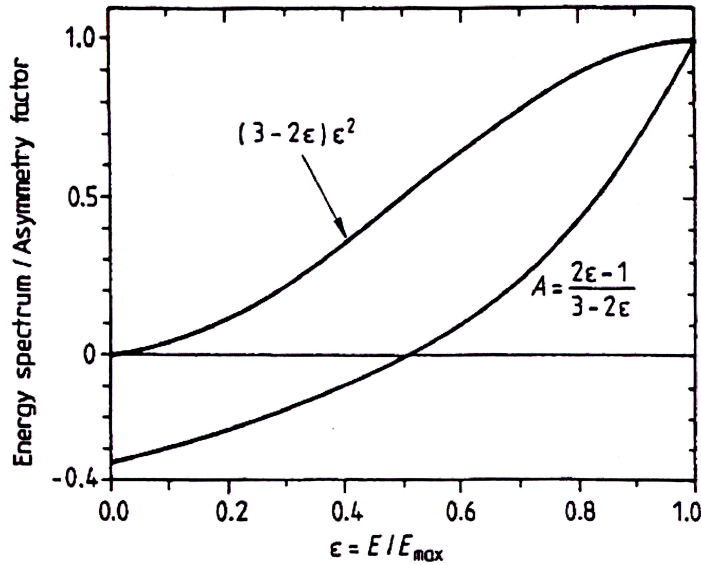


FIG.2.4 Energetic spectrum and asymmetry factor as a function of the emitted positron energy after muon decay.

2. Fundamental Aspects of NMR and μ SR Techniques

The total probability of decay can be obtained integrating (2.43) with respect to θ and ε :

$$W = \frac{1}{\tau_\mu} = \frac{G^2 m_\mu^5}{192\pi^3} \quad (2.46)$$

Instead, positron energy spectrum is obtained integrating (2.43) only with respect to $\cos(\theta)$, giving [40]

$$dW(\varepsilon) = W(\varepsilon) d\varepsilon = \frac{2(3-2\varepsilon)\varepsilon^2}{\tau_\mu} d\varepsilon \quad (2.47)$$

Since $A^+(1)=1$, the most part of the positrons is emitted parallel to μ^+ spin. By integrating over all the energies one obtains an average value for $A(\varepsilon)$ equal to $1/3$.

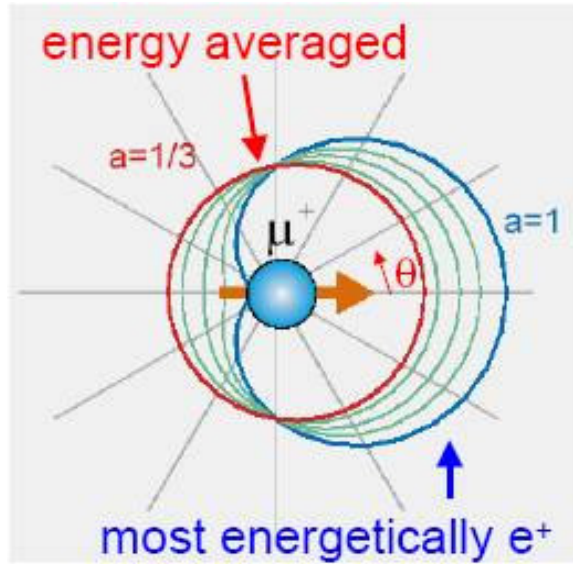


FIG.2.5 Angular distribution of the emission of positrons from muon decay with maximum energy (blue line) and after the integration over all the energies (red line).

2. Fundamental Aspects of NMR and μ SR Techniques

2.2.3 Experiments in Longitudinal and Transverse Fields

Measurements performed in this thesis make use of the so-called *longitudinal configuration*.

Let's consider at $t=0$ a large number N_0 of polarized muons stopped in the sample after the collision of the beam with the sample itself. Being $\vec{P}_\mu(0) = \langle \vec{\sigma}_\mu \rangle_{t=0}$ the initial polarized vector of the incident beam, where $\vec{\sigma}_\mu$ is defined as $2\vec{S}_\mu/\hbar$, the quantity of interest is the number dN of positrons emitted at an angle θ within the solid angle $d\sigma = \sin\theta d\phi$, in the time interval dt and in the energy range between ε and $\varepsilon+d\varepsilon$ [39]. From equation (2.43) we can write

$$dN = W(\theta, \varepsilon) N(t) dt d\varepsilon d\sigma \quad (2.48)$$

where $N(t)$ indicates the number of muons not yet decayed after a time t . Considering an exponential decay rate for muons, proper of a radioactive law,

$$N(t) = N_0 \exp(-t/\tau_\mu) \quad (2.49)$$

and making use of eq.s (2.43), (2.48), (2.49), the number of positrons detected by the scintillator is

$$N(t) = K \exp(-t/\tau_\mu) (1 + AP_\mu(0)\cos\theta) \quad (2.50)$$

where $0.2 < A < 0.3$ is the value of the asymmetry parameter averaged on the emitted energy with respect to the spectral sensitivity of the detectors.

The experiments of the present thesis have been performed in

2. Fundamental Aspects of NMR and μ SR Techniques

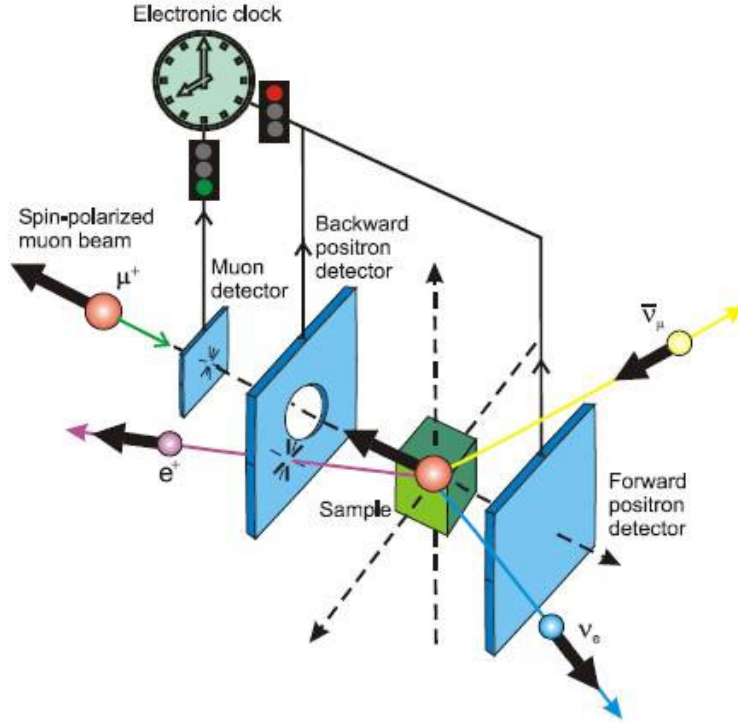


FIG.2.6 Experimental set up for μ SR measurements in longitudinal configuration.

zero field or in a static magnetic field \vec{H}_0 applied along the same direction of the beam polarization. In this situation one obtains:

$$N(t) = K \exp(-t/\tau_\mu) (1 + AP_z(0)G_{||}(t)\cos\theta) \quad (2.51)$$

The crucial quantity to be studied is $G_{||}(t)$, called *longitudinal polarization function* which corresponds to nuclear relaxation function in NMR. It allows to determine the time evolution, the distribution and the amplitude of the local magnetic fields at the muons sites [41].

The calibration experiments were performed with the static

2. Fundamental Aspects of NMR and μ SR Techniques

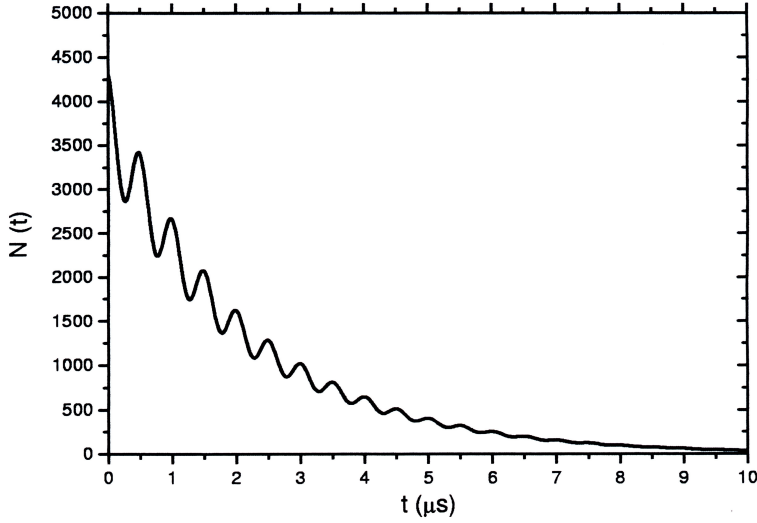


FIG.2.7 Signal detected by a scintillator as a function of time described in equation (2.50).

magnetic field applied in the direction perpendicular to the one of the muon beam polarization. As a result the spins precess around the field direction (analogously to what happens for NMR technique). In this case the expression of the number of positrons detected is

$$N(t) = K \exp(-t / \tau_{\mu}) (1 + AP_x(0) G_{\perp}(t) \cos(\omega_{\mu} t + \phi)) \quad (2.52)$$

In this configuration also the phase ϕ of the muons polarization, when the muons themselves enter in the magnetic field area, must be taken into account. In eq.(2.52), $\omega_{\mu} = 2\pi\gamma_{\mu}B$ is the precession frequency. In this case all the information about the system is included in the *transverse depolarization function* $G_{\perp}(t)$.

2. Fundamental Aspects of NMR and μ SR Techniques

2.2.4 Depolarization Functions

The detection system in a μ SR experiment consists in a series of *Backward-Forward scintillators* which cover all the solid angle around the sample area. The Backward scintillators are placed behind the sample, while the forward scintillators stand in the front space. This configuration allows us to find out the *longitudinal depolarization function* and the *transverse depolarization function*, which can be obtained in the so called transverse configuration, rotating by 90° the system of detectors. The result is

$$\frac{N(t,0)}{N(t,180)} = \alpha \frac{1 + AP_z(0)G_{||}(t)}{1 - AP_z(0)G_{||}(t)}. \quad (2.53)$$

In eq.(2.53) $N(t,0)$ is the number of positrons detected by forward detectors, $N(t,180)$ is the same quantity revealed by backward detectors and α is a parameter which takes into account the different sensitivity of the scintillators. As a consequence of this equation, the expression of the muon asymmetry can be written

$$A(t) \equiv AP_z(0)G_{||}(t) = \frac{N(t,0) - \alpha N(t,180)}{N(t,0) + \alpha N(t,180)}. \quad (2.54)$$

In the case of total muons polarization (100%), the signal is the asymmetry factor A , since longitudinal depolarization function is equal to one. In the following a more detailed study of $G_{||}(t)$ will be done.

The behaviour of the longitudinal depolarization function can be analyzed in two main cases related to the relationship between

2. Fundamental Aspects of NMR and μ SR Techniques

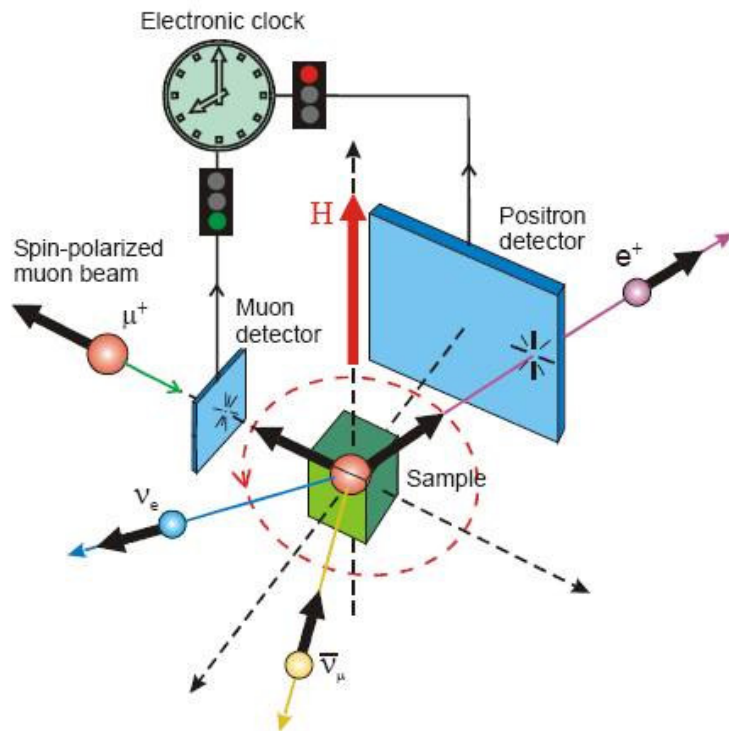


FIG.2.8 Experimental set up for μ SR measurements in transverse configuration.

the intensity of the external applied field and of the internal local fields. The limit cases are:

1. the external field is weaker than the local (i.e. at the muon site) fields
2. the external field is stronger than the local fields distribution

The first case includes two options: the external field is zero (the

2. Fundamental Aspects of NMR and μ SR Techniques

so-called *Zero-Field experiment*), the longitudinal external field is much weaker than the local fields distribution inside the sample.

If just local fields can be taken into account, calling \vec{B}_μ the internal field, the longitudinal depolarization function can be written [42]:

$$G(t)_\parallel = \cos^2 \theta + \sin^2 \theta \cos \omega_\mu t \quad (2.55)$$

where \vec{B}_μ is supposed to have a random orientation and forms an angle θ with the direction of the initial orientation of the muons polarization and the local fields distribution is described by e.g. a Gaussian centred in zero.

Averaging over the angle θ

$$G(t)_\parallel = \frac{1}{3} + \frac{2}{3} \langle \cos \omega_\mu t \rangle \quad (2.56)$$

and considering the *Gaussian distribution of local fields*, the function can be expressed as

$$G_\parallel(t) = \frac{1}{3} + \frac{2}{3} \left(1 - \gamma_\mu^2 \langle \Delta B^2 \rangle t^2 \right) \exp \left(-\frac{1}{2} \gamma_\mu^2 \langle \Delta B^2 \rangle t^2 \right). \quad (2.57)$$

Equation (2.57) is the *Kubo-Toyabe function* [43]: it quickly decays to zero with a Gaussian behaviour but after long time it recovers the constant value 1/3, approached asymptotically.

This behaviour is obtained, since 1/3 of the internal fields are supposed to be collinear with initial muons polarization, so that they don't cause neither muon spin precession nor depolarization.

2. Fundamental Aspects of NMR and μ SR Techniques

The above discussion has been done without taking into account the *fluctuations of local fields*, which modify the depolarization function. In presence of fluctuations of \vec{B}_μ the new depolarization function is referred as *dynamic Kubo-Toyabe* and it has an analytical expression in two regimes: (i) the *slow motion regime*, i.e. $\tau_c \gamma_\mu \sqrt{\langle \Delta B^2 \rangle} \gg 1$, where τ_c is the time related to fluctuations. In this case the relaxation behaviour remains Gaussian for short times while it becomes exponential for long times and its expression is [44]

$$G_{\parallel} \propto \frac{1}{3} \exp\left(-\frac{2}{3} \frac{t}{\tau_c}\right) \quad (2.58)$$

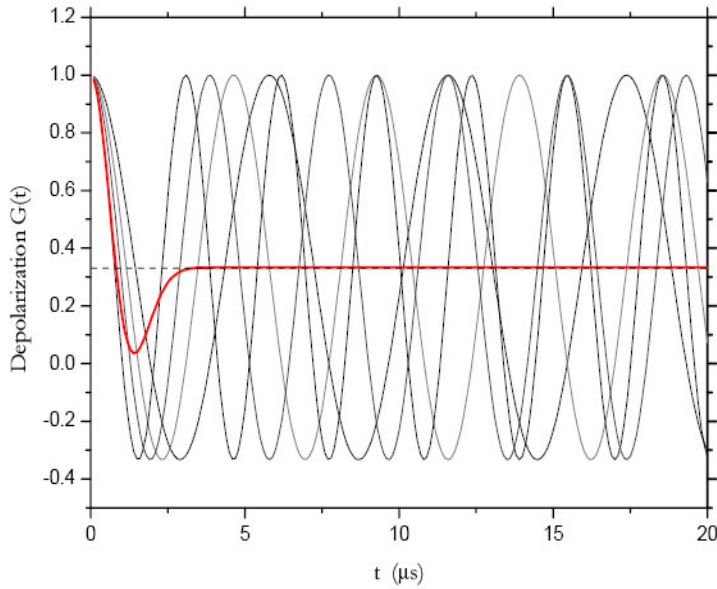


FIG.2.9 Behaviour of the Kubo-Toyabe function in zero field with the superposition of four different function of the form of eq.(2.57) calculated for various depolarization fields.

2. Fundamental Aspects of NMR and μ SR Techniques

(ii) the *fast motion regime* ($\tau_c \gamma_\mu \sqrt{\langle \Delta B^2 \rangle} \ll 1$): the most important feature is that the constant value for long times disappears, while the exponential behaviour ($\exp(-\lambda t)$), characteristic of Lorentzian form, is still valid.

Analogies between muon spin relaxation and nuclear spin relaxation spectroscopy are relevant if the longitudinal applied field is much stronger than the internal fields.

As for NMR, the Zeeman effect can be expressed by:

$$H_Z = -\vec{\mu}_\mu \cdot \vec{H}_0 = -\gamma_\mu \hbar \vec{S}_\mu \cdot \vec{H}_0 \quad (2.59)$$

and the effect of \vec{H}_0 on muon levels can be treated as in NMR theory.

Once the 100% polarized muons implant in the sample, depending on the direction of the static magnetic field applied, just one of the muons levels is totally occupied. This is not an equilibrium condition: in fact the muons ensemble has a different temperature with respect to the lattice one and one or more relaxation mechanisms act on this configuration to equalize the temperature of the system. Analogously to NMR spin-lattice relaxation time, the inverse of the relaxation time for \vec{P}_μ can be defined as [45]

$$\lambda = \frac{\gamma_\mu^2}{2} \int_{-\infty}^{\infty} \langle B_+(0) B_-(t) \rangle e^{-i\omega_\mu t} dt \quad (2.60)$$

which is mainly due to the hyperfine interactions between the muons and the surrounding (the lattice).

In this case the longitudinal depolarization function can be

2. Fundamental Aspects of NMR and μ SR Techniques

deduced from Kubo-Toyabe function, mixing Zero Field result with the exponential decay due to the spin-lattice relaxation just described, leading to

$$G_{\parallel}(t) = P_{\mu} \left(t, \langle \Delta B^2 \rangle, H_0, T \right) e^{-\lambda t}. \quad (2.61)$$

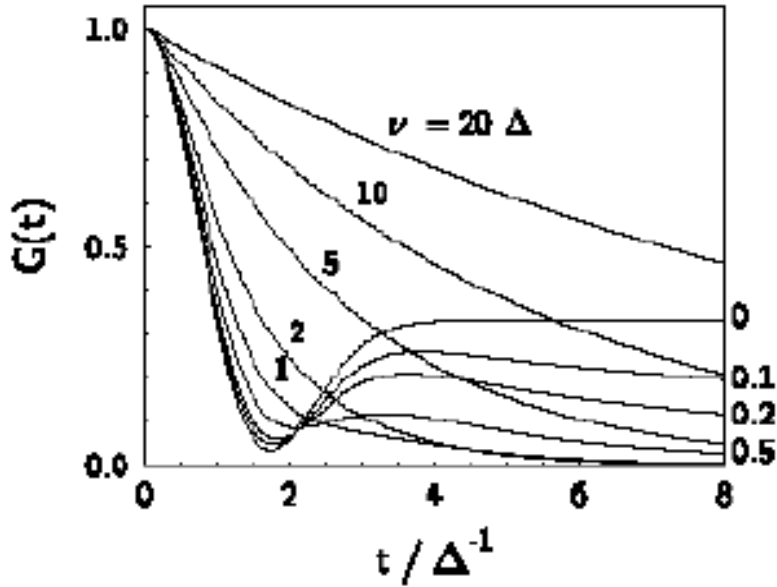


FIG.2.10 Dynamic Kubo-Toyabe behaviour in presence of local field fluctuations. Here it is reported for various ν/Δ values (ν =frequency of fluctuations, Δ =width of the distribution of local fields).

The muon spin feels a total magnetic field which is the sum of the external field and of the internal field and precesses around it. If the field is applied in the same direction of the initial muon polarization, the spins don't precess but remain aligned along their initial direction.

For long times, the constant value of Kubo-Toyabe rises

2. Fundamental Aspects of NMR and μ SR Techniques

progressively from $1/3$ to 1 with increasing static magnetic field intensity.

For transverse fields just a brief description will be given.

The most important distinction to understand the behaviour of transverse depolarization function is related to the characteristics of the local field fluctuations felt at muon sites. The behaviour of $G_{\perp}(t)$ can be divided in three main cases whose discriminant is

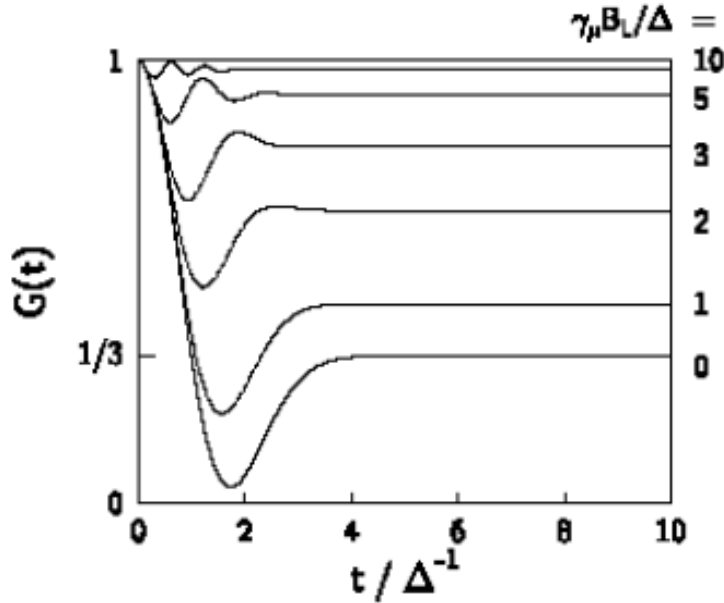


FIG.2.11 Kubo-Toyabe function behaviour in presence of growing longitudinal magnetic fields.

the relative intensity of the characteristic fluctuation time (τ_c) and the distribution of the Larmor frequencies of the muons around the field given by the sum of the external field and the local fields inside the sample.

In the *slow motion regime* ($\tau_c \gg (\Delta\omega_{\mu})^{-1} \equiv (2\pi\langle\Delta B^2\rangle^{1/2}\gamma_{\mu})^{-1}$), the

2. Fundamental Aspects of NMR and μ SR Techniques

depolarization function has a Gaussian form:

$$G_{\perp}(t) = \exp\left(\frac{-\langle \Delta B^2 \rangle \gamma_{\mu}^2 t^2}{2}\right) \equiv \exp(-\sigma_G^2 t^2) \quad (2.62)$$

where $\langle \Delta B^2 \rangle$ is the second moment of the frequency distribution. In an intermediate condition, an approximate expression is

$$G_{\perp}(t) = \exp\left(-\langle \Delta B^2 \rangle \gamma_{\mu}^2 \tau_c^2 \left[\exp\frac{-t}{\tau_c} - 1 + \frac{t}{\tau_c}\right]\right) \quad (2.63)$$

In the *fast motion limit* ($\tau_c \ll (\Delta\omega_{\mu})^{-1} \equiv (2\pi \langle \Delta B^2 \rangle^{1/2} \gamma_{\mu})^{-1}$) it becomes

$$G_{\perp}(t) = \exp(-\langle \Delta B^2 \rangle \gamma_{\mu}^2 \tau_c t) \equiv \exp(-\sigma_L t) \quad (2.64)$$

The *motional narrowing* phenomenon is present also in μ SR: it consists in the reduction of the resonance line width, because static distribution of fields is averaged (fast motion regime of the local fields). When fluctuations become faster, the shape of the line also changes from Gaussian to Lorentzian.

2.2.5 μ SR Study of Magnetic Powder Systems

μ SR spectroscopy is applied to many kinds of physical systems, but it is mainly used for the study of magnetic systems.

In this compounds, the muons implanted in the sample feel different internal interactions, such as transferred hyperfine and

2. Fundamental Aspects of NMR and μ SR Techniques

dipolar ones; the corresponding Hamiltonian can be written as [46]:

$$H = \hbar \vec{S}_\mu \cdot \sum_{\langle i \rangle} (A_i + D(\vec{r}_i)) \cdot \vec{S} \quad (2.65)$$

where A_i and $D(\vec{r}_i)$ are the *transferred hyperfine* and the *dipolar tensors* of the i -th spin respectively.

In most part of real systems many approximations can be assumed starting from this Hamiltonian of interaction: for example the transferred hyperfine tensor often becomes a simple constant scalar term and in the Hamiltonian just nearest-neighbours are taken into account. In some systems transferred hyperfine term is neglected because of the weakness of the wave function at muon sites; instead in metallic systems it becomes important, because the wave function is strong where a negative density charge is present, i.e. where muons tend to stop.

As already remarked, the magnetic moments of muons, once stopped in the sample, precess around the local internal field \vec{B}_μ with Larmor frequency $\omega_\mu = \gamma_\mu B_\mu$. When measurements are performed on powder samples, the angle between the muons initial polarization and \vec{B}_μ varies from grain to grain, so that 2/3 of the signal of the total symmetry precess, while 1/3 does not. In this case the expression for the muon polarization in terms of depolarization functions can be written

$$P_\mu = A \left[\frac{2}{3} G_\perp(t) \cos(\omega_\mu t) + \frac{1}{3} G_\parallel(t) \right]. \quad (2.66)$$

CHAPTER 3

One-Dimensional Magnetic Systems and Models

3.1 Introduction

In this chapter we will discuss from a theoretical point of view formalisms that will be used in Chapter 4 and in Chapter 5. We will introduce the fundamental concepts for the comprehension of the magnetic systems and in particular the 1D systems treated in this thesis. In the first part of the chapter the 1D magnetic systems will be considered, explaining their properties and the main approximations used for real 1D compounds. In the second section the theoretical methods applied to the study of the systems considered in this work will be described: in particular the Glauber Model used for the interpretation of the behaviour of CoPhOMe in Chapter 4 and the Transfer Matrix Method and its application to Ising Model and to Planar Model in Zero Field employed in the following chapters. In the last section, instead, we will focus on the frustrated spin systems and, in particular, on the quasi 1D frustrated spin systems examined in Chapter 5.

3.2 1D Magnetic Systems

3.2.1 The Spin Hamiltonian Formalism

In this work we will deal with magnetic systems that will be treated in the so-called Spin Hamiltonian formalism.

The properties of a magnetic system are, in general, related to the electronic and nuclear structure of the system itself. In the

3. One-Dimensional Magnetic Systems and Models

formalism that we will adopt here we will take into account just the electronic configuration of the orbitals, since the nuclear contribution is negligible: in fact the ratio between these two contributions is of the order of the fine-structure constant.

The electronic orbitals can be divided into two main types: the *fully occupied orbitals* and the orbitals with unpaired electrons. In the first case the contribution to the magnetic properties is diamagnetic: in fact in this kind of orbitals a variation of the applied external magnetic field changes the motion of the electrons in the orbitals with the generation of currents which causes an internal magnetic field opposed to the external one. As can be seen from susceptibility measurements, this temperature independent contribution is order of magnitude smaller than the one related to the contribution due to the orbitals constituted by unpaired electrons, which are called *magnetic orbitals*.

In principle one should take into account all the electronic coordinates and all the interactions present in the system to have a complete description of the magnetic properties of the system. In practice the solution of the complete Hamiltonian is not possible analytically. The Spin Hamiltonian, instead, is a model Hamiltonian which incorporates all the main interactions and coordinates in terms of a low number of parameters such as spin \vec{S} , Landé \vec{g} factors, \vec{J} constant which couples one spin to another, anisotropy terms \vec{A} and external magnetic fields applied to the sample.

In particular \vec{A} , \vec{S} and \vec{g} are, in general, 3x3 matrices, i.e. tensors, because they could be, in general, anisotropic quantities. These matrices can be reduced to a diagonal form by choosing a proper orthonormal base, and the axes corresponding to this base are called the principal axes of the system. In the orthonormal base, thus, just three components of the tensors which will be

3. One-Dimensional Magnetic Systems and Models

referred, for Landé factors for instance, as $g_{xx}=g_x$, $g_{yy}=g_y$, $g_{zz}=g_z$, survive. In most of the cases for all of these quantities the principal axes are coincident, because they are all related to the symmetry of the system .

As regards the \vec{J} constant, its matrix form is related to the coupling between the three components of each of the two spins involved in the exchange: often the off-diagonal (Dzyaloshinsky-Moriya terms) components are negligible and the diagonal ones are the only ones to be taken into account. In the following we will use this formalism for theoretical and real spin chains models.

The general expression for spin system consisting in N spins will be given in eq.(3.1).

3.2.2 Spin Chains: general properties

In this work two different types of the so-called *magnetic spin chains* will be analyzed and discussed.

A linear spin chain is a magnetic system where a large number of N magnetic moments are arranged in a one-dimensional lattice. Each magnetic moment is described by its corresponding spin \vec{S}_j where the subscript indicates the lattice site. Depending on the approach, spins can be considered either as vectors if they are described by a classical model or as quantum operators if they are treated in a quantum mechanical framework. The general form of the Hamiltonian with the most important interactions which spins can undergo, can be written in this case as:

$$H = -\sum_{\alpha} J_{\alpha} \sum_j \vec{S}_j \cdot \vec{S}_{j+\alpha} + H_{Anis} - g\mu_B \vec{H} \cdot \sum_j \vec{S}_j . \quad (3.1)$$

The first term of the Hamiltonian represents the effective

3. One-Dimensional Magnetic Systems and Models

Magnetic Exchange Interaction which describes the combined effect of electrostatic repulsion and Pauli exclusion principle. The exchange can be *Direct* if it is related to the Coulomb interaction of neighbouring unpaired electrons with an overlapping wave function. The exchange interaction can also be indirect i.e. *super-exchange*, when the magnetic unpaired electrons don't interact directly but via the electrons of non-magnetic ions involved in a covalent or metallic bond. J_α is the phenomenological exchange constant which can assume different values depending on the system studied: if $J_\alpha > 0$, the minimum of the spin system energy is reached when all the spins arrange themselves parallel (*ferromagnetic coupling*); if $J_\alpha < 0$ the configuration which minimizes the system energy is the one where each spin is anti-parallel with respect to its neighbours and the system is *antiferromagnetic*.

The sum over α takes into account the exchange interactions between spins belonging to different sites inside the chain, setting the range of the interactions themselves. In most of the real cases just nearest-neighbour (*n.n.*) interactions are taken into account and so the sum over α is omitted. Whenever next-nearest neighbour (*n.n.n.*) interactions are important, then $\alpha = 1, 2$.

The second term of the total Hamiltonian is the *Anisotropy Term* which is often responsible for the spins arrangement which determines the system symmetry. The presence of this contribution can be verified experimentally through magnetization measurements: in fact, in presence of anisotropy, the magnetization and the susceptibility depend on the direction of the applied magnetic field with respect to the crystal axes. Anisotropy effects are observable at a temperature comparable to the anisotropy interaction. Anisotropy can have different origin: one of the most important is the so called *single ion anisotropy* due to the indirect interaction between the crystal field and the

3. One-Dimensional Magnetic Systems and Models

electrons spins. Another source of anisotropy is due to the exchange interaction itself which can be different for the different spin components.

The last term of the Hamiltonian is the so-called *Zeeman Hamiltonian* which accounts for the application of an external field on the system studied and in particular on each magnetic moment related to each spin. It can be expressed as

$$\vec{\mu}_j = g\mu_B\vec{S}_j \quad (3.2)$$

where \vec{S}_j is the spin at the j -th site, $\mu_B = \frac{\hbar e}{2m_e c}$ and the Landè factor g can be calculated, for the real systems, from experimental measurements.

The simplest models for molecular chains take into account just the exchange interaction between nearest-neighbour so that the total Hamiltonian becomes simply:

$$H = -2J \sum_j \vec{S}_j \cdot \vec{S}_{j+1} \quad (3.3)$$

In this case three different models for chains can be described depending on the dimensionality of spin \vec{S}_j called d :

$$H = -2J \sum_j [S_j^x S_{j+1}^x + S_j^y S_{j+1}^y + S_j^z S_{j+1}^z] \quad (3.4a)$$

$$H = -2J \sum_j [S_j^x S_{j+1}^x + S_j^y S_{j+1}^y] \quad (3.4b)$$

$$H = -2J \sum_j [S_j^z S_{j+1}^z] \quad (3.4c)$$

3. One-Dimensional Magnetic Systems and Models

The model related to eq.(3.4a) is called *Isotropic Heisenberg Model* with $d=3$ and does not vary with rotation of the system in 3D space.

Eq.(3.4b) represents the so-called *Isotropic Planar Model* where $S_j^z=0$, $d=2$ and it does not vary with rotation on a plane; finally in eq.(3.4c) Ising Model is described with $S_j^z=\pm 1$, $d=1$ and it is invariant for $S_j^z \rightarrow -S_j^z$. These models are independent from system dimensionality, in fact they are suitable also for 3D and 2D systems.

3.2.3 Spin Chains: real systems

At the beginning of the 70s the first one-dimensional systems have been synthesized stimulating the experimental activity and improving the theoretical investigation.

The ideal model systems described in the previous section for magnetic chains have to be modified in the case of real systems. In fact, even if recently chemistry has improved its knowledge and chemists are able to synthesize 1D chains samples with a good control on the exchange couplings, especially as regards the interchain distance, the chains cannot be considered completely insulated from the interaction of the neighbour chains: thus a small but non negligible *interchain interaction* has to be taken into account.

The main parameter for the evaluation of the dimensionality of the system is $|J|/|J'|$ which represents the ratio between intrachain and interchain coupling constants. When the condition $|J'| < k_B T < |J|$, is verified, the system can be thought approximately as 1D. The condition to be verified for considering the sample as a 1D chain is, at least, $|J|/|J'| < 10^{-4}$. Thus the temperature range, in which the system can be considered as 1D, depends on $|J|/|J'|$ ratio. This ratio is related to another ratio, T_N/θ between two

3. One-Dimensional Magnetic Systems and Models

characteristics temperatures: T_N is the transition temperature towards three-dimensional phase, while θ represents the paramagnetic temperature which appears in Curie-Weiss Law of the susceptibility ($\chi \propto 1/(T-\theta)$). In any real system a temperature of transition towards 3D order exists, because J' has, in any case, a finite value. The weaker is the interchain coupling, the larger is the temperature range where the system can be considered one-dimensional.

From susceptibility measurements, the J coupling constant can be evaluated and an approximate value for θ can be found. Many

ANISOTROPY	SPIN	INTERACTION	SPIN DIMENSIONALITY	MODEL
$A \rightarrow \infty$	$S_x^2 + S_y^2 - S(S+1)$	$J_x = J_y \neq 0$	$d=2$	Planar
		$J_x = 0; J_y \neq 0$	$d=1$	Planar Ising
$A=0$	$S_x^2 + S_y^2 + S_z^2 - S(S+1)$	$J_x = J_y = J_z$	$d=3$	Heisenberg
		$J_x = J_y \neq 0; J_z = 0$	$d=2$	XY
		$J_x = J_y = 0; J_z \neq 0$	$d=1$	Z
$A \rightarrow -\infty$	$S_z^2 - S(S+1)$	$J_z \neq 0$	$d=1$	Ising

Table 3.1 Summary of the characteristics of the models for spin systems.

3. One-Dimensional Magnetic Systems and Models

measurements can be performed for evaluating T_N , for instance specific heat measurements, susceptibility, NMR, EPR, etc.

From a theoretical point of view, the most important models for one-dimensional compounds have been discussed in the previous paragraph; now the related general cases will be presented.

In fact for a complete description of the real systems also the anisotropy term must be taken into account and the Hamiltonian becomes [47]:

$$H = -2J \sum_j \vec{S}_j \cdot \vec{S}_{j+1} + A \sum_i (\vec{S}_i^z)^2. \quad (3.5)$$

Also in this case three different models can be summed up depending on anisotropy constant:

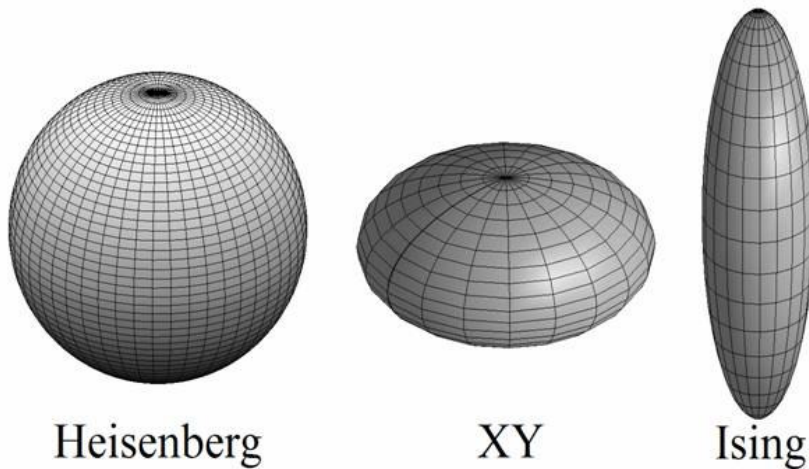


FIG.3.1 Schematic representation of the situations close to the three main limiting cases for the single ion anisotropy. The ellipsoids represent the fact that in real systems no g and A element is exactly zero, and perfect anisotropy is never reached.

3. One-Dimensional Magnetic Systems and Models

- a) $A=0 \rightarrow$ Isotropic Heisenberg Model as in eq.(3.4a)
- b) $A>0 \rightarrow$ Heisenberg Model with easy-plane anisotropy; if $A \rightarrow +\infty$ the case of eq.(3.4b) can be obtained
- c) $A<0 \rightarrow$ Heisenberg Model with easy-axis anisotropy; if $A \rightarrow -\infty$ the case of eq.(3.4c) can be obtained

This sketch is just a schematic point of view of real systems; in fact many factors can modify the condition and characteristics of each system:

- 1) the exchange coupling could be not isotropic, i.e. each component of the exchange coupling constant could be different from the other ones ($J_x \neq J_y \neq J_z$): this situation lead to the so-called XYZ Model which is the generalization of the Isotropic Heisenberg Model.
- 2) anisotropy term can assume different forms in comparison to the one codified in the previous models
- 3) the application of a magnetic field to the sample can change the spin configuration and its dynamics, depending on the field intensity; in a compound where the anisotropy term is relevant, also the direction of the field can increase the effects of the anisotropy itself or works against it if it is applied along a direction different from the one of the easy anisotropy axis.

3. One-Dimensional Magnetic Systems and Models

3.2.4 Spin Dynamics in 1D Magnetic Systems

The most important aspect studied in this thesis is the spin dynamics of one-dimensional and quasi one-dimensional spins systems. For this purpose we have to introduce here some definitions related to the physical quantities which will be theoretically derived and experimentally measured. One of the main parameter which is measured in NMR is the nuclear spin-lattice relaxation rate T_1^{-1} . This parameter is related directly to the Fourier Transform of the *spin-spin correlation function*, which is defined in general as [14][31][48-49]

$$G_{ij}^{\alpha\gamma}(t) = \langle S_i^\alpha(0) S_j^\gamma(t) \rangle \quad (3.6)$$

where $\alpha, \gamma=x, y, z$ and $i, j=1, \dots, N$ represent the number of the spin system considered, while $\langle \rangle$ is the average value over the electronic spins ensemble. The correlation function represents the probability of having a particular value of the component γ of the spin at j -th site at a particular time t , once it is known the value at $t=0$ of the component α of the spin at i -th site.

In particular for a system whose Hamiltonian is invariant for a rotation around an axis, such in the case when the Hamiltonian consists in a quadratic expression of the spin operators, the correlation function has the expression

$$G_{ij}^\alpha(t) = \langle S_i^\alpha(0) S_j^\alpha(t) \rangle \quad (3.7)$$

where $\alpha=z, +, -$ being $S_i^\pm = S_i^x \pm iS_i^y$.

If the Hamiltonian of the system is invariant for rotations with respect to the x and y axes, the equation

3. One-Dimensional Magnetic Systems and Models

$$\langle S_i^+(t) S_j^-(0) \rangle = \langle S_i^-(t) S_j^+(0) \rangle \quad (3.8)$$

is valid.

For $t=0$ the correlation function reduces to the *static correlation function*

$$\langle S_i^\alpha(0) S_j^\alpha(0) \rangle \quad (3.9)$$

which gives information about the degree of static order of the spins system.

In the particular case of spin chains for finite temperature ($T \neq 0$), the behaviour of the static correlation function is

$$\lim_{m \rightarrow \infty} \langle S_i^\alpha(0) S_{i+m}^\alpha(0) \rangle \approx \exp\left(-\frac{ma}{\xi_s}\right) \quad (3.10)$$

where ξ_s is the so-called *correlation length* and a is the *lattice step*. ξ_s is a fundamental parameter for the comprehension of the order of the system: in fact in a system with correlated spins there are two different types of order called *short range order* (SRO) and *long range order* (LRO) respectively. In the first case ξ_s has a finite value which represents the finite distance over which the spins are correlated: for a paramagnetic system at high temperature the correlation length is zero. If the correlation length diverges then one has LRO with spontaneous magnetization. For the ideal 1D systems, the long range order occurs only at $T=0$: this is a very general result which follows from simple considerations about stability of 1D systems with respect to the finite temperature fluctuations and can be derived by considering the competition between entropy and internal energy terms in the free energy expression of the spin system;

3. One-Dimensional Magnetic Systems and Models

differently, in real 1D systems the spins develop a SRO on lowering the temperature until eventually they order in a 3D LRO phase.

Often the *correlation function* is used in the *normalized form*:

$$g_{ij}^{\alpha\beta}(t) = \frac{\langle S_i^\alpha(0) S_j^\beta(0) \rangle}{\langle S_i^\alpha(0) S_i^\alpha(0) \rangle} \quad (3.11)$$

where it is normalized to its value in the case when $t=0$, $i=j$ and $\alpha=\gamma$.

The Fourier Transform of the correlation function which is related to the NMR relaxation rate T^{-1}_1 is [14][31][48-49]

$$J_{ij}^{\alpha\beta}(\omega) = \int g_{ij}^{\alpha\beta}(t) e^{-i\omega t} dt \quad (3.12)$$

and is called *spectral density*, which accounts for the spectrum of spin fluctuations.

Another quantity is useful from an experimental point of view and can be defined

$$f_i^{\alpha\beta}(\vec{q}, \omega) = \int dt e^{i\omega t} \sum_i g_{ij}^{\alpha\beta} e^{-i\vec{q} \cdot \vec{r}_{ij}}. \quad (3.13)$$

It is called *dynamic structure factor*.

3. One-Dimensional Magnetic Systems and Models

3.3 1D Magnetic Models

3.3.1 Glauber Kinetic Ising Model

The theoretical calculation of the spin-spin correlation function (CF) can be done, in principle, from the knowledge of the spin Hamiltonian; in practice the calculation can be done analytically only for simple cases such as, for example, 1D chains. The static CF was calculated exactly by Fisher [50] for the classical *Heisenberg model*. The dynamic CF in 1D Heisenberg models can be obtained in the long time approximation leading to the well-known result of the diffusive $t^{-1/2}$ dependence of the CF [12,16]. The Ising Model [51] does not have any dynamics, since there is no transverse term in the Hamiltonian. Glauber [1] back in 1963 proposed a dynamic model where the dynamics is introduced *ad hoc* by considering the probability of a spin to exchange energy with a thermal bath.

The innovation introduced by Glauber was related to the fact that he treated the stochastic spin dynamics from a statistical point of view, taking into account many external factors which could change the spins behaviour. This theory predicts a slow dynamics of the magnetization at low temperature with a thermally activated regime driven by an Arrhenius law. This theory has been improved for various specific cases in the following years, for instance by taking into account one-dimensional systems affected by finite-size effects [52]. The interesting result following the Glauber theory and regarding the slowing down of the magnetization was utilized in the interpretation of the phase transitions [48]. However the direct verification of *Glauber theory* [1] in 1D spin system was not possible until the beginning of the 90s when samples synthesized in Firenze [23], allowed the fulfilment of the special

3. One-Dimensional Magnetic Systems and Models

conditions necessary to verify Glauber model [1] in single chain magnets (SCM).

This theory will be explained in the following taking into account different cases examining different conditions underwent by the spin system.

Starting from the Ising Model [51], Glauber assigned for each spin a stochastic function $s_j(t)$ that can assume just two values $s_j(t)=\pm 1$.

First let us consider a non-interacting spin system where each individual spin can just interact thermally with the surrounding environment. In this situation, the transition probability is the same for each spin which can change its own state randomly. Calling $w(s_j)=\alpha/2$ the transition probability from one state to another and $p(s,t)$ the probability to find the j -th spin with the spin value s at time t , the time evolution of the transition probability can be written

$$\frac{d}{dt} p(s,t) = -\frac{\alpha}{2} p(s,t) + \frac{\alpha}{2} p(-s,t) \quad (3.14)$$

where for $p(s,t)$ stands the normalization condition

$$p(s,t) + p(-s,t) = 1. \quad (3.15)$$

Naming as $q(t)$ the expectation value of spin s at time t

$$q(t) \equiv \langle s(t) \rangle = s p(s,t) - s p(-s,t), \quad (3.16)$$

using equation (3.14) and deriving equation (3.16), the time evolution for spin expectation value can be rewritten

$$\frac{d}{dt} q(t) = -\alpha q(t) \quad (3.17)$$

3. One-Dimensional Magnetic Systems and Models

and the solution is

$$q(t) = q(0) e^{-\alpha t} \quad (3.18)$$

where $q(0)$ is the initial expectation value and α is the probability per unit time for a spin transition.

Let us consider now spins interacting through the Ising Hamiltonian in the form of an exchange coupling

$$H = -J \sum_j s_j s_{j+1} . \quad (3.19)$$

In this case the transition probability must be written down taking into account the behaviour of the nearest-neighbours of the spin considered.

The expression for the transition probability can be written

$$w(s_j) = \frac{\alpha}{2} \left[1 - \frac{\gamma}{2} s_j (s_{j-1} + s_{j+1}) \right] \quad (3.20)$$

In general there are three different values that can be assumed by the transition probability:

$$w(s_j) = \frac{1}{2} a_0 (1 - \gamma) \quad (3.21a)$$

$$w(s_j) = \frac{1}{2} a_0 \quad (3.21b)$$

$$w(s_j) = \frac{1}{2} a_0 (1 + \gamma) \quad (3.21c)$$

3. One-Dimensional Magnetic Systems and Models

whose corresponding spins configurations are

$$\begin{array}{ccc} j-1 & j & j+1 \\ \uparrow & \uparrow & \uparrow \end{array} \quad (3.22a)$$

$$\begin{array}{ccccccc} j-1 & j & j+1 & & j-1 & j & j+1 \\ \uparrow & \uparrow & \downarrow & \text{or} & \downarrow & \uparrow & \uparrow \end{array} \quad (3.22b)$$

$$\begin{array}{ccc} j-1 & j & j+1 \\ \downarrow & \uparrow & \downarrow \end{array} \quad (3.22c)$$

Consequently:

for $J > 0 \rightarrow \gamma > 0$ (FERROMAGNETIC CASE)

(3.22a) Highest Energy State (less probable)

(3.22c) Lowest Energy State (more probable)

for $J < 0 \rightarrow \gamma < 0$ (ANTI-FERROMAGNETIC CASE)

(3.22a) Lowest Energy State (more probable)

(3.22c) Highest Energy State (less probable)

with the second configuration corresponding, for both the cases,

3. One-Dimensional Magnetic Systems and Models

to the insulated spin case.

Before going on with the explanation of Glauber model, let's establish the relationship between the exchange coupling constant J and the γ parameter.

For the interacting spin system one can define, analogously to the previous case, the probability $p(\{s\},t)$ for the system to assume a particular spin configuration $\{s\}=(s_1, s_2, \dots, s_j, \dots, s_N)$ at time t , where N is the number of the spins in the system considered.

The time evolution equation for the probability cited above is

$$\frac{d}{dt}p(\{s\},t) = - \left[\sum_j w(s_j) p(s_1, \dots, s_j, \dots, s_N, t) \right] + \left[\sum_j w(s_j) p(s_1, \dots, -s_j, \dots, s_N, t) \right]. \quad (3.23)$$

When the system reaches the equilibrium configuration, the Maxwell-Boltzmann statistics is valid and the probability for a spin to assume the value s_i or $-s_i$ is proportional to the Boltzmann

factor $e^{-\frac{H}{k_B T}}$ and results

$$\frac{p(s_j)}{p(-s_j)} = \frac{\exp\left[\frac{J}{k_B T} s_j (s_{j-1} - s_{j+1})\right]}{\exp\left[-\frac{J}{k_B T} s_j (s_{j-1} - s_{j+1})\right]}. \quad (3.24)$$

Considering eq.(3.23) at the equilibrium ($\frac{d}{dt}p(\{s\},t)=0$) one can write:

$$\frac{p(s_j)}{p(-s_j)} = \frac{w(-s_j)}{w(s_j)} = \frac{1 + \frac{1}{2} \gamma s_j (s_{j-1} + s_{j+1})}{1 - \frac{1}{2} \gamma s_j (s_{j-1} + s_{j+1})} \quad (3.25)$$

3. One-Dimensional Magnetic Systems and Models

Comparing now eq.(3.24) and eq.(3.25), one has

$$\gamma = \tanh\left(\frac{2J}{k_B T}\right) \quad (3.26)$$

In his theory Glauber [1] defines the same quantity as in the isolated spin case such as the expectation value for each spin named $q_k(t)$: for a finite ring the total magnetization of the system becomes

$$M(t) = \sum_j q_k(t) \propto \exp\left(-\frac{t}{\tau}\right) \quad (3.27)$$

where

$$\tau = \frac{1}{\alpha(1-\gamma)}. \quad (3.28)$$

In low temperature limit equation (3.28) becomes

$$\tau = \tau_0 \exp\left(\frac{4J}{k_B T}\right) \quad (k_B T \ll |J|) \quad (3.29)$$

with $\tau_0 = \frac{1}{2\alpha}$.

Analyzing eq.(3.29) one can see that, for a ferromagnetic coupling, the relaxation time diverges, while for an anti-ferromagnetic coupling there is no divergence.

In presence of an external magnetic field the Hamiltonian can be written

$$H = -g\mu_B H \sum_j s_j - J \sum_j s_j s_{j+1} \quad . \quad (3.30)$$

3. One-Dimensional Magnetic Systems and Models

Under these conditions the transition probability changes again its expression, since one must take into account the fact that spins tend to align along the field direction.

Glauber assumed

$$w(s_j) = \frac{\alpha}{2} \left[1 - \frac{\gamma}{2} s_j (s_{j-1} + s_{j+1}) \right] (1 - \beta s_j) \quad (3.31)$$

where

$$\beta = \tanh \left(\frac{g\mu_B H}{k_B T} \right) \quad (3.32)$$

Proceeding as in the previous cases, the average value for magnetization is

$$M(t) = \frac{(g\mu_B)^2 N}{k_B T} \frac{1 - \eta^2}{1 + \eta^2} \int_{-\infty}^t \exp[-\alpha(1 - \gamma)(t - t')] H(t') \alpha dt' \quad (3.33)$$

where

$$\eta = \tanh \left(\frac{J}{k_B T} \right). \quad (3.34)$$

Up to now we have treated the general case of the Glauber model [1] for a ferromagnetic or an anti-ferromagnetic coupling. Now let's briefly describe the application of the model to our specific case. We will have to deal with a *ferrimagnet* constituted by two sublattices where the Landé factors have different values (see Chapter 4). It can be demonstrated that [23][53], following the same procedure of Glauber, and considering the two different

3. One-Dimensional Magnetic Systems and Models

sublattices we still have an exponential thermally activated relaxation time. In this case, however, there is a further condition to be fulfilled: in fact the relaxation rate expression depends on the initial condition as follows:

- 1) $\tau = \frac{1}{\alpha(1-\gamma)}$ system starts evolving in the configuration
with parallel spins
- 2) $\tau = \frac{1}{\alpha(1+\gamma)}$ system starts evolving in the configuration
with anti-parallel spins

This means that the relaxation time can diverge in the case of a ferrimagnet [23][53][54], differently from the case of an anti-ferromagnet. In particular in our system we have a particular arrangement of the spins, since CoPhOMe is constituted by a helical system with each primitive cell constituted by three Cobalt ions and three radical centres, i.e. six different sites. For finding the solutions of the problem in our case we can just focus on one cell imposing boundary periodic conditions with the result of having six different equations of the form [23][53]:

$$\dot{\vec{\sigma}} = A\vec{\sigma} + \vec{k} \quad (3.35)$$

where $\sigma_1, \sigma_2, \sigma_3, \sigma_4, \sigma_5, \sigma_6$ are the spins of the micro-system investigated, whose directions are the ones of the local anisotropy axes and $\vec{k}=(k_1, k_2, k_3, k_4, k_5, k_6)$ are the inhomogeneous terms. We can obtain six non-coupled equations thanks to the diagonalization of matrix A and introducing collective coordinates $\xi=(\sigma_1, \sigma_2, \sigma_3, \sigma_4, \sigma_5, \sigma_6)$. The solutions of the equations obtained are [53]:

3. One-Dimensional Magnetic Systems and Models

$$\xi_i(t) = k_i \int_{-\infty}^t e^{-\alpha_i(t-t')} \alpha dt' \quad (3.36)$$

while the six eigenvalues of matrix A are

$$\alpha_1 = (1 + \gamma)\alpha \quad (3.37a)$$

$$\alpha_2 = (1 - \gamma)\alpha \quad (3.37b)$$

$$\alpha_3 = \left(1 - \frac{\gamma}{2}\right)\alpha \quad (3.37c)$$

$$\alpha_4 = \left(1 + \frac{\gamma}{2}\right)\alpha \quad (3.37d)$$

$$\alpha_5 = \left(1 + \frac{\gamma}{2}\right)\alpha \quad (3.37e)$$

$$\alpha_6 = \left(1 + \frac{\gamma}{2}\right)\alpha \quad (3.37f)$$

with $\alpha_3, \alpha_4, \alpha_5, \alpha_6$ which are always different from zero being $|\gamma| < 1$, while, analyzing the first two eigenvalues, results

$$\tau_1 = \frac{1}{2\alpha} \exp\left(-\frac{4J}{k_B T}\right) \quad (3.38a)$$

$$\tau_2 = \frac{1}{2\alpha} \exp\left(\frac{4J}{k_B T}\right) \quad (3.38b)$$

3. One-Dimensional Magnetic Systems and Models

being $\tau_i = \frac{1}{\alpha_i}$ if $\frac{|J|}{k_B T} \rightarrow \infty$ (very low temperatures). From the form of the two relaxation rates we can say that both for $J < 0$ and for $J > 0$ we have always a slow relaxation for modes ξ_1 and ξ_2 respectively.

If a magnetic field is applied along the plane perpendicular to the axis of the helix results for ξ_1 and ξ_2

$$k_{\perp 1} = k_{\perp 2} = 0 \quad (3.39)$$

with \vec{k}_{\perp} the component of \vec{k} along the field direction, while in the case when the field is applied along the chain axis we have

$$k_{\parallel 1} = \frac{3}{\sqrt{6}} \frac{s\mu_B H_0}{k_B T} \frac{1-\eta^2}{1+\eta^2} \cos \theta (g_{Co} - g_R) \quad (3.40a)$$

$$k_{\parallel 2} = \frac{3}{\sqrt{6}} \frac{s\mu_B H_0}{k_B T} \frac{1-\eta^2}{1+\eta^2} \cos \theta (g_{Co} + g_R) \quad (3.40b)$$

with \vec{k}_{\parallel} the component of \vec{k} along the new direction of the magnetic field.

In the first case no slow relaxation can be activated by the application of a magnetic field perpendicular to the chain axis, while applying the magnetic field along the chain axis we obtain a slow relaxation related to the ξ_2 mode, being the coupling constant $J < 0$ in the case of CoPhOMe [53].

3. One-Dimensional Magnetic Systems and Models

3.3.2 Transfer Matrix Method

In this paragraph we will briefly describe one of the most used theoretical method [56] for the calculation of analytical and numerical solutions from the model Hamiltonians mentioned in paragraphs 3.2.2-3.2.3 and used for the theoretical interpretation of the systems studied in this work.

For using such method various assumptions must be made both on the spin system and on the Hamiltonian describing the system itself.

The spin system must obey the following conditions:

- 1) 1D system consisting of N spins
- 2) spins \vec{S}_i are classical unit vectors
- 3) spins periodic boundary conditions are $\vec{S}_{i+N} = \vec{S}_i$

The Hamiltonian must be:

- 1) invariant for translations
- 2) containing sums of nearest neighbours interactions

$$(H = -\sum_{i=1}^N V(\vec{S}_i, \vec{S}_{i+1}))$$

- 3) symmetric with respect to the exchange of two spins

$$(H(\vec{S}_i, \vec{S}_{i+1}) = H(\vec{S}_{i+1}, \vec{S}_i))$$

3. One-Dimensional Magnetic Systems and Models

This method starts from the so-called *transfer integral equation*

$$\int d\vec{S}_{i+1} e^{-\beta V(\vec{S}_i, \vec{S}_{i+1})} \psi_n(\vec{S}_{i+1}) = \lambda_n \psi_n(\vec{S}_i) \quad (3.41)$$

where $\beta = 1/k_B T$.

The aim of this technique consists in the determination of the eigenfunctions $\psi_n(\vec{S}_i)$ and of the eigenvalues λ_n of eq.(3.41).

Transfer integral equation (3.41) can be simplified since:

$$\sum_n \psi_n^*(\vec{S}_i) \psi_n(\vec{S}_j) = \delta_{ij} \quad (3.42a)$$

$$\int d\vec{S}_i \psi_n(\vec{S}_i) \psi_{n'}(\vec{S}_i) = \delta_{nn'} \quad (3.42b)$$

being the eigenfunctions a complete (eq.(3.42a)) orthonormal (eq.(3.42b)) set: thus it results

$$e^{-\beta V(\vec{S}_i, \vec{S}_{i+1})} = \sum_n \lambda_n \psi_n^*(\vec{S}_i) \psi_n(\vec{S}_{i+1}). \quad (3.43)$$

Also, being the *classical partition function*

$$Z_N = \int d\vec{S}_1 \dots \int d\vec{S}_N \prod_i e^{-\beta V(\vec{S}_i, \vec{S}_{i+1})} \quad (3.44)$$

we obtain

$$Z_N = \sum_{n=0}^{\infty} \lambda_n^N \quad (3.45)$$

3. One-Dimensional Magnetic Systems and Models

with a spectrum consisting in an infinite number of real eigenvalues with an upper limit.

In the *thermodynamic limit*, i.e. for $N \rightarrow \infty$, the partition function is dominated by the maximum eigenvalue of the spectrum that will be referred as λ_0 . Thus one has

$$Z_N = \lambda_0^N. \quad (3.46)$$

With this approximation, thermodynamic quantities such as susceptibility and magnetization can be calculated with the equations

$$\chi = -N^2 k_B T \frac{\partial^2 \lambda}{\partial H^2} \quad (3.47a)$$

$$M = -N^2 k_B T \frac{\partial \lambda}{\partial H} \quad (3.47b)$$

where H is the magnetic field, and analogously the spin pair static correlation function can be obtained through

$$\langle S_i^\alpha S_{i+m}^\alpha \rangle \approx \sum_{n=0}^{\infty} \left(\frac{\lambda_n}{\lambda_0} \right)^m \left| \int d\vec{S} \psi_n^*(\vec{S}) S^\alpha \psi_0(\vec{S}) \right|^2 \quad (N \rightarrow \infty) \quad (3.48)$$

From the fluctuation-dissipation theorem, one can deduce the susceptibility without knowing the field dependence of λ_0 :

$$\chi = \frac{Ng^2 \mu_B^2}{k_B T} \sum_m \langle S_i^\alpha S_{i+m}^\alpha \rangle. \quad (3.49)$$

In the two following paragraphs we will discuss the two classical

3. One-Dimensional Magnetic Systems and Models

models, Ising Model and Planar Model, used in this thesis for the interpretation of the real systems studied in Chapter 4 and in Chapter 5 and the most important thermodynamic quantities will be derived with the Transfer Matrix Method.

3.3.2.1 Application to the Ising Model

The Hamiltonian describing a spin chain in the Ising Model [51] is

$$H = -2J \sum_i S_i^z S_{i+1}^z - g\mu_B H \sum_i S_i^z \quad (3.50)$$

where J is the exchange coupling constant, $S^z = \pm \frac{1}{2}$ with periodic boundary conditions $\vec{S}_{i+N} = \vec{S}_i$ and N the number of spins of the chain considered. In the case when the spin can assume just discrete values, the transfer integral operator is reduced to a simple matrix. In the present case the *integral transfer equation* is represented by the simple matrix equation

$$\begin{pmatrix} e^{\beta(A+B)} & e^{-\beta A} \\ e^{-\beta A} & e^{\beta(A+B)} \end{pmatrix} \begin{pmatrix} \psi_{n,j+1}^+ \\ \psi_{n,j+1}^- \end{pmatrix} = \lambda_n \begin{pmatrix} \psi_{n,i}^+ \\ \psi_{n,i}^- \end{pmatrix} \quad (3.51)$$

where $A = 2JS^2$, $B = g\mu_B SH$ and $\beta = 1/k_B T$.

The eigenvalues are

$$\lambda_{\pm} = e^A \cosh(B) \pm \sqrt{e^{2A} \sinh^2(B) + e^{-2A}} \quad (3.52)$$

In the thermodynamic limit results

3. One-Dimensional Magnetic Systems and Models

$$\lim_{N \rightarrow \infty} Z_N = \lambda_N^+ =$$

$$= \left\{ e^{\beta JS^2} \cosh(\beta g \mu_B SH) + \left[e^{2\beta JS^2} \sinh^2(\beta g \mu_B SH) + e^{-2\beta JS^2} \right]^{1/2} \right\}^N \quad (3.53)$$

and for $H=0$

$$Z_N = [2 \cosh(\beta J)]^N \quad (3.54)$$

which is the result obtained by Ising [51].

Starting from Transfer Matrix Method [55] we can get the *free energy*

$$F = -k_B T \ln \left[2 \cosh \left(\frac{2JS^2}{k_B T} \right) \right] \quad (3.55)$$

the spin-pair correlation function in Zero Field

$$\langle S_i^z S_{i+r}^z \rangle =$$

$$= \lim_{N \rightarrow \infty} \frac{1}{Z_N} \sum_{S^z} S_i^z S_{i+r}^z \exp \left[2A\beta \sum_{i=1}^N S_i^z S_{i+r}^z \right] = \quad (3.56)$$

$$= S^2 \left(\frac{\lambda_-}{\lambda_+} \right)^{|r|} = S^2 \tanh^{|r|} \left(\frac{J}{k_B T} \right)$$

and consequently the reciprocal of the correlation length is

3. One-Dimensional Magnetic Systems and Models

$$\frac{1}{\xi} = -\ln \left[\tanh \left(\frac{J}{k_B T} \right) \right] \quad (3.57)$$

which exponentially vanishes at low temperatures.

Finally with this method also susceptibility and specific heat for $H=0$ can be respectively derived through the equations

$$\frac{\chi_T}{N(g\mu_B S)^2} = \frac{1}{k_B T S^2} \sum_{p=-\infty}^{\infty} \langle S_{i+p}^z S_i^z \rangle = \frac{1}{k_B T} \frac{1 + \tanh \left(\frac{J}{k_B T} \right)}{1 - \tanh \left(\frac{J}{k_B T} \right)} = \frac{1}{k_B T} e^{\frac{2J}{k_B T}} \quad (3.58)$$

$$C = Nk_B \left(\frac{J}{k_B T} \frac{1}{\cosh \left(\frac{J}{k_B T} \right)} \right)^2 \quad (3.59)$$

In eq.(3.59) it is easy to notice that specific heat vanishes for $T \rightarrow 0^+$.

3.3.2.2 Application to the Planar Model in Zero Field

The Hamiltonian representing a planar system in Zero Field is [56]

$$H = -2J \sum_i \left(S_i^x S_{i+1}^x + S_i^y S_{i+1}^y \right) \quad (3.60)$$

where the spins, whose periodic conditions are still $\vec{S}_{i+N} = \vec{S}_i$, are forced to lie in a plane and thus just two of its components

3. One-Dimensional Magnetic Systems and Models

survive. Introducing polar coordinates, $\vec{S}_i = S(\cos\theta_i, \sin\theta_i)$ the partition function becomes

$$Z_N = \int_0^{2\pi} d\varphi_1 \dots \int_0^{2\pi} d\varphi_N \exp \left[2\beta JS^2 \sum_{i=1}^N \cos(\varphi_{i+1} - \varphi_i) \right] \quad (3.61)$$

Decoupling the integrals of the partition function with the substitution

$$\theta_i = (\varphi_{i+1} - \varphi_i) \quad (3.62)$$

the expression of the partition function itself becomes

$$Z_N = \left[\int_0^{2\pi} d\theta \exp \left(\frac{2JS^2}{k_B T} \cos \theta \right) \right]^N \quad (3.63)$$

and in the thermodynamic limit, it results to be

$$Z_N = \left[2\pi I_0 \left(\frac{2JS^2}{k_B T} \right) \right]^N \quad (3.64)$$

where I_0 is the Bessel function with imaginary argument. Also in this case we can derive the free energy

$$F = -k_B T \left\{ \ln(2\pi) + \ln \left[I_0 \left(\frac{2JS^2}{k_B T} \right) \right] \right\}, \quad (3.65)$$

the spin pair correlation function

3. One-Dimensional Magnetic Systems and Models

$$\langle \vec{S}_i \cdot \vec{S}_{i+r} \rangle = S^2 \langle \cos(\varphi_{i+1} - \varphi_i) \rangle = S^2 \left[\frac{I_1\left(\frac{1}{T^*}\right)}{I_0\left(\frac{1}{T^*}\right)} \right]^{|r|} = S^2 w(1/T^*)^{|r|} \quad (3.66)$$

where

$$T^* = \frac{k_B T}{2JS^2} \quad (3.67)$$

and the correlation length, whose expression for $T \rightarrow 0^+$ is

$$\xi \cong \frac{4|J|S^2}{k_B T} \quad (3.68)$$

Finally we obtain also susceptibility and specific heat as in the Ising Model case: their expression are respectively

$$\chi = \frac{N(g\mu_B)^2}{k_B T} \sum_r \langle S^x_n S^x_{n+r} \rangle = \frac{1}{2} \frac{N(g\mu_B S)^2}{k_B T} \frac{1 + w(1/T^*)}{1 - w(1/T^*)} \quad (3.69)$$

$$C = Nk_B \left(\frac{1}{T^*} \right) \left[1 - w^2\left(\frac{1}{T^*}\right) - T^* w\left(\frac{1}{T^*}\right) \right] \approx \begin{cases} \frac{1}{2} \left(\frac{1}{T^*} \right)^2 & \text{for } T \rightarrow +\infty \\ \frac{1}{2} \left(1 + \frac{T^*}{2} \right) & \text{for } T \rightarrow 0^+ \end{cases} \quad (3.70)$$

In the limit of very low temperatures, the susceptibility remains finite for $J < 0$ while for $J > 0$ it diverges as T^2 .

3. One-Dimensional Magnetic Systems and Models

The expression for specific heat has been obtained using the Bessel functions property $\frac{d}{dx} I_1(x) = I_0(x) - \frac{I_1(x)}{x}$.

3.4 Frustrated Spin Systems

In this section we will talk about the so-called frustrated spin systems in one dimension. In the systems studied in Chapter 5 the frustration arises from the competition between different interactions of comparable strength which tend to orient the spins in different directions. Frustration can also arise from simple geometrical arguments. The typical example is the equilateral triangular lattice with spins on the edge of each triangle coupled by a *n.n.* antiferromagnetic exchange interaction. In this case the system is frustrated and the ground state degenerate. Nearest-neighbour interactions may be sufficient to remove the degeneracy and generate a stable non degenerate ground state. In the case of 1D systems, that we will discuss about in this paragraph, the interactions taken into account will be extended even beyond the nearest-neighbours ones. The most important interactions in 1D magnetic chains are intrachain exchange couplings and these are the only ones considered in the model discussed below. The dipolar interactions and the interchain couplings are much weaker and will be taken into account to extend the validity of the model to very low temperatures. The model described in the following is the simplest one; it is discussed just to give the reader a general knowledge of its power also in the interpretation of quite complicated systems.

The basic assumptions on the 1D system studied are:

- 1) spin chain of N classical spins

3. One-Dimensional Magnetic Systems and Models

- 2) ferromagnetic nearest-neighbours interactions ($J_1 > 0$)
- 3) antiferromagnetic next nearest-neighbours interaction ($J_2 < 0$)
- 4) the ratio between the two exchange interactions is defined as $\delta = \frac{|J_2|}{J_1}$
- 5) the lattice step is assumed to be $a=1$
- 6) planar nature of the system

The Hamiltonian in this case is given by

$$H = -2J_1 \sum_i \vec{S}_i \cdot \vec{S}_{i+1} - 2J_2 \sum_i \vec{S}_i \cdot \vec{S}_{i+2} \quad (3.71)$$

where the spins $\vec{S}_i = (\cos\theta_i; \sin\theta_i)$ are unit vectors in the plane perpendicular to the chain axis with the usual boundary conditions $\vec{S}_{i+N} = \vec{S}_i$.

Eq.(3.71) thus becomes

$$H = -2J_1 \sum_i \cos(\theta_{i+1} - \theta_i) - 2J_2 \sum_i \cos(\theta_{i+2} - \theta_i) \quad (3.72)$$

The ground state can be determined minimizing the energy of the entire system: in our case the minima of the energy must be searched in the function

$$E_0 = -2AJ_1 N [\cos(q_0) - \delta \cos(2q_0)] \quad (3.73)$$

3. One-Dimensional Magnetic Systems and Models

where for brevity $q_0 = \theta_{i+1} - \theta_i$ assuming the angles for adjacent spins to be identical.

The *discriminant* for the determination of the minima and of the phases of the system investigated is δ and results

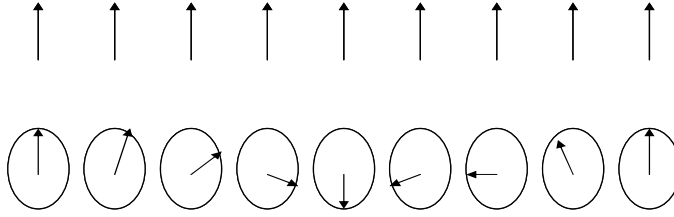


FIG.3.2 Pictorial sketch of the two spin configuration for a one-dimensional frustrated system as studied by Harada. For $\delta < 1/4$ the system assumes a ferromagnetic configuration (ABOVE), for $\delta > 1/4$ the order is helical (BELOW).

$$\left\{ \begin{array}{ll} \cos q_0 = \frac{1}{4\delta} & \text{for } \delta > \frac{1}{4} \quad \text{HELICAL ORDER} \\ \sin q_0 = 0 & \text{for } \delta < \frac{1}{4} \quad \text{FERROMAGNETIC ORDER} \end{array} \right. \quad (3.74)$$

The conditions in eqs.(3.74) mean that, depending on the relative strength of the two exchange interactions, *two different orders* dominate at low temperatures. The two configurations are depicted in FIG.3.2: in particular in the second case the helix is two-fold degenerate because of the invariance of the system with respect to the rotations; the helix pitch is $2\pi/q_0$ with two different possible values for q_0 :

3. One-Dimensional Magnetic Systems and Models

$$q_0 = \pm \arccos\left(\frac{1}{4\delta}\right) \quad (3.75)$$

signalling another two-fold degeneration in the ground state related, in this case, to the *clockwise* or *counterclockwise arrangement* of the spins in the plane perpendicular to the chain axis. In fact these two states at $T=0$ are characterized by an opposite *chirality* which can be classified through *chirality order parameter* defined for each pair of spins as [26][28]

$$\vec{K}_i = \frac{\vec{S}_i \times \vec{S}_{i+1}}{|\sin q_0|}. \quad (3.76)$$

This parameter is a three dimensional vector [27] in the Heisenberg Model while in the Planar Model it is a scalar quantity and at $T=0$ the values assumed are ± 1 [26] for clockwise and anticlockwise spins arrangement respectively.

The phase diagram of these kinds of systems has been studied by many scientists, depending on the degree of frustration of various compounds and suggesting various models for the interpretation of the experimental results. Two of the most important researchers who studied *helimagnets* behaviour have been Harada [25-27] and Villain [28,29] (see also Chapter 1).

The first one started from the system described by the Hamiltonian in eq.(3.71) [26] and suggested that the two-fold degeneration arising from the two *helical arrangements* of the spins in the ground state could cause excitations of the stable chiral *domain walls* separating two domain with different chirality [26]; these excitations can give a non-linear contribution to the thermodynamic properties.

He studied the system with the transfer matrix method [55].

3. One-Dimensional Magnetic Systems and Models

Specific heat calculations for different values of δ are shown in FIG. 3.3.

The results show a peak for $\delta > 1/4$ (that is to say in the helical phase) which smoothens when $\delta < 1/4$ (ferromagnetic phase). This

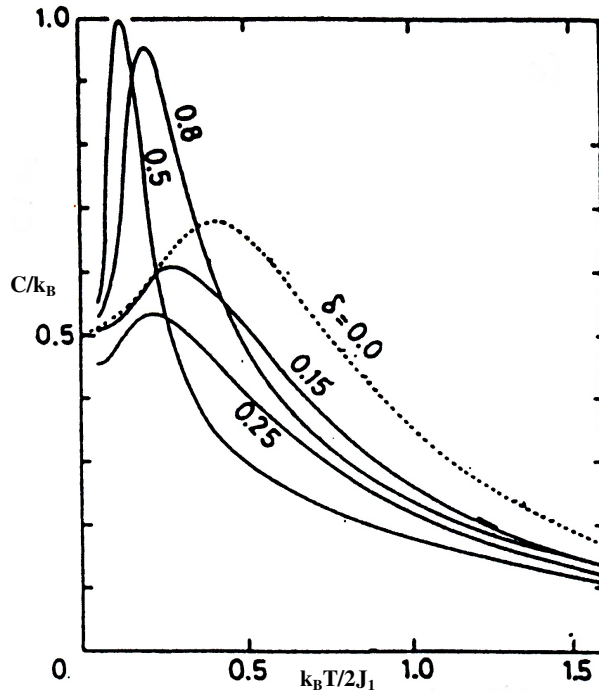


FIG.3.3 Specific heat as a function of $k_B T / 2J_1$ calculated with transfer matrix method with planar model for various values of the discriminant δ (see text).

anomaly has been related by Harada to the chiral excitations which are absent in the ferromagnetic phase.

He studied the same problem also with the Heisenberg Model [27] assuming

3. One-Dimensional Magnetic Systems and Models

1) $J_1, J_2 < 0$

2) $j = J_2/J_1$

Also in this case the specific heat shows a peak for $j > 1/4$ and no peaks for $j < 1/4$ (see FIG. 3.4)

This time the peak is broader than in the previous case, since, as already mentioned before, in the former case K_i is scalar and the

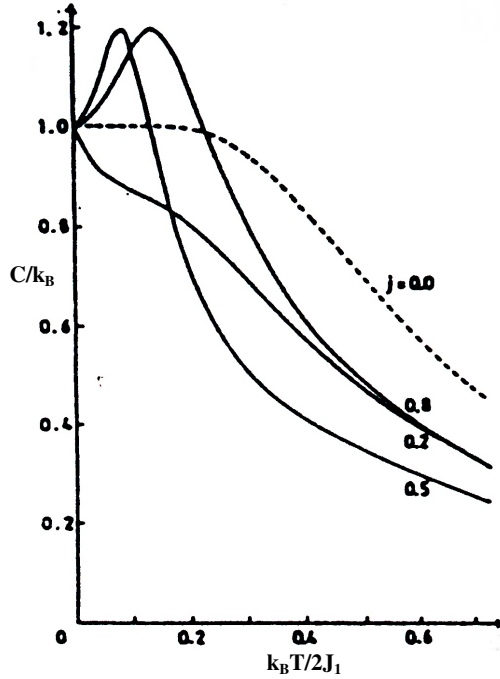


FIG.3.4 Specific heat as a function of $k_B T / (2J_1)$ calculated with transfer matrix method with Heisenberg model for various values of the discriminant j (see text).

excitations are Ising-like while in the latter case the chirality order parameter is a vector and the effects due to domain walls

3. One-Dimensional Magnetic Systems and Models

are less important [27]. This study has been the guideline for the earlier interpretations regarding the behaviour of the helical frustrated systems discussed in Chapter 5.

A revisiting of this kind of systems has been done by Villain [28][29]: he studied fully frustrated systems especially taking into account various intrachain exchange interactions for systems with identical spins. This study have been later developed [57] for a system composed by two different kinds of spins. It was considered [57] the more complex Hamiltonian

$$H = H_{\text{intra}} + H_{\text{inter}} \quad (3.77)$$

with [57-58]

$$H_{\text{intra}} = \sum_{i=1}^M \sum_{n=1}^{N/2} \left\{ -J_1 (\vec{S}_{i,2n-1} \cdot \vec{S}_{i,2n} + \vec{S}_{i,2n} \cdot \vec{S}_{i,2n+1}) - J_2 (\vec{S}_{i,2n-1} \cdot \vec{S}_{i,2n+1}) + \right. \\ \left. - J'_2 (\vec{S}_{i,2n} \cdot \vec{S}_{i,2n+2}) - g\mu_B \vec{H} \cdot \vec{S}_{i,2n-1} - g'\mu_B \vec{H} \cdot \vec{S}_{i,2n} + D(S_{i,2n-1}^z)^2 \right\} \quad (3.78)$$

and

$$H_{\text{inter}} = \sum_{\langle i,j \rangle} \sum_{n=1}^N \left[-J_{\perp} (\vec{X}_{i,n} \cdot \vec{X}_{j,n}) \right] \quad (3.79)$$

where $J_1 > 0$ is the nearest-neighbour exchange coupling constant, $J_2 < 0$ and $J'_2 < 0$ are next-nearest neighbour constants between spins of the type S and type s respectively; g and g' are Landé factors of the spins S and s respectively, $D > 0$ is the single-ion anisotropy constant term, J_{\perp} is the interchain magnetic coupling which becomes important at low temperature and $\vec{X}_{j,n} = \vec{S}_{j,n}, \vec{s}_{j,n}$.

3. One-Dimensional Magnetic Systems and Models

The periodic boundary conditions are $\vec{S}_{N+1} = \vec{S}_1$ and $\vec{S}_{N+2} = \vec{S}_2$.

The ground state of the system represented by the Hamiltonian in eq.(3.78) for $H=0$ can be expressed as [59]

$$E_0 = -\frac{N}{2} J_1 S s [2 \cos(Qa) - (\delta + \delta') \cos(2Qa)] \quad (3.80)$$

where Q is one of the absolute maxima of

$$I(q) = J_1 S s [2 \cos(qa) - (\delta + \delta') \cos(2qa)] \quad (3.81)$$

and

$$\delta = \frac{|J_2| S^2}{J_1 S s} \quad (3.82a)$$

$$\delta' = \frac{|J'_2| s^2}{J_1 S s} \quad (3.82b)$$

Under the condition $2(\delta + \delta') > 1$ the helical ground state is favoured for this samples and the pitch of the helix is

$$\pm Qa = \pm \cos^{-1} \left[\frac{1}{2(\delta + \delta')} \right] \quad (3.83)$$

where + and - are related to clockwise and counterclockwise rotation of the spins along the chain axis.

Following a procedure similar to the one adopted by Harada, Villain and then Rettori [29] [57] found out that for *quasi-1D XY helimagnets* the phase diagram is characterized by two phase transitions (see Chapter 5):

3. One-Dimensional Magnetic Systems and Models

1) $T > T_0 \Rightarrow$ PARAMAGNETIC PHASE

2) $T_N < T < T_0 \Rightarrow$ CHIRAL PHASE

3) $T < T_N \Rightarrow$ HELICAL PHASE

The novelty is the presence of an intermediate *chiral phase* where there is a spontaneous breaking of the translation invariance, even if the overall invariance with respect to rotations and time reversal is not broken.

Now we will evaluate the two transition temperatures T_0 and T_N . Using the *Green's-function approach* and the *spectral theorem* [60][61] the transverse two-spin correlation function can be obtained for the two different kinds of spins of the chain considered [57][62]:

$$\begin{aligned}
 & \langle S^x_1 S^x_{2n+1} S^y_1 S^y_{2n+1} \rangle \approx \\
 & \approx S^2 \cos(2Qna) e^{-\frac{2}{N} \sum_k [1 - \cos(2kna)]} \langle \psi_k \psi_{-k} \rangle \approx \quad (3.84a) \\
 & \approx S^2 \cos(2Qna) e^{-\frac{2|n|a}{\xi^s}}
 \end{aligned}$$

$$\begin{aligned}
 & \langle S^x_2 S^x_{2n+2} S^y_1 S^y_{2n+2} \rangle \approx \\
 & \approx s^2 \cos(2Qna) e^{-\frac{2}{N} \sum_k [1 - \cos(2kna)]} \langle \psi_k \psi_{-k} \rangle \approx \quad (3.84b) \\
 & \approx s^2 \cos(2Qna) e^{-\frac{2|n|a}{\xi^s}}
 \end{aligned}$$

These results are valid for low temperatures where the *continuum*

3. One-Dimensional Magnetic Systems and Models

approximation can be used. In the case studied the correlation length ξ_s is defined as:

$$\frac{\xi_s}{a} = \frac{J_1 s S}{k_B T} \frac{4(\delta + \delta')^2 - 1}{\delta + \delta'} \quad (3.85)$$

The relationship between the susceptibility of an isolated spin chain $\chi_{1D}(k_{\parallel})$ (see for its expression also [57]) and a three dimensional susceptibility $\chi_{3D}(k_{\parallel}, k_{\perp})$ is, in the mean-field approximation [63]

$$\chi_{3D}(k_{\parallel}, k_{\perp}) = \chi_{1D}(k_{\parallel}) \cdot \left[1 - \frac{J_{\perp} (S^2 + s^2) \cos(k_{\perp} a_{\perp})}{N/2 (g' \mu_B S + g \mu_B s)^2} \chi_{1D}(k_{\parallel}) \right]^{-1}. \quad (3.86)$$

Finally the condition for an estimation of T_N is [57]

$$\chi_{3D}(k_{\parallel} = \pm Q, k_{\perp} = 0) \rightarrow \infty \quad (3.87)$$

resulting in the equation

$$\frac{k_B T_N}{J_1} = \sqrt{\frac{J_{\perp}}{J_1}} \sqrt{S s \frac{S^2 + s^2}{2} \frac{4(\delta + \delta')^2 - 1}{\delta + \delta'}} \quad (3.88)$$

For an estimation of T_0 [57], instead, one must take into account the fact that two regions of opposite chirality are separated by domain walls that can be of various types, depending on the system studied: here we will consider localized domain walls. In this specific case the system consists in two different kinds of spins and, as a consequence, the domain walls can be of three

3. One-Dimensional Magnetic Systems and Models

different kinds:

- 1) domain walls localized on spin S
- 2) domain walls localized on spin s
- 3) domain walls localized between spin S and spin s

and the correspondent excitations energies are

$$1) \Delta E_a = 2J_1 S s \delta \left[1 - \frac{1}{2(\delta + \delta')} \right] \left[1 + \frac{1}{2(\delta + \delta')} \right] \quad (3.89a)$$

$$2) \Delta E_b = 2J_1 S s \delta' \left[1 - \frac{1}{2(\delta + \delta')} \right] \left[1 + \frac{1}{2(\delta + \delta')} \right] \quad (3.89b)$$

$$3) \Delta E_c = 2J_1 S s (\delta + \delta') \left[1 - \frac{1}{2(\delta + \delta')} \right] \quad (3.89c)$$

Using the mean-field approximation, the *interaction energy* between two finite regions of definite chirality, whose length is

$\frac{\xi_k}{a} \propto e^{\Delta E / k_B T}$, is given by

$$\begin{aligned} E_{\perp} &= -J_{\perp} \sum_{n=1}^{\xi_k/2} (\vec{S}_{i,n} \cdot \vec{s}_{j,n}) - J_{\perp} \frac{\xi_k}{a} \langle \vec{S}_{i,1} \cdot \vec{s}_{j,1} \rangle \cong \\ &\cong -\beta J_{\perp}^2 \frac{\xi_k}{a} \sum_{n=1}^{\xi_k/2} \{ \langle (\vec{S}_{i,1} \cdot \vec{s}_{j,1}) (\vec{S}_{i,n} \cdot \vec{s}_{j,n}) \rangle_{(0)} \} \end{aligned} \quad (3.90)$$

where the interchain coupling interaction has been treated in first order perturbation theory.

The *four-spin correlation function* can be written as

3. One-Dimensional Magnetic Systems and Models

$$\langle (\vec{S}_{i,1} \cdot \vec{S}_{j,1}) (\vec{S}_{i,n} \cdot \vec{S}_{j,n}) \rangle_{(0)} = \frac{1}{2} (1 + \mu_i \mu_j) \cdot \left\{ \frac{1}{2} \langle (\vec{S}_{i,1} \cdot \vec{S}_{i,n}) (\vec{S}_{j,1} \cdot \vec{S}_{j,n}) \rangle_{(0)} \right\} \quad (3.91)$$

where the equation has been expressed in terms of effective Ising spins $\mu_i = \pm 1$ and the energy E_{\perp} can be thus written

$$\begin{aligned} E_{\perp} &= -\frac{1}{2} (1 + \mu_i \mu_j) \cdot \left\{ \beta J_{\perp}^2 \frac{\xi_k}{a} \frac{1}{2} (Ss)^2 \sum_{n=0}^{\xi_k/a} \cos^2(2Qna) e^{-\frac{4|n|a}{\xi_s}} \right\} \equiv \\ &\equiv -\frac{1}{2} (1 + \mu_i \mu_j) \cdot \left\{ \beta J_{\perp}^2 \frac{\xi_k}{a} \frac{1}{2} (Ss)^2 \frac{1}{8} \frac{\xi_s}{a} \right\} \end{aligned} \quad (3.92)$$

where ξ_s is the correlation length of the two-spin correlation functions at low temperatures in the continuum limit, being $\xi_s \ll \xi_k$.

The condition for the occurrence of the chiral transition is that the Ising interaction [64-68] is of the order of $k_B T$; considering the expressions of the two correlation lengths mentioned before, one has

$$\frac{k_B T_0}{J_1} = \frac{\Delta E}{J_1} \left\{ \ln \left[\left(\frac{k_B T_0}{J_1} \right)^3 \cdot \frac{1}{(J_{\perp}/J_1)^2 (1/16)(Ss)^3 [4(\delta+\delta)^2 - 1]/(\delta+\delta)} \right] \right\}^{-1} \quad (3.93)$$

From eqs.(3.88) and (3.93) in the case $J_{\perp} \ll J_1$, i.e. when interactions among neighbour chains are negligible, T_N results to be much lower than T_0 (see also Chapter 5).

CHAPTER4

Pure and Zinc-Doped CoPhOMe

4.1 General Features

4.1.1 Introduction

As mentioned in Chapter 3, many magnetic properties of low dimensional systems theoretically predicted decades ago have not been experimentally observed, due to the inability in synthesizing materials which fulfilled the characteristics of a one-dimensional compound. One of the first systems that approximated well a magnetic chain was the so called TMMC [12-16] (its chemical formula is $[(\text{CH}_3)_4\text{N}]\text{MnCl}_3$), whose $J_{\text{inter}}/J_{\text{intra}}$ is about 10^{-4} . Nowadays many others compounds have been synthesized with a lower ratio between interchain and intrachain coupling. Among these systems one of the most relevant is constituted by $\text{Co}(\text{hfac})_2\text{NITPhOMe}$ ($\text{N}_4\text{C}_{24}\text{F}_{12}\text{O}_8\text{H}_{21}$) [23] (in the following called simply CoPhOMe) which will be analyzed in this chapter. In the first part of the chapter the most important features of CoPhOMe will be summed up, from previous Magnetization, Susceptibility, NMR and μSR measurements performed in collaboration with the University of Firenze. As regards to the second part of the chapter, CoPhOMe doped with Zn impurities will be investigated with the same techniques for a comparison with the pure system.

4. Pure and Zinc-Doped CoPhOMe

4.1.2 Structure

In the framework of one-dimensional systems, CoPhOMe, synthesized for the first time at the beginning of the 90s by Caneschi and his co-workers in Firenze, is characterized by a very low ratio between interchain and intrachain exchange interaction (less than 10^{-5}). CoPhOMe is a compound whose structure develops along one direction (z axis or c crystal direction) and it is characterized by the presence of divalent *Cobalt ions* (Co^{2+}) connected through organic radical centres. The properties of radicals are crucial for the magnetic behaviour of the compound, because the radical moiety used determines the interchain distance and thus the interchain interaction. These stable centres are constituted by *radicals* of the *nitronyl-nitroxide* family (NITR) where the organic element R in FIG.4.1 is a para-methoxy-phenyl which will be referred as PhOMe.

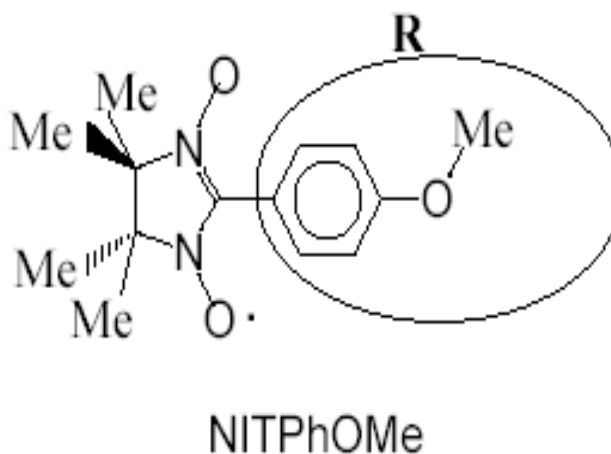


FIG.4.1 Sketch of NITPhOMe where R is the organic component of the radical centre.

4. Pure and Zinc-Doped CoPhOMe

Summing up, the chains are characterized by the alternation, along the chain direction, of ions belonging to the first series of *transition metals*, and of *radical centres*. The entire chain is nothing but a simple repetition of the fundamental unity metal-radical.

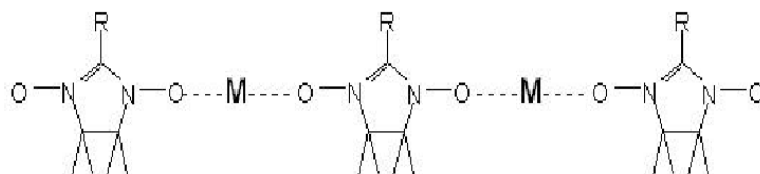


FIG.4.2 Sketch of the linear structure of Pure CoPhOMe.

The structure of this material is much more complicated than in normal one-dimensional molecular magnets: in fact Cobalt ions arrange themselves in *trigonal crystallographic lattice* and,

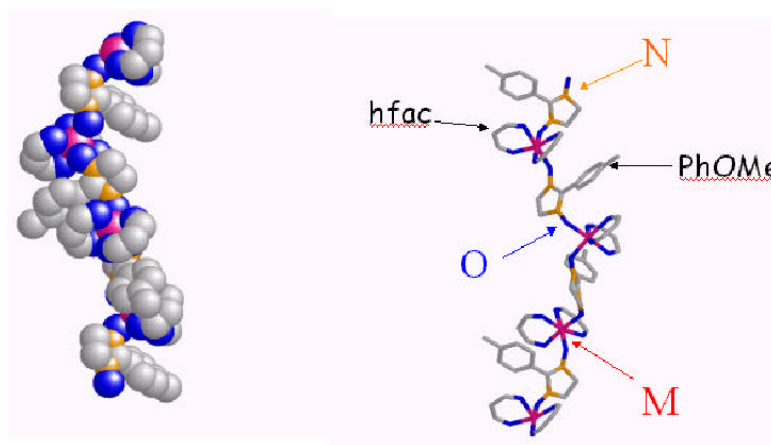


FIG.4.3 Pictorial representation of CoPhOMe single chain magnet crystallized in the trigonal system; on the right picture the position of the main components of the material are indicated.

4. Pure and Zinc-Doped CoPhOMe

because of *supramolecular interactions*, as in manganese analogues [69], the chain has an helical structure characterized by a ternary screw axis. The elementary cell, consisting in three metallic ions and three radical centres, is the results of a 120° rotation combined with the translation of $1/3$ of the length of the cell along the *trigonal axis* c .

As verified by X-ray diffraction measurements, the closest distance between two neighbour chains is 11.3\AA , while metal-



FIG.4.4 Representation of the exagonal packing of the helical chains and of the elementary cell.

metal distance along trigonal axis of the chain is 6.9\AA .

Despite this little difference between intrachain and interchain distances, it was found out that the coupling interaction along the chain is orders of magnitude stronger than interchain interaction,

4. Pure and Zinc-Doped CoPhOMe

so that the 1D nature of the compound is assured.

4.1.3 Interactions and Electronic Configuration

As shown in FIG.4.1, the strong intrachain interaction between Cobalt ions and radical centres is due to the peculiar properties of the radical inserted in the chain during synthesis: in fact it has an unpaired electron in the outer shell which is strongly delocalized with the same probability to be on the two N-O centres [70]: in this way there is a direct exchange between the paramagnetic metal ion and the radical, so that the latter is able to transmit

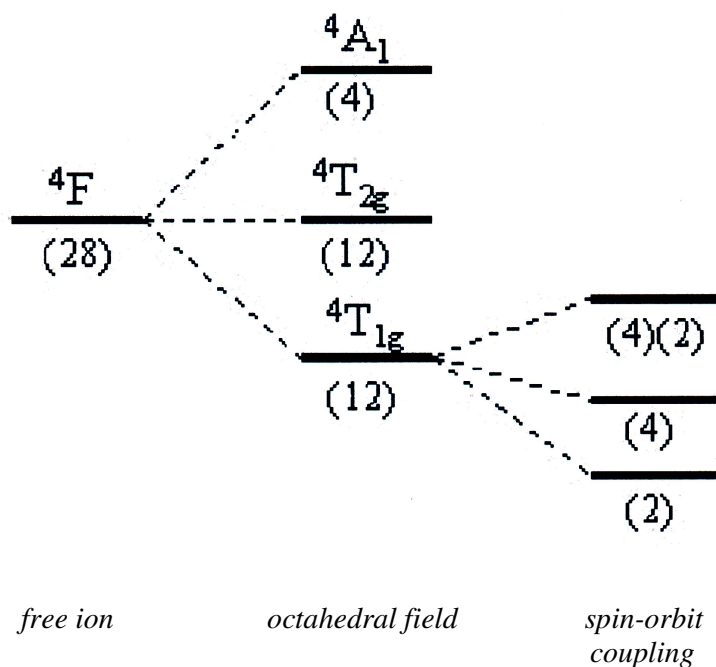


FIG.4.5 Sketch of the energy levels of bivalent Cobalt ions undergoing octahedral field and spin-orbit coupling.

4. Pure and Zinc-Doped CoPhOMe

with great efficiency the interaction along the chain and the electron delocalization permits the superposition of magnetic orbitals, due to unpaired electrons.

For a better understanding of the origin of intrachain interactions, the attention must be focussed on the particular case under discussion. In fact when a nitronyl-nitroxide radical centre interacts with a metal ion, the nature of the interaction depends on the overlap of the orbitals between the two centres involved [71-73]. It is anti-ferromagnetic if the molecular orbitals of the two centres are superimposed, while, if there is no superposition, the interaction is ferromagnetic. In CoPhOMe Cobalt(II), whose configuration is $[\text{Ar}]3d^74s^2$, presents, at high temperature, three unpaired electrons in the outer shell with a high orbital contribution displayed by its quantum numbers ($L_z=3$, $S=3/2$); the ground state of this ion, thought as free, is 4F . As already described, Cobalt is used to form octahedral compounds: the strongest perturbation acting on it is the octahedral crystal field which splits the original ground state in three degenerate levels with lower energy and two other levels, still degenerate, with higher energy. The crystal field, in most of the cases, results to be distorted and the perfect octahedral field is not a real situation. In fact, taking into account the spin-orbit coupling as a perturbation, $^4T_{1g}$, which is the ground level in octahedral symmetry, is split into three levels with the one having lower energy still degenerate. This electronic configuration leads to very important properties for metal centres in the sample. Also the theoretical model for the interpretation of the dynamics of the chain at low temperature derives from this property. In fact for $T < 50\text{K}$ just the ground state is populated and the Cobalt ion can be considered as possessing an effective spin $S=1/2$. This is no longer valid at high temperature, where excited states start being populated. The strong anisotropic exchange interaction between radicals and

4. Pure and Zinc-Doped CoPhOMe

Cobalt ions makes this chain a very good model system for investigating *Glauber dynamics*. All the features of the system can be summarized in the Hamiltonian:

$$H = \sum_i J(\vec{S}_{2i}^{\xi} \cdot \vec{S}_{2i+1}^{\xi} + \vec{S}_{2i}^{\xi} \cdot \vec{S}_{2i-1}^{\xi}) - \mu_B H^{\xi} \sum_i (g_{Co} \vec{S}_{2i}^{\xi} + g_{rad} \vec{S}_{2i-1}^{\xi}) \quad (4.1)$$

where the odd sites are the ones of the radical spins while the even sites represents the Cobalt ions spins and J represent the exchange coupling constant between nearest neighbours.

4.2 Macroscopic Measurements on Pure CoPhOMe

CoPhOMe is the first compound which displays a superparamagnetic slowing down of the magnetization as predicted by Glauber [1] in 1963 for ferromagnetic 1D Ising systems. The difficulty in observing the slow Glauber spin dynamics in a real Ising chain is due to the fact that the interchain interaction has to be so weak that the spin system does not undergo a 3D phase transition before the intrachain interaction induces the superparamagnetic freezing of the spins in the chain. CoPhOMe fulfils the two main conditions: a very *high magnetic anisotropy* of Ising type and a *very low ratio* between inter- (J') and intrachain (J) interactions i.e. $J'/J < 10^{-5}$. For example the CoPhOMe analogue, containing Mn^{2+} ions [71], does not show the phenomenon.

In this section a review of the previous results [23][58][74-80] obtained on pure CoPhOMe from DC and AC Susceptibility, NMR and μ SR measurements is shown. These results are the starting point for the interpretation of the data for Zinc-Doped compounds studied in this thesis. The macroscopic

4. Pure and Zinc-Doped CoPhOMe

measurements reported in the following have been performed by A. Caneschi and his co-workers of the University of Firenze and by E. Micotti of the University of Pavia.

4.2.1 Measurements in the Monomeric Compound

Preliminary information about CoPhOMe have been obtained from X-rays and DC Susceptibility measurements performed on the *monomeric sample* [75-76] constituted by a Cobalt(II) ion connected to two NITPhOMe radical centres. X-rays diffraction showed that this system has a structure resembling the one of the entire chain, so that it can be considered as a part of the chain with similar features. The most important information collected from the study of monomeric compound ($\text{Co}(\text{hfac})_2(\text{NITPhOMe})_2$) are:

- 1) the *Ising anti-ferromagnetic nature* of the nearest neighbour interactions along the chain between Cobalt ions and radicals.
- 2) the orientation of the *easy anisotropy axis* of the magnetization of each magnetic centre deviates considerably from the axis of the chain, forming a 45° - 55° angle with it.

As mentioned before the magnetic properties of interest refer to the low temperature range ($T < 50\text{K}$) where the chains can be considered a ferrimagnetic Ising system, with the Cobalt ions having an effective spin $S=1/2$ and an anisotropic g -factor ($g_{\text{Co}\perp}=0$, $g_{\text{Co}\parallel}=9$), and radical centres having $s=1/2$ and an isotropic g -factor ($g_{\text{rad}}=2$).

4. Pure and Zinc-Doped CoPhOMe

4.2.2 Susceptibility Measurements

DC Susceptibility

In FIGS.4.6-4.8 *DC susceptibility measurements* [74][77], performed on one and more iso-oriented single crystals, are shown.

The ratio between magnetization and the constant ($H=1\text{kOe}$)

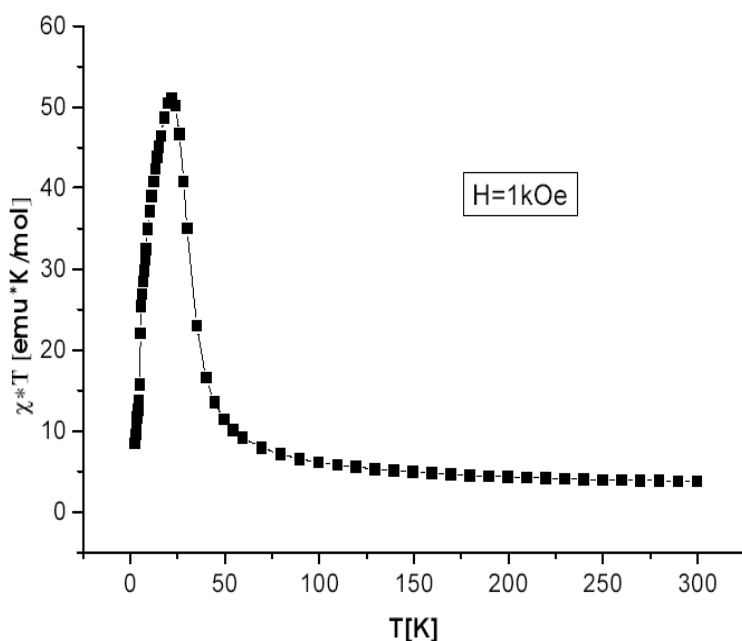


FIG.4.6 Temperature dependence of the ratio between magnetization and magnetic field applied along trigonal axis ($H=1\text{kOe}$) multiplied by temperature on a microcrystalline sample of CoPhOMe.

applied field multiplied by temperature increases with decreasing temperature: in particular the sudden increase below 100K clearly indicates *strong intrachain interactions* as already

4. Pure and Zinc-Doped CoPhOMe

observed for other 1D ferro- and ferrimagnetic systems. Susceptibility values at low temperature are much higher than for a system of non-interacting Cobalt(II) and radical centres. DC susceptibility measurements are well-fitted with an Ising model whose parameters are: $J=220\text{K}$, $g_{\text{Co}}=7.4$ and $g_{\text{Rad}}=2$ [23].

As can be seen from FIG.4.7, the magnetization is *strongly anisotropic* below 50K with the easy axis anisotropy corresponding to the trigonal axis.

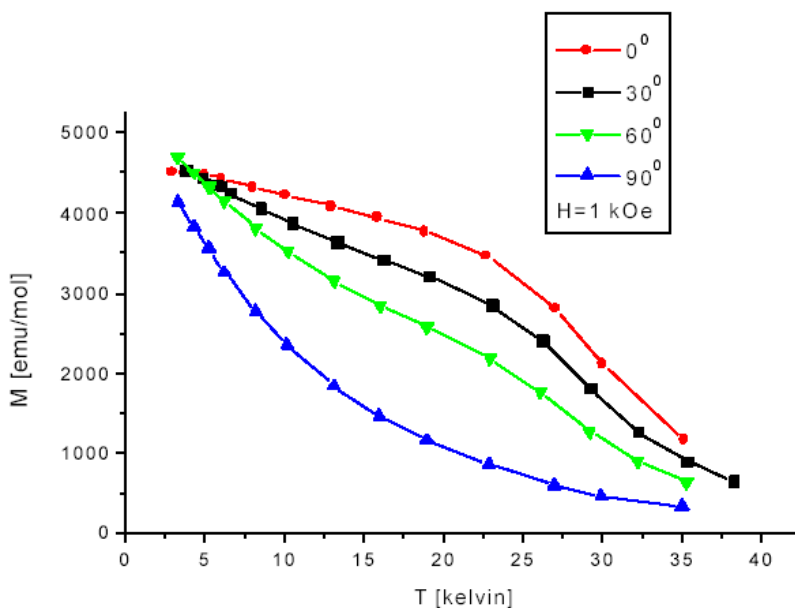


FIG.4.7 Magnetization as a function of temperature for various orientations of the external magnetic field $H=1\text{kOe}$ performed on a single crystal of CoPhOMe. The direction of the field is indicated by the angle between field itself and trigonal axis of the crystal. The strong anisotropy of the magnetization is evident.

The magnetization measurements performed in Pavia by Dr. E. Micotti [77] for six different magnetic fields show a shift of

4. Pure and Zinc-Doped CoPhOMe

the maximum with increasing the field magnitude. This behaviour is caused by *saturation effects* of the magnetization related, in Ising systems, to a damping in the susceptibility divergence with decreasing the temperature. The higher the field the higher is the temperature where the saturation effects start being dominant.

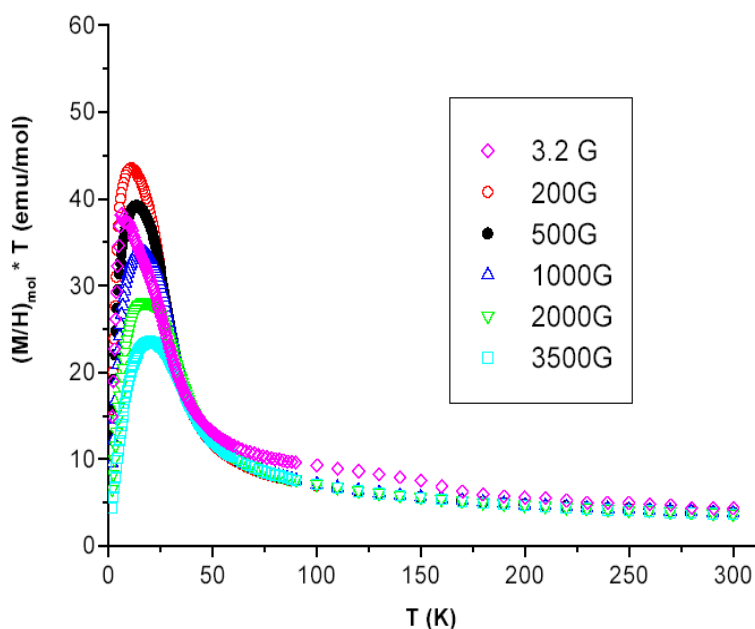


FIG.4.8 χT as a function of temperature for six different magnetic fields applied along trigonal axis. The graph shows the field dependence of the magnetization due to the saturation effects.

AC Susceptibility

CoPhOMe has been also investigated with AC susceptibility [74], in the frequency range 0.2Hz-500Hz, in order to detect the

4. Pure and Zinc-Doped CoPhOMe

dynamics of the spin system.

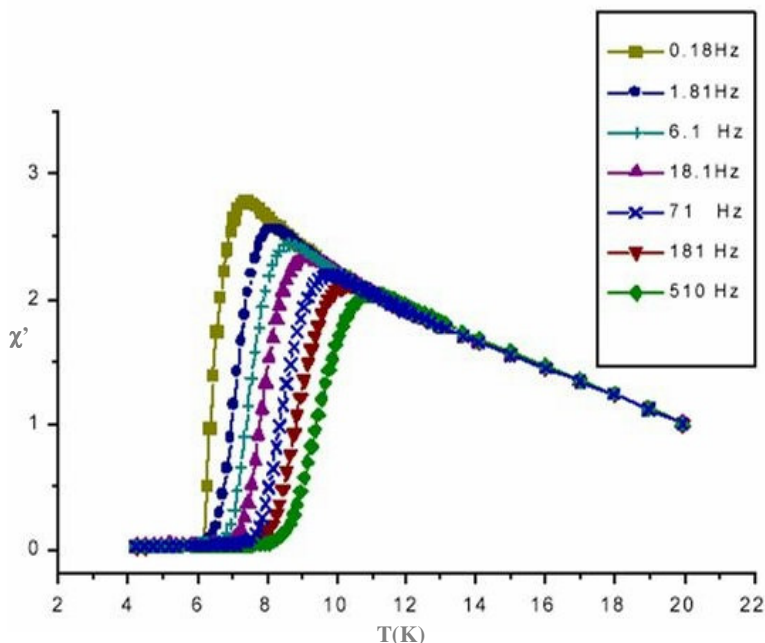


FIG.4.9 Real component of the AC susceptibility as a function of temperature measured for seven different frequencies. The T-dependence of χ' maximum rules out the occurrence of a 3D phase transition.

The real component (χ') of the AC susceptibility displays a peak for all of the seven frequencies of measurements. The important feature of these curves consists in the frequency dependence of the susceptibility below 12K with a peak which moves towards lower temperature for smaller frequencies.

The imaginary part of the AC susceptibility is characterized for all of the frequencies by a peak at temperatures close to the ones where χ' diminishes; also in this case the peak occurs at different temperatures for different measuring frequencies. This behaviour rules out the possibility of a phase transition, suggesting, instead,

4. Pure and Zinc-Doped CoPhOMe

that the dynamics of the magnetization reaches the same time scale of the measurements (2ms-10s) in the temperature range between 6K and 11K.

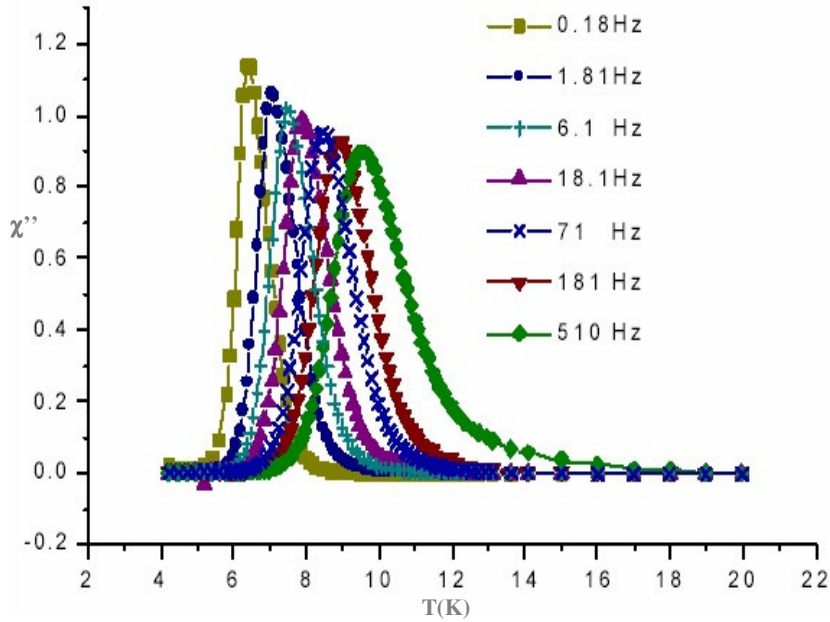


FIG.4.10 Imaginary component of the AC susceptibility as a function of temperature measured for seven different frequencies. The T-dependence of χ'' maximum suggests dynamic effects in the compound at low temperature.

The entire sample has the same blocking temperature, which is the temperature at which the spin system results to be frozen, as can be inferred by the semicircle form of the Cole-Cole plot [74]. Thus a single relaxation time τ can be extracted from the peaks in the susceptibility measurements.

When the relaxation time is plotted in a semi-log plot vs temperature one obtains a straight line, as can be clearly observed

4. Pure and Zinc-Doped CoPhOMe

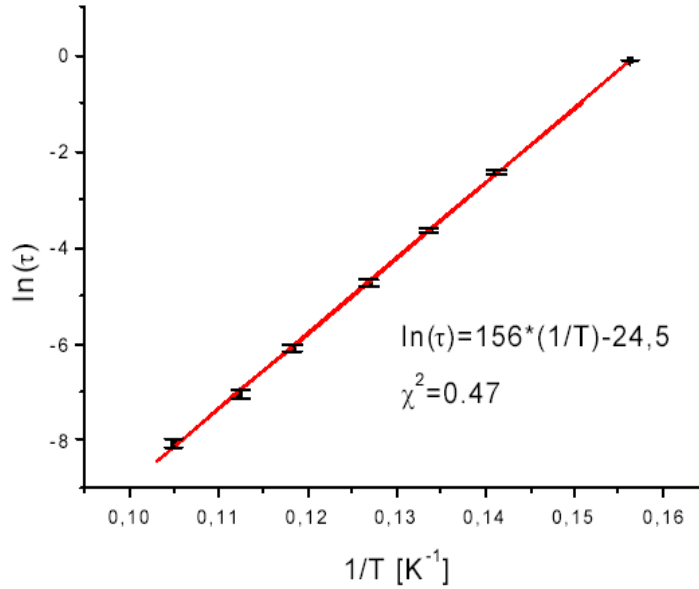


FIG.4.11 Logarithm of the relaxation time of the magnetization as a function of the inverse of the temperature.

in FIG.4.11, signalling an Arrhenius behaviour of τ whose equation is:

$$\tau = \tau_0 \exp\left(\frac{\Delta E}{k_B T}\right). \quad (4.2)$$

The experimental values are fitted well assuming in eq.(4.2) $\tau_0 = 3 \times 10^{-11} \text{ s}$ and $\Delta E = 156 \text{ K}$ [74]. The *pre-exponential factor* is comparable to the values for superparamagnetic systems. This characteristic is a further evidence of the fact that the magnetization follows a Glauber dynamics where the barrier of energy is represented by the exchange coupling constant J , through a thermally activated law:

4. Pure and Zinc-Doped CoPhOMe

$$\tau = \tau_0 \exp\left(\frac{4J}{k_B T}\right) \quad (4.3)$$

4.2.3 Magnetization Decay Method

The *relaxation time* at low temperature, i.e. well below the peak in the AC susceptibility, can be measured by monitoring the decay of the magnetization after a sudden variation of the magnetic field applied [74][77].

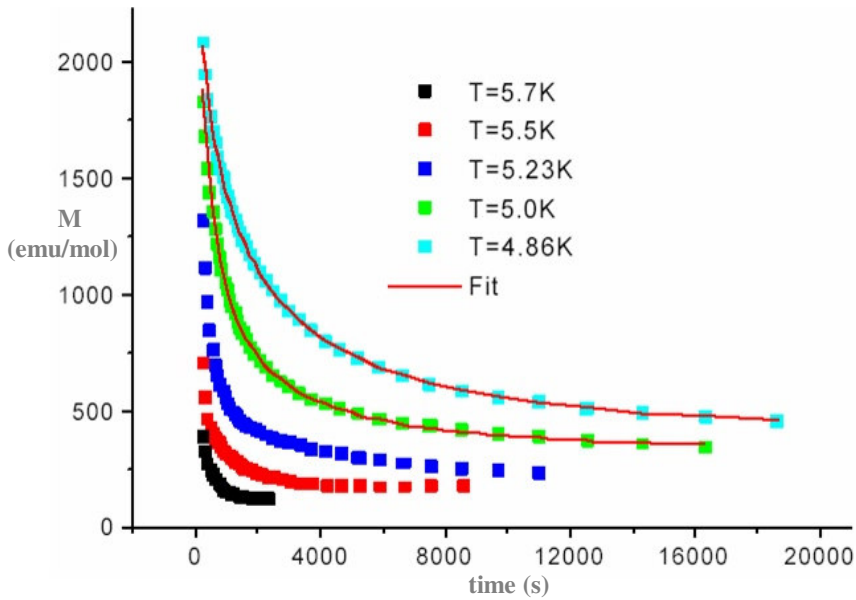


FIG.4.12 Magnetization decay along trigonal axis as a function of time in ZF, after saturating the sample with $H=30\text{kOe}$ in the temperature range 4.8-5.7K. Solid lines represent stretched exponential function fitting the data.

When a 30kOe magnetic field is applied along the trigonal axis and then switched off, the system is far from the equilibrium

4. Pure and Zinc-Doped CoPhOMe

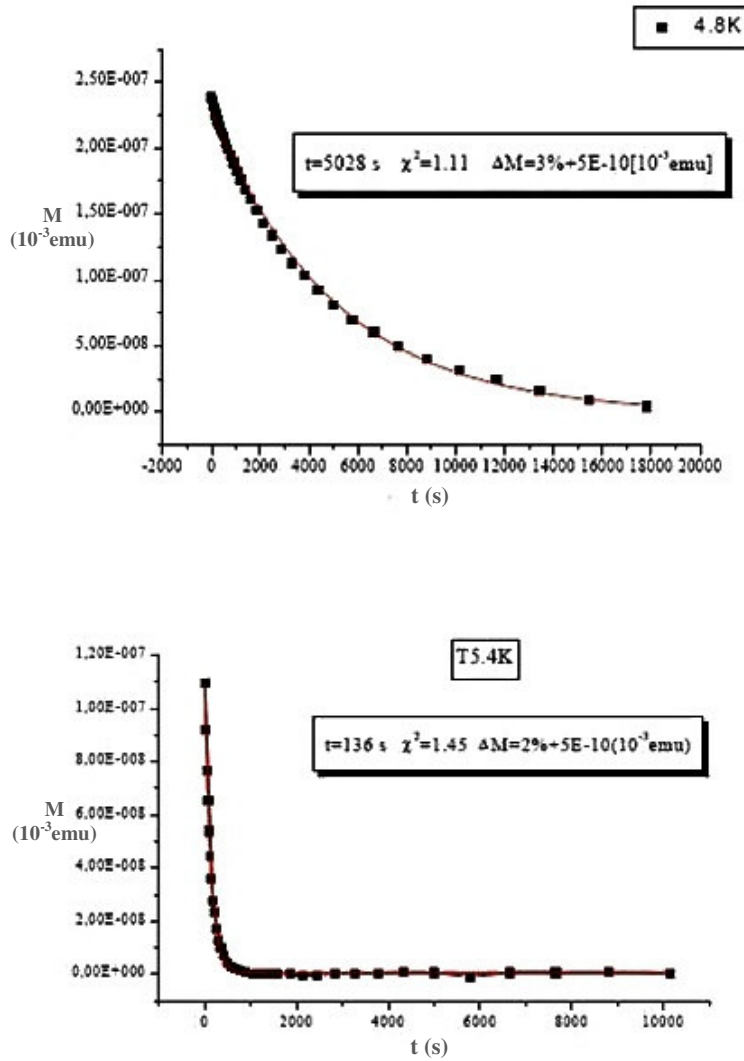


FIG.4.13 Decay of magnetization as a function of time in zero field applied after equilibrating magnetization by applying a 100e field along the trigonal axis of the system. Solid lines are the best fitting functions for each decay.

condition in zero field. In the range between 4.8K and 5.7K the deviation from the mono-exponential decay of magnetization,

4. Pure and Zinc-Doped CoPhOMe

proper of a system characterized by a single relaxation time, is evident. Just in the measurements at 4.86K and at 5K a stretched exponential fitting function

$$M(t) = [M(0) - M(\infty)] \exp \left[- \left(\frac{t}{\tau} \right)^\beta \right] + M(\infty) \quad (4.4)$$

can be used, suggesting a distribution of relaxation times.

By applying instead a lower magnetic field (100Oe), the initial condition is closer to the equilibrium condition and the single exponential behaviour is recovered.

Comparing the relaxation times obtained with this method with the ones expected from the extrapolation at low temperature of the AC susceptibility results, one finds a very good agreement: in fact from magnetization decay method the energy barrier varies between 156K and 159K, while from AC susceptibility it is found to be 156K.

4.2.4 Isothermal Magnetization

Preliminary results showed that the magnetization curves cannot be superimposed for $T < 6K$ [74]; that's why a series of *isothermal magnetization measurements* [23][74] have been performed at four different temperatures below the blocking temperature: as expected an *hysteresis loop* progressively opens up with decreasing temperature (see FIG.4.14 lower part), while no hysteresis has been detected when the magnetic field is oriented in the *trigonal plane* (see FIG.4.14 upper part). This behaviour is consistent with *hard-plane* like nature of the trigonal plane.

The saturation values in the hysteresis loop in FIG.4.14 (upper part) suggest a quite small anisotropy, since $M_{||} = 10390 \text{ emu/mol}$ and $M_{\perp} = 9680 \text{ emu/mol}$. This small difference, which could be an

4. Pure and Zinc-Doped CoPhOMe

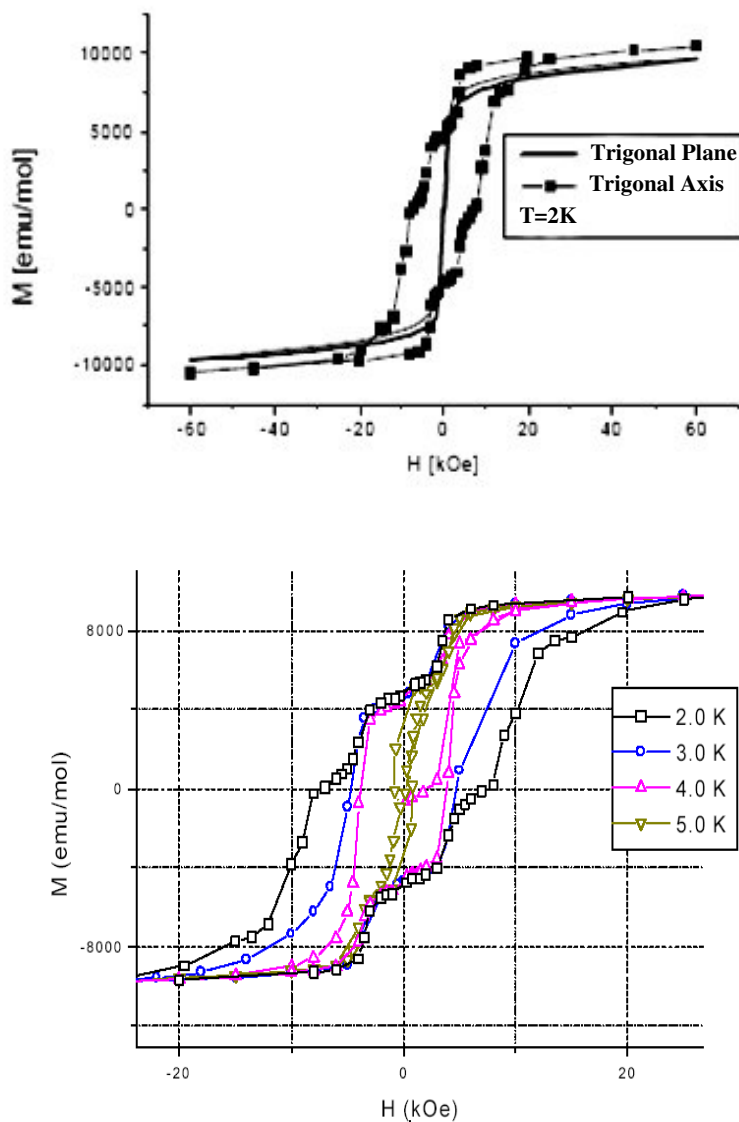


FIG.4.14 Isothermal magnetization at $T=2\text{K}$ with steady magnetic field applied both along and perpendicular to the trigonal axis (ABOVE). Isothermal Magnetization performed for four different temperatures with the field applied along trigonal axis: at $T=2\text{K}$ a second step appears (BELOW).

4. Pure and Zinc-Doped CoPhOMe

evidence against the use of Ising model for this system, is probably related to the *helical arrangement of the chain* that allows us to see just an average macroscopic anisotropy of the crystal, instead of the anisotropy of each magnetic centre. This kind of anisotropy is smaller if the local anisotropy directions, with respect to the trigonal axis are close to the magic angle 54.74° and this is the case of CoPhOMe as mentioned previously. Another unexpected feature characterizes isothermal magnetization around some thousands of Oe: it consists in the presence of plateaus whose number varies depending on the temperature [74]. For $T > 3\text{K}$ there is just one plateau around 4000Oe while for lower temperature another step has been found around 10000Oe (see FIG.4.14 lower part).

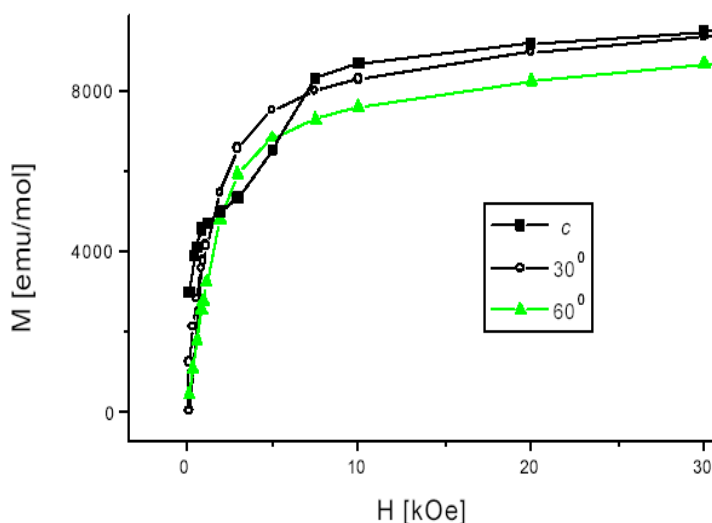


FIG.4.15 Isothermal magnetization at $T=8\text{K}$ measured along three different directions of the sample. The directions are indicated by the angle between the field orientation and the trigonal axis.

4. Pure and Zinc-Doped CoPhOMe

The origin of these steps has been tested from the performance of hysteresis loops with various sweeping rates (from 0.7kOe/s to 0.09kOe/s) [74] and no dynamical effects have been detected in correspondence of the plateaus previously recorded.

These steps could be due to the helical arrangement of the chain together with the anisotropic nature of the Cobalt ions and the reason of these plateaus can be related to the fact that for high magnetic fields the spins are driven by the strength of the field itself, while for low magnetic fields the anisotropy can be the driving force for the orientation of the magnetic moments, with the formation of *metastable states* suggested by the steps. The static origin of plateaus is proved by their presence in the plot also for temperatures above the blocking temperature, where the hysteresis loop is absent. All of these features disappear for temperature above 10K.

4.3 NMR Measurements

4.3.1 Introduction

In this section the results of *NMR measurements* done in Pavia by Dr. E. Micotti [77][79][80] will be summarized. Measurements include *^1H absorption spectra*, *spin-spin* and *spin-lattice relaxation rates* measurements as a function of temperature in the temperature range between ~300K and 1.5K for two different applied fields of $H=0.35$; 1.7Tesla.

4.3.2 ^1H NMR Spectra

From the observation of the spectra collected [58][77][79] for different applied magnetic fields and shown in FIG.4.16, the

4. Pure and Zinc-Doped CoPhOMe

most evident feature is the progressive broadening of the absorption line with decreasing the temperature.

The NMR line width in a paramagnet has two main contributions: a *field independent term* arising from the *nuclear dipole-dipole interaction* discussed in Chapter 2. In the proton NMR in molecular magnets this term is dominated by the proton-proton dipolar interaction within the organic molecular group. Thus it is of the same order of magnitude for all molecular magnets (about 25-30 KHz). If the molecular groups reorient fast enough this term can be substantially reduced. This, however, occurs most likely above room temperature. The other term is related to *the proton electrons dipolar interaction*. In this case the electron, polarized by the external field generates a local hyperfine field at the proton site which is proportional to the local paramagnetic moment i.e. χB . Thus the resulting line width is given by:

$$\delta\nu = (\delta\nu)_{dip} + A\chi B \quad (4.5)$$

where the constant A is an average hyperfine coupling constant between the nuclei and the magnetic moments. This result is the same for a single crystal and a powder sample. In fact the *paramagnetic broadening* is an inhomogeneous broadening due to the distribution of local fields at the different proton sites due to the presence of many *non equivalent protons* in the molecular magnet [56] with different dipolar fields resulting from the anisotropic character of the dipolar interaction. The increase in NMR line width on lowering the temperature reflects the increase of the susceptibility of the system. The field dependence of the FWHM vs B shown in Fig.4.17 follows from eq.(4.5) and the extrapolated value at $B=0$ yields the dipolar contribution to the line width, which can be estimated to be about

4. Pure and Zinc-Doped CoPhOMe

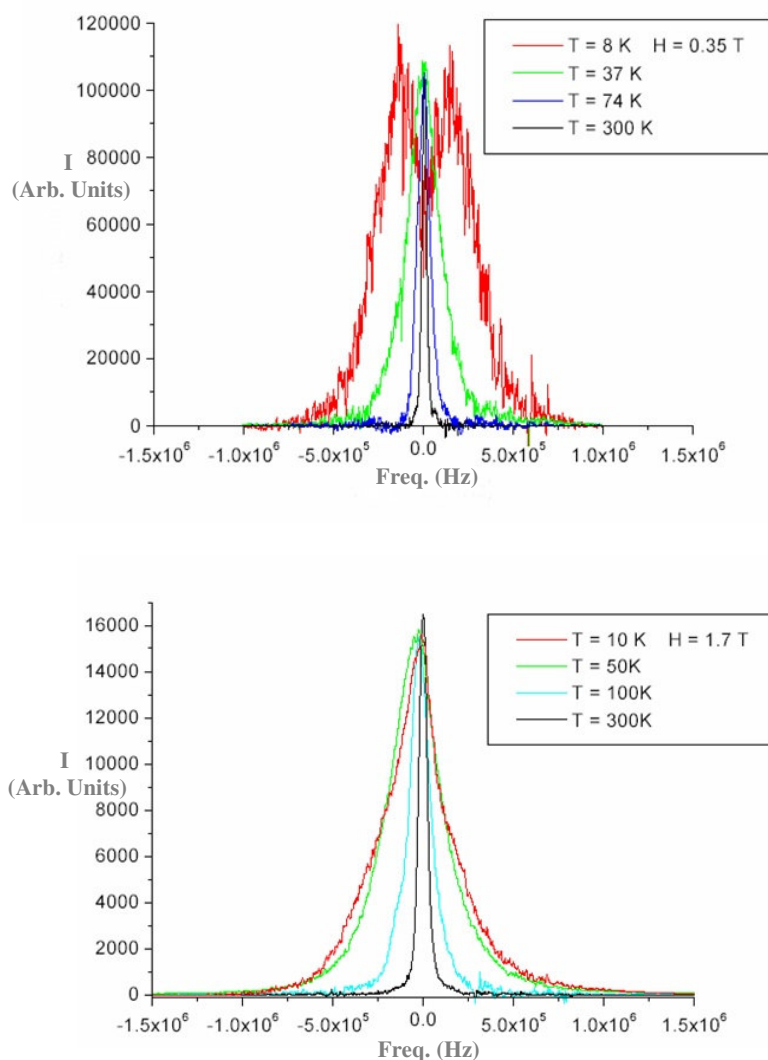


FIG.4.16 ^1H NMR absorption spectra for $H=0.35\text{T}$ (ABOVE) and for $H=1.7\text{T}$ (BELOW) for four different temperatures. The progressive line broadening with decreasing temperature is evident.

27kHz. This room temperature value could be slightly smaller than the rigid lattice value as the result of molecular reorientations.

4. Pure and Zinc-Doped CoPhOMe

If the proton is coupled to the magnetic moment by an *isotropic contact term* one can observe a shift since the local field is the same at all proton sites having the same coupling to the magnetic moment. This shift can be described by the equation:

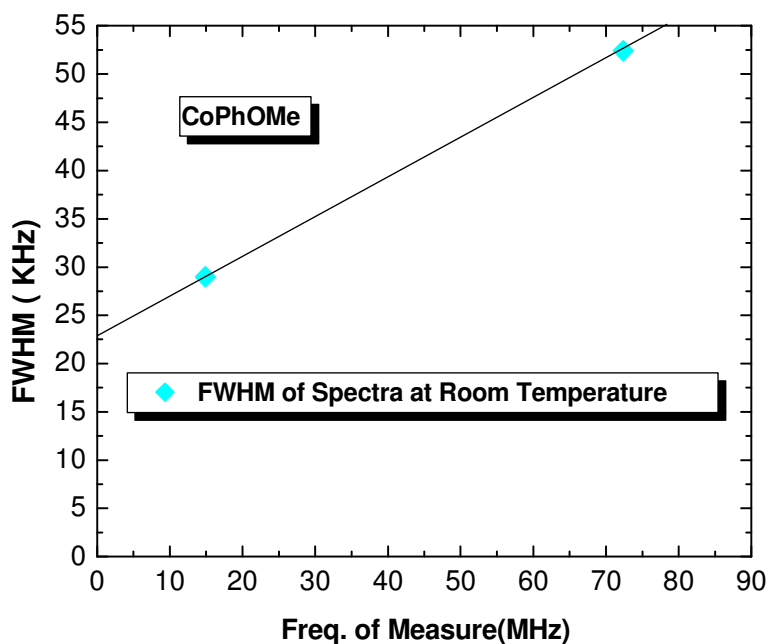


FIG.4.17 FWHM at Room Temperature for pure CoPhOMe at two frequencies of measure; the extrapolated FWHM at H=0 gives us a rough estimation of the dipolar contribution to the line width.

$$\nu = \frac{\gamma}{2\pi} (\nu_L + A' \langle \vec{s} \rangle) \quad (4.6)$$

where ν_L is the Larmor frequency, A' represents the isotropic hyperfine coupling and $\langle \vec{s} \rangle$ is the expectation value of the spins

4. Pure and Zinc-Doped CoPhOMe

oriented along the field direction. Since for protons A' is normally very small one expects a very small *paramagnetic shift*. This is shown in the experimental results of FIG.4.19.

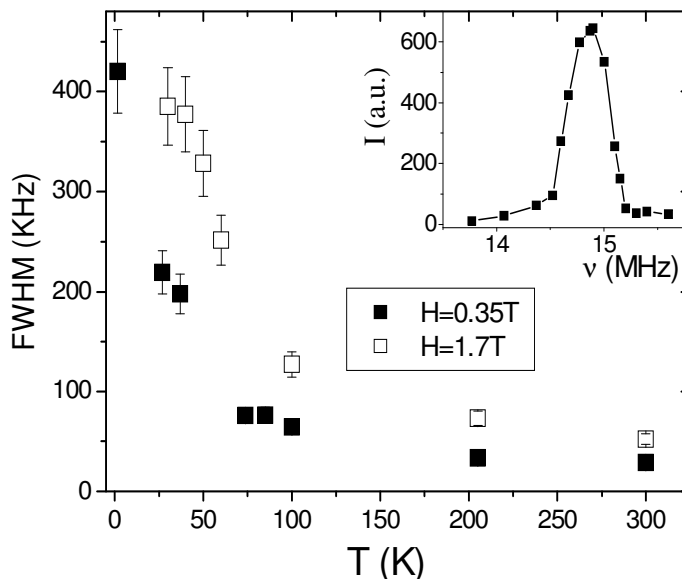


FIG.4.18 FWHM as a function of temperature for $H=0.35\text{T}$ and $H=1.7\text{T}$. Its rapid increase with decreasing temperature is shown. INSET: ^1H NMR absorption spectrum at $T=1.65\text{K}$ and $H=0.35\text{T}$ [58].

This small shift cannot be detected in low field measurements while for $H=1.7\text{T}$, the peak of the line shifts 40kHz below the Larmor frequency at low temperature.

At very low temperature, when the spin system freezes one expects a proton line width which is no longer proportional to the magnetic susceptibility and no longer proportional to the external field B . This is due to the fact that, in the frozen spin state, the local field is large and spontaneous namely largely independent of the applied field B . This effect has been seen clearly in single

4. Pure and Zinc-Doped CoPhOMe

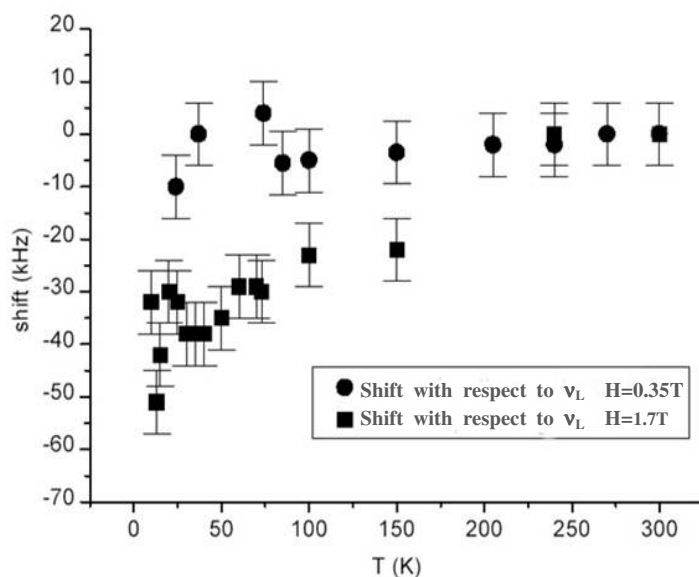


FIG.4.19 Line Shift as a function of temperature for $H=0.35T$ and $H=1.7T$ with respect to the Larmor frequency. No shift has been detected for lower field, while for higher field the line shifts till 40kHz below Larmor frequency when the temperature is decreased.

molecule magnets like Mn12 and Fe8 [81][82]. The onset of a spontaneous local field should also be observable in CoPhOMe at low temperature from the NMR line width measurements. However, the present data do not reach enough low temperatures to allow an analysis of the superparamagnetic slowing down on the NMR line width and shift.

4.3.3 Spin-Spin Relaxation Time T_2

A first investigation regarding the dynamics of the system can be done through the analysis of the relaxation time of nuclear transversal magnetization (T_2) [77].

As already mentioned in Chapter 2, spin-spin relaxation time is

4. Pure and Zinc-Doped CoPhOMe

proportional to the *spectral density* at frequency equal to zero ($T_2 \propto [J(0)]^{-1}$ [31]). The relaxation curves showed an exponential

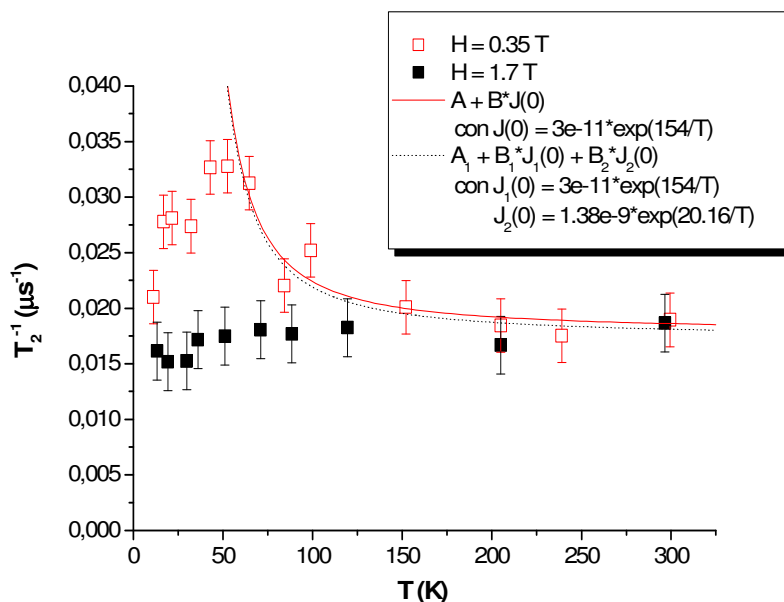


FIG.4.20 Spin-Spin relaxation rate as a function of temperature for $H=0.35\text{T}$ and $H=1.7\text{T}$ for NMR measurements on ^1H . In the figure are reported also the results of the best-fits performed and indicated by the lines on the graph.

behaviour as can be seen by plotting them in a semi-logarithmic graph, resulting in a straight line.

Depending on the magnetic field applied, the response of the system is different: for the highest field its behaviour is constant within the error bar, which suggests that the spectrum of fluctuations at frequencies close to zero is the same in all the temperature range investigated. Instead for $H=0.35\text{Tesla}$, $T_2(T)$ shows a large maximum around 50K (see FIG.4.20).

4. Pure and Zinc-Doped CoPhOMe

T_2^{-1} relaxation rate, can be written

$$\frac{1}{T_2} = A + \frac{1}{T'_2} = A + B \cdot J(0) = A + B\tau \quad (4.7)$$

where A refers to the *static contribution* while $1/T'_2$ is related to the *dynamic contribution* deriving from electronic spins.

The best-fit of these data has been done through two different procedures: for both of them a constant static contribution $A \sim 16\text{kHz}$ has been supposed, while for the dynamic term in the first case the fitting function was characterized by the Arrhenius law

$$\tau = \tau_0 \exp\left(\frac{\Delta}{T}\right) \quad (4.8)$$

as predicted in Glauber model; in the second case the dynamic term has been written as

$$B\tau = B_1 J_1(0) + B_2 J_2(0) = B_1 \tau_{0,1} \exp\left(\frac{\Delta_1}{T}\right) + B_2 \tau_{0,2} \exp\left(\frac{\Delta_2}{T}\right) \quad (4.9)$$

taking into account two different Arrhenius-like relaxation times. The static contribution is the contribution given to T_2 by the interactions between nuclear dipoles: the value used for the fit is in consistent with the one obtained from the line width of the spectra at room temperature though the procedure explained in the previous paragraph and in FIG.4.17. The results of the fit are summarized in FIG.4.20. There is a good agreement between eq.(4.9) and the data above 50K, while the maximum at lower temperature suggests that there is a different mechanism driving spin dynamics with respect to the one driving spin-lattice relaxation rate, as will be explain later.

4.3.4 Spin-Lattice Relaxation Time T_1

The recovery of the *nuclear magnetization* towards the equilibrium value after a saturation pulse is non-exponential but, rather, it follows a stretched exponential law like in the case of the recovery of the magnetization discussed in section 4.2.3. The origin of the stretched exponential is different in the two cases. In the case of the magnetization recovery it indicates a distribution of relaxation times of the magnetization itself, while in the NMR case it indicates a distribution of spin-lattice relaxation times. This second case can be explained simply by considering the distribution of proton sites with different couplings to the magnetic ions and thus different T_1 . If the different protons do not have time to reach a common *spin temperature* the recovery of the nuclear magnetization is given by the sum of exponentials i.e. a stretched exponential $\exp(-(t/\tau)^\beta)$. It should be noted that there is also the possibility that the distribution of NMR T_1 is related to the distribution of relaxation rates of the magnetization but it is impossible to discern the two cases.

In the case of stretched recovery of the nuclear magnetization it is customary to measure the slope of the tangent at the origin [58][79-80]. The relaxation rate obtained from the initial decay of the nuclear magnetization is a weighted average over all fast-relaxing protons.

The *Nuclear Spin Lattice Relaxation Rate* (NSLR), plotted in FIG.4.21 as a function of temperature, shows two main anomalies for $T < 50\text{K}$, where the compound can be considered as a one-dimensional ferrimagnetic Ising chain: at higher temperature both curves display a peak respectively at $T \sim 30\text{K}$ ($H=0.35\text{T}$) and at $T \sim 24\text{K}$ ($H=1.7\text{T}$) and for lower temperature ($T < 15\text{K}$) they show a pronounced shoulder.

The interpretation for the peak at $T > 15\text{K}$ has been done

4. Pure and Zinc-Doped CoPhOMe

identifying the correlation time τ , which enters in the theoretical expression of T_1 consisting in the so-called BPP law (BPP stands for Bloembergen Purcell and Pound [33]), which will be derived in Par.4.6.7, and whose expression is

$$\frac{1}{T_1} = A^2 \frac{2\tau_1}{1 + \omega_L^2 \tau_1^2} \quad (4.10)$$

with the macroscopic relaxation time of the magnetization $M(t)$ given by

$$\tau_1 = \tau_{0,1} \exp\left(\frac{\Delta_1}{T}\right). \quad (4.11)$$

It is noted that this assumption implies that the local spin-spin correlation function decays in time in the same way as the macroscopic magnetization correlation function.

The best fitting parameters are $A_1 = 3.0(\pm 0.1) \times 10^{11} \text{ rad s}^{-2}$, $\tau_{0,1} = 3(\pm 1) \times 10^{-11} \text{ s}$ and $\Delta_1 = 152(\pm 2) \text{ K}$ with a slight dependence of τ_0 on the applied field ($\tau_{0,1}(0.35 \text{ T}) = 3 \times \tau_{0,1}(1.7 \text{ T})$) and on the *thermomagnetic history* of the sample, but in good agreement with susceptibility results. The local character of the NMR spectroscopy has allowed the detection of a relaxation mechanism which was undetected in the first magnetization relaxation measurements. In fact the shoulder in the plot of NSLR vs T suggests the presence of a different mechanism with a different correlation time which reaches the radiofrequency range only below 10K.

To fit the shoulder of the NSLR data we assume the usual Arrhenius law $\tau_2 = \tau_{0,2} \exp\left(\frac{\Delta_2}{T}\right)$ but with a distribution of energy Barriers Δ_2 , of width δ_2 . The data for $T < 50 \text{ K}$ are quite well-fitted

4. Pure and Zinc-Doped CoPhOMe

by the total equation:

$$\frac{1}{T_1} = A_1^2 \frac{2\tau_1}{1 + \omega_L^2 \tau_1^2} + A_2^2 \left\{ \left(\frac{1}{2\omega_L \ln b_2} \right) [\arctan(b_2 \omega_L \tau_2) - \arctan(\omega_L \tau_2 / b_2)] \right\} \quad (4.12)$$

where $b_2 = \exp(\delta_2/T)$. In this expression the hyperfine coupling

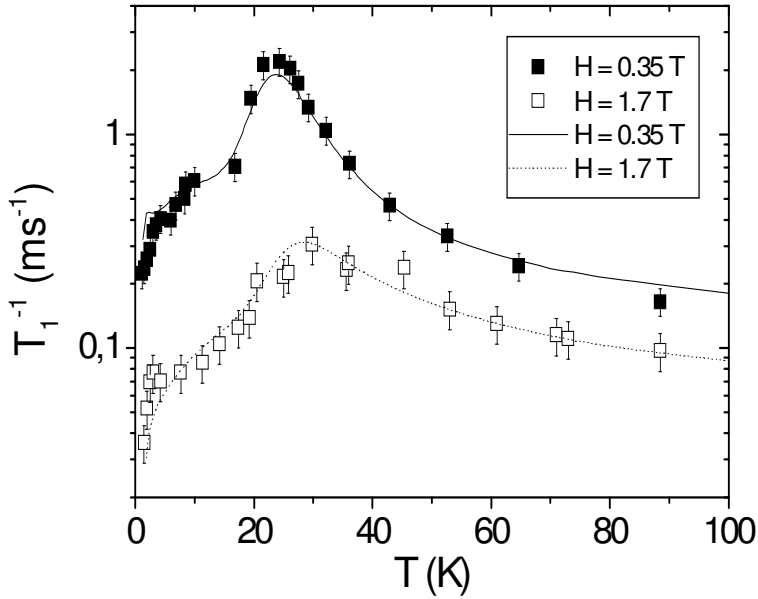


FIG.4.21 Spin-Lattice relaxation rate as a function of temperature for $H=0.35\text{T}$ and $H=1.7\text{T}$ for NMR measurements on ^1H . The solid and dashed lines on the graph represent the behaviour of the best-fits described in the text [79][80].

constant A_1 and A_2 are assumed to be temperature independent and Δ_1 and Δ_2 field independent. The results of the fit regarding the second relaxation mechanism are: $\tau_{2,0} = 9(\pm 0.5)\text{K}$,

4. Pure and Zinc-Doped CoPhOMe

$\delta_2=20(\pm 0.5)\text{K}$, $A_2=1.8(\pm 0.2)\times 10^{11}\text{rad sec}$ with τ_2 following the same field dependence as τ_1 discussed above. The scarce agreement between fits and data for $T>50\text{K}$ is due to the fact that the model used for low temperature, taking into account for the Cobalt spins a value equal to $1/2$, cannot be anymore used, since for higher temperatures the excited levels of the Cobalt ions start to be populated, the distance between the ground state and the first excited level being about 150K .

It must be remarked that the choice of a distribution of energy barriers in eq.(4.12) could be justified, since it can correspond, phenomenologically, to the excitations at different wave vectors in the generalized susceptibility which can be detected by the local probe constituted by protons in NMR spectroscopy.

4.4 μSR Measurements

Measurements discussed in this paragraph have been done by Dr. E. Micotti [58][80] in the temperature range $4\text{K} \leq T \leq 300\text{K}$ in the so-called *longitudinal configuration*, i.e. with different magnetic fields ($H=2000, 3500\text{Gauss}$) applied in the same direction of the muons initial polarization. Depolarization curves behaviour has been analyzed as a function of temperature.

From the measurements presented in previous paragraphs, it's evident that the behaviour of CoPhOMe can be divided into two main temperature ranges:

- 1) **$T>50\text{K}$** : the system is paramagnetic
- 2) **$T<50\text{K}$** : progressive electronic spin freezing takes place

Following the μSR experimental results the behaviour of the

4. Pure and Zinc-Doped CoPhOMe

muon polarization $P(t)$ in the two different temperature regions, in ref. [80] was described by the following equations:

$$P(t) = Ae^{-\lambda t} + B \quad T > 50K \text{ PARAMAGNETIC REGION} \quad (4.12a)$$

$$P(t) = Ae^{-\lambda t} + G_{KT}(t) \cdot A'e^{-T^{-1}/KT} + B \quad T < 50K \text{ SPIN FREEZING} \quad (4.12b)$$

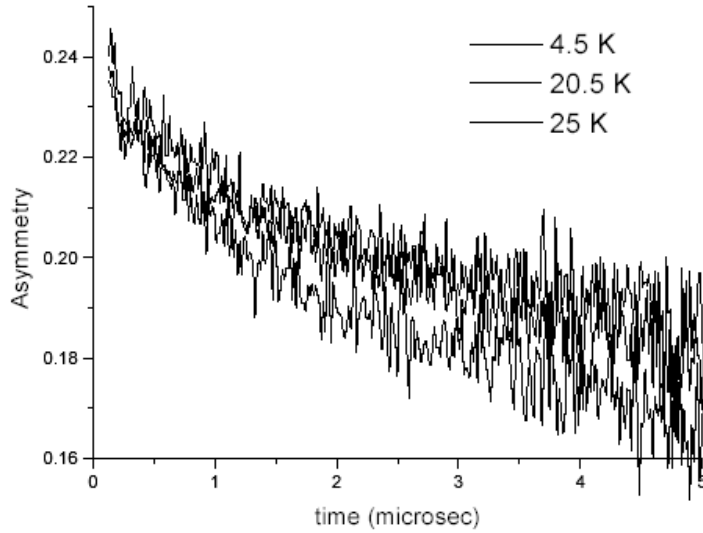


FIG.4.22 Depolarization curves of the muon in a longitudinal field of $H=3500$ Gauss at different temperatures on CoPhOMe.

where A is a constant parameter and B is the background due to the sample holder contribution, assumed to be nearly constant with respect to temperature and applied magnetic field. By the observation of crystal structure of CoPhOMe, one can evince a-priori that more than one equivalent muon site is present. From Eq.(4.12a), we deduced that in the paramagnetic region the behavior of $P(t)$ is monoexponential, i.e. the muons in different

4. Pure and Zinc-Doped CoPhOMe

sites have common spin temperature. On the other hand in the spin freezing region the muons implant in at least two different sites, as witnessed by the two components in $P(t)$. In eq.(4.13b) λ represents a relaxation rate associated to an exponential decay of $P(t)$. The second term in Eq.(4.13b), $G_{KT}(t) \cdot A' e^{-T^{-1}_{1KT} t}$ represents a *Kubo-Toyabe static function* $G_{KT}(t)$ multiplied by an exponential decay term $\exp(-T^{-1}_{1KT} t)$. The function G_{KT} depends on t and Δ where Δ is the FWHM of the Gaussian or Lorentzian *local static field distribution*. This function gives an indication of the local field distribution evidenced in particular by a minimum occurring at short times. Despite to the absence of the minimum in the RAL experimental data of ref. [80] (explained by the impossibility of collecting data at short times $t < 80$ ns, with a pulsed muon source), the use of KT function in the fitting of $P(t)$ was justified by the progressive decrease of the muon total asymmetry and the increase of the background with field increasing, when the temperature is decreased below 50K. λ and T^{-1}_{1KT} , the inverse of the relaxation times of two different muon groups, can be treated both like the nuclear spin-lattice relaxation rate T^{-1}_1 in NMR measurements. They give information on the *electronic spin dynamics* such as NSLR, even if muons stop in different position inside the sample with respect to protons. In fact, because of their positive charge they thermalize in an environment negatively charged where they can minimize the potential energy.

The temperature behaviours of λ and T^{-1}_{1KT} at the applied fields are qualitatively the same. In Fig. 4.23 the behaviour of $T^{-1}_{1KT}(T)$ is reported ($\lambda(T)$ not reported). As can be easily seen, two anomalies for $T < 50K$ can be pointed out: for $T > 15K$ a maximum and for $T < 15K$ a broad shoulder. These results are similar to the ones collected with NMR proton spin-lattice relaxation rate measurements. The solid lines in Fig.4.23 correspond to the

4. Pure and Zinc-Doped CoPhOMe

fitting performed using the same relaxation times used for NMR data, i.e. Arrhenius-like τ_1 and τ_2 (see previous paragraph) with the proper renormalization of the hyperfine constants.

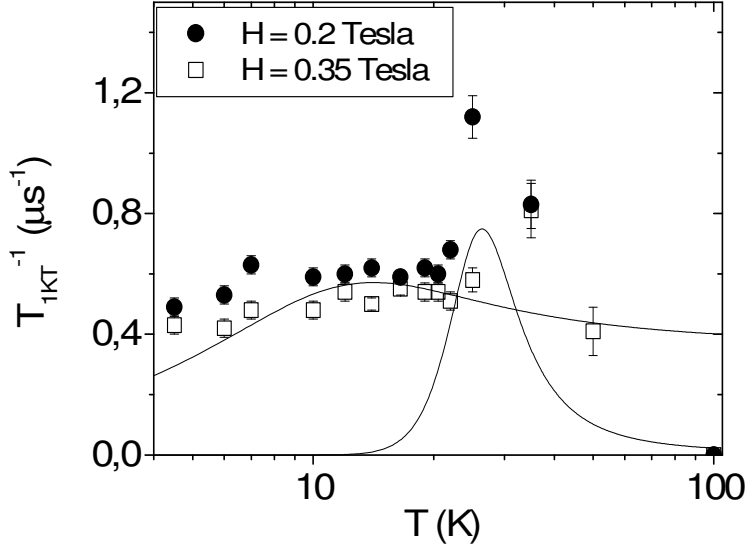


FIG.4.23 Muon relaxation rate multiplying the Kubo-Toyabe function, reported as a function of temperature for $H=0.2T$ and $H=0.35T$. The solid lines are the best-fits as described in the text [80]. The behaviour of the second relaxation rate of Eq.(4.13b) is qualitatively the same.

For the sake of completeness, we would like to remark that recent PSI data, still not analysed, showed that the muon asymmetry does not display any KT-like behaviour neither for times $t < 80$ ns. However, by substituting Eq.(4.13b) with a bi-exponential function $C \exp(-\lambda_1 t) + D \exp(-\lambda_2 t)$, preliminary fits allowed to verify that the temperature behaviour of the relaxation rates extracted from PSI data, λ_1 and λ_2 , is similar to the ones of λ and T_{1KT}^{-1} , thus validating the qualitative conclusions of the

4. Pure and Zinc-Doped CoPhOMe

present paragraph (the slight increase of the background we talked about above, can be justified by the *change of asymmetry* predicted with field increasing). For a more detailed discussion about the physical meaning of the used fitting function of PSI data, more data elaboration is needed (in progress).

4.5 Conclusions

After this first run of measurements [23][58][74-80] for the characterization of the properties of **pure CoPhOMe**, a lot of information have been obtained regarding this molecular magnet, both from macroscopic measurements, consisting in Magnetization and DC and AC Susceptibility measurements and microscopic measurements such as NMR and μ SR experiments. The most important characteristic pointed out has been the Ising 1D behaviour of CoPhOMe in all the temperature range investigated (1.5-300K).

It consists in the extreme *slowing down* of the magnetization, following a *thermally activated law* ($\tau=\tau_0\exp(\Delta/T)$), which occurs at low temperature before any 3D phase transition could take place: this is the first experimental verification of the slowing down in single chain magnet predicted by Glauber in 1963 [1]. This feature has been pointed out by the relaxation time extracted from AC susceptibility measurements [23][74]. An important evidence for a spin freezing of the electronic spins in the time scale of the experiments performed has been displayed by AC susceptibility and isothermal magnetization measurements [23][74]: in the first case, it has been suggested by the frequency dependence of the peak in the out-of-phase component χ'' , and in the second case, by the hysteresis loop appearing at temperatures below 6K.

The possibility of a distribution of relaxation processes and, as a

4. Pure and Zinc-Doped CoPhOMe

consequence, of different relaxation times, related to the non-exponential behaviour of the magnetization relaxation curves, has been first confirmed by NMR microscopic measurements [58][79-80]. In fact, plotting *spin-lattice relaxation rate*, below 50K two different relaxation mechanisms have been displayed in the form of a pronounced peak for $T > 15\text{K}$ and a broad shoulder at $T < 15\text{K}$. The identification of these processes as related to the electronic spins dynamics has led to the assignment, for each mechanism, of a correlation time thermally activated behaviour as for the relaxation of the macroscopic magnetization. The insertion of the Arrhenius expression for the relaxation time in the *BPP fitting function*, suggested that there are two different regions in the sample where two different electronic dynamics are present.

These two different correlation times detected by NMR NSLR can be tentatively assigned to the electronic spin dynamics of the two sublattices composing the sample: in fact Co^{2+} ions sublattice and radical centres sublattice, even if they are both characterized by $S=1/2$, they have really different Landé factors. The high sensitivity of ^1H NMR measurements can be related to the fact that two of the 21 non-equivalent protons in the sample [56], the ones of the *hfac* group, are close to Cobalt ions so that they feel their dynamics, while all of the other protons closer to radical centres reflects the radical dynamics. This spin dynamics picture has been further confirmed by μSR measurements [58][80] and in particular by the behaviour of the relaxation rates (T^{-1}_1 and λ) of muons extracted from fitting functions used for the muon depolarization: for both the longitudinal fields used in the experiments ($H=0.2\text{T}$, 0.35T) for $T > 15\text{K}$ a peak is present while for $T < 15\text{K}$ a broad shoulder is evident. This result implies that the muons implant in two different site, which still could be related to the two sublattices of the system.

4. Pure and Zinc-Doped CoPhOMe

This last conclusion is still debate, since there are some open questions on the real behaviour of the electronic dynamics: in fact, as regards NMR, the field dependence of the relaxation time is not clear. In fact fits are not so good in NMR especially for $H=1.7T$.

4.6 Zinc-Doped CoPhOMe

4.6.1 Introduction

After the intense research dedicated to Pure CoPhOMe where the slowing down of the magnetization predicted by Glauber [1] has been evidenced experimentally, the attention has been focussed on the same 1D magnetic chain compound doped with Zn diamagnetic impurities in order to investigate the finite-size (length of the chain) effects on the spin dynamics. The static and dynamic properties will be analyzed with both DC and AC Susceptibility measurements and with local NMR spectroscopy, the interpretation of the data being still in progress.

4.6.2 General Features

Various concentrations of *Zinc diamagnetic ions* have been inserted in the pure sample: this procedure has been done by adding to the solutions used for the pure sample various quantities of $Zn(hfac)_2 \cdot 2H_2O$ vs $Co(hfac)_2 \cdot 2H_2O$ [83-84]. It has been found from measurements with PIXE [85] (particle induced X-ray emission technique) that the concentration of Zinc in the sample was always lower than in the starting solutions. With PIXE also the distribution of the dopant in longitudinal and in transverse direction for single crystals has been controlled: it

4. Pure and Zinc-Doped CoPhOMe

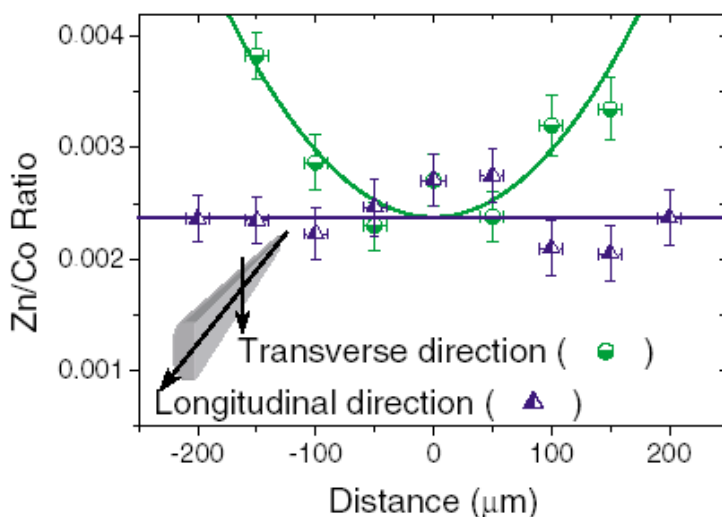


FIG.4.24 Spatial distribution of Zn/Co ratio in CoPhOMe doped samples in the transverse and in longitudinal direction [83][84].

resulted that the distribution in the longitudinal direction is in practice uniform while in the transverse direction it increases from the centre to the edges. The problem with this kind of compounds is also related to reproducibility of the concentration in different crystals deriving from different batches, whereby it is reproducible in the same batch with an uncertainty of 5%.

The importance of the doping in such compounds is crucial, because all their morphological characteristics are varied. Starting from the pure compound which can be thought as formed by chains of more than 3000 spins i.e. infinite chains, one can reduce the length of the chains by doping. For Zn=0.3% and Zn=5.4% the chains have of about 200 and 15 spins respectively. The concentrations studied experimentally here are Zn=0.3, 1.9, 4.7, 5.4%. In this chapter we are interested in particular in the *dynamics* of these new systems and in the way the dynamics

4. Pure and Zinc-Doped CoPhOMe

changes in comparison with the one of the pure compounds and with increasing the doping concentration. The most important assumption to be done in the analysis of the doped samples, is considering the sample as made up of non interacting segments, that is to say, not taking into account 3D interactions.

4.6.3 DC Susceptibility Measurements

For a first characterization of the doped CoPhOMe compounds we have performed *DC susceptibility measurements* in the temperature range between 2K and 300K with three different magnetic fields of 500, 3500, 16500G applied on powders samples with a percentage of Zinc of 1.9% and 5.4%.

In FIG.4.25 the behaviour of the molar susceptibility multiplied by temperature as a function of temperature itself is shown.

The magnetic fields of the measurements have been chosen for a comparison with NMR measurements that have been performed with the same applied fields.

As can be clearly seen from the graph, the results on powder sample used for these measurements resemble to the ones obtained in the pure compound. In particular, for low applied fields, it can be noticed that below 100K the susceptibility starts increasing abruptly giving a clear indication of *strong intrachain interaction* as in the pure compound and characteristic of 1D ferro- and ferrimagnets. Also in the doped chains case the lack of a minimum in the susceptibility curve is against the hypothesis of the 1D ferrimagnetic system. This absence can be, anyway, justified by the high intrachain coupling constant which causes the minimum to be above the highest temperature limit (300K) of this experiment. Another interesting feature is related to the fact that, with increasing field, the peak shifts at higher temperature (from $T \sim 12\text{K}$ for 500Gauss to $T \sim 32\text{K}$ for 16500Gauss) as the

4. Pure and Zinc-Doped CoPhOMe

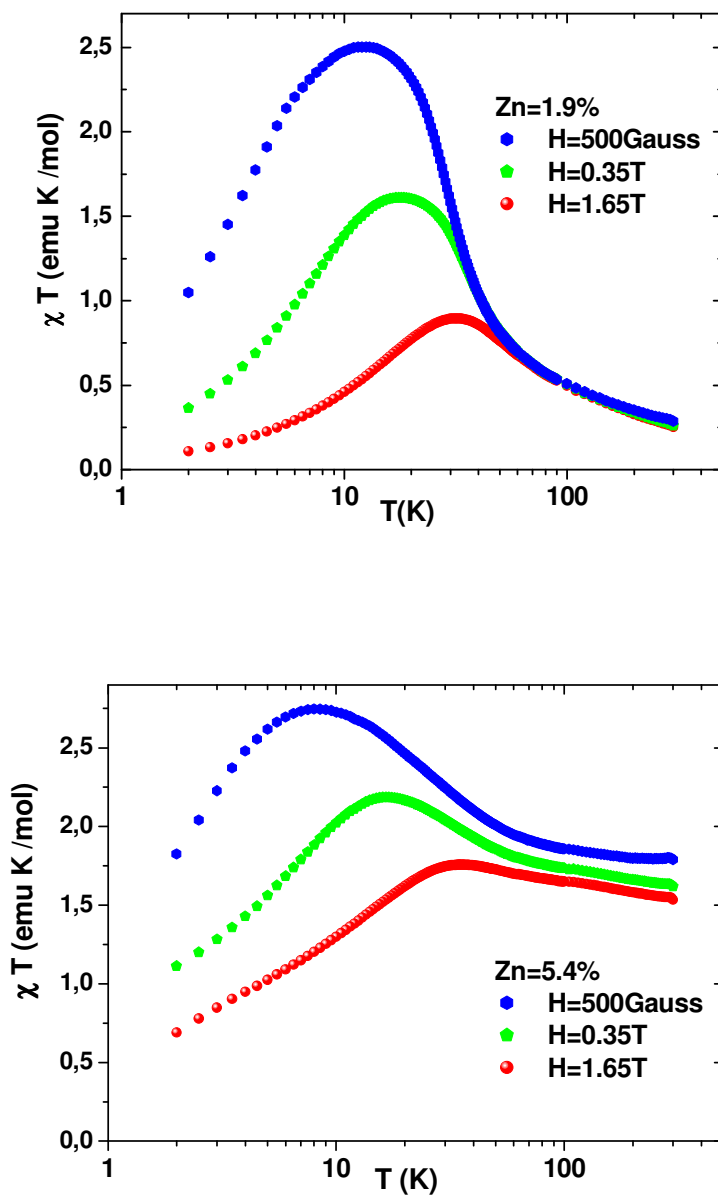


FIG.4.25 Molar susceptibility multiplied by the temperature as a function of temperature of CoPhOMe powders doped with Zn=1.9% and Zn=5.4% for three different static magnetic fields.

4. Pure and Zinc-Doped CoPhOMe

result of *saturation effects* characteristic of *strong short range order* within the segments. This behaviour has been observed also in the compound doped with Zn=5.4%, but with a slight field dependence of unknown origin also at high temperature (see also Par.4.6.6). These features seem to suggest that doped compounds don't show sizeable differences with respect to the pure compound as regards the static properties, even when the chains are broken in very short segments.

4.6.4 AC Susceptibility Measurements

In this paragraph the spin dynamics of the sample is investigated through *AC susceptibility* [83-84] [86-87] with new runs of measurements also on Pure CoPhOMe done at University of Firenze. Measurements have been performed for more than one run on samples with various concentrations of Zinc: in particular AC susceptibility measurements have been performed in compounds with Zn=0.3, 1.9, 4.7%.

The spin dynamics in Ising chains of finite length was also investigated theoretically by using the Glauber model [1]. From transition probabilities calculated by Glauber [1] the equation of motion for spins, under free boundary conditions [52][88], can be expressed by the matrix equation

$$\frac{d}{dt}\vec{S} = -\vec{M}'\cdot\vec{S} \quad (4.14)$$

where $\vec{S}=(s_1,\dots,s_N)$ is a vector with dimensionality N , while \vec{M}' is a real quasi-symmetric tridiagonal $N\times N$ matrix whose expression is

4. Pure and Zinc-Doped CoPhOMe

$$\vec{\vec{M}}' = \begin{pmatrix} 1 & -\beta & 0 & 0 & \cdots & 0 & 0 \\ -\gamma & 1 & -\gamma & 0 & \cdots & 0 & 0 \\ 0 & -\gamma & 1 & -\gamma & \cdots & 0 & 0 \\ \vdots & \vdots & \ddots & \vdots & & & \\ 0 & 0 & 0 & 0 & \cdots & -\beta & 1 \end{pmatrix}. \quad (4.15)$$

where $\gamma = \tanh(2J/k_B T)$ $\beta = \tanh(J/k_B T)$.

The eigenvalues spectrum can be written, after some algebra,

$$\lambda_L(\theta) = q \alpha_0 [1 - \gamma \cos \theta] \quad (4.16)$$

where q represents the probability of reversal of a single spin of the chain in the unit time $1/\alpha_0$ and θ is one of the L roots of the transcendental equation

$$\tan(L\theta) = \frac{-2 \coth(\xi^{-1}) \tan \theta}{1 - \coth^2(\xi^{-1}) \tan^2 \theta} \quad (4.17)$$

used by Luscombe [89] where ξ is the correlation length.

The relaxation time $\tau_L(T)$ of a segment of length L is related to the smaller eigenvalue of the matrix $\vec{\vec{M}}'$: when $L \gg 1$ the expansion of this eigenvalue leads to different expressions for relaxation time [88-89]:

$$\tau_L(T) \approx \xi^2 \quad \xi \ll L \quad \rightarrow \quad \tau_L(T) \propto \exp(4J/k_B T) \quad (4.18a)$$

$$\tau_L(T) \approx L\xi \quad \xi \gg L \quad \rightarrow \quad \tau_L(T) \propto \exp(2J/k_B T) \quad (4.18b)$$

4. Pure and Zinc-Doped CoPhOMe

being $\xi \sim \exp(2J/k_B T)$, with J representing the nearest neighbour exchange coupling constant.

This theoretical discussion shows that there are two distinct regions depending on the L/ξ ratio. In fact the relaxation time of equation (4.18a) is the one expected for the infinite system, i.e. for infinite chains as in the pure CoPhOMe, where the length of the chain is longer than the correlation length along the chain, while for doped sample the correlation length becomes longer than the length of the segments. In practice, even if Glauber dynamics is still valid, in the second regime the energy barrier is halved [83-84][86] as can be seen from FIG.4.26. In this figure the solid lines have been obtained by the position of the peak

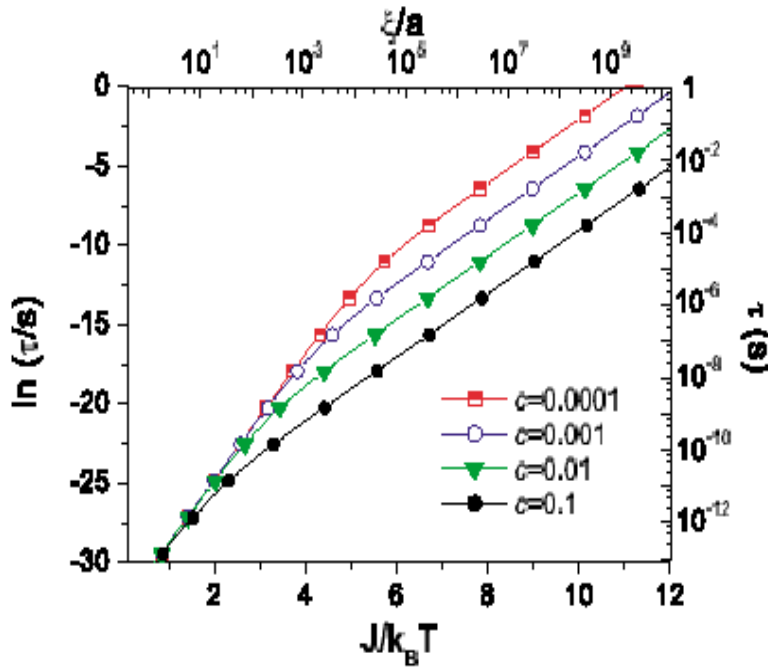


FIG.4.26 Logarithm of the relaxation time τ as a function of $J/k_B T$. These results have been extracted from eq.(4.19) with $\alpha_0 = 3.6 \times 10^{13} \text{ s}^{-1}$, $J/k_B = 80 \text{ K}$ and $q = 0.73$ [83].

4. Pure and Zinc-Doped CoPhOMe

from the *frequency-dependent susceptibility function*

$$\chi(\omega, T) = \frac{c^2}{Z_c} \sum_{L=1}^{\infty} \frac{\chi_L(\omega, T)}{1 - i\omega\tau_L} (1 - c)^L \quad (4.19)$$

where c is the impurities concentration, $\chi_L(\omega, T)$ is the susceptibility from the Ising model for a chain of length L calculated by Wortis [52] and

$$Z_c = c^2 \sum_{L=1}^{\infty} (1 - c)^L \quad (4.20)$$

is the *normalization factor*.

Experimental measurements have been performed on pure compound and on doped samples with three different impurities concentration (Zn=0.3; 1.9; 4.7%) [83-84][86] and for seven different frequencies in the range between 10Hz and 10kHz. The behaviour of both components of the susceptibility has been studied. The *imaginary part* χ'' as a function of temperature shows a maximum for each frequency ω of the AC field applied for low concentrations while for highest concentration the curves are distorted and presents also a little shoulder at low temperature; from these plots the relaxation time of the magnetization can be extracted from the condition $\tau^{-1}(T_{\max}) = \omega$. The results are displayed in FIG. 4.27. From the fit of the data to the equation $\tau = \tau_0 \exp(\Delta E / T)$, both the energy barrier ΔE and the pre-exponential factor τ_0 can be estimated.

All the data in FIG.4.27 lie on a straight line indicating that the thermally activated mechanism is valid for both the pure and the doped samples. All the lines for all the samples studied have the same slope; from this slope the energy barrier can be extracted and since all the straight lines are parallel the *energy barrier* does

4. Pure and Zinc-Doped CoPhOMe

not vary, and it is $\Delta E = 160(\pm 8)$ K [83-84], in good agreement with the value found in previous measurements. The shift of the lines along y axis is due to the fact that the *pre-exponential factor* varies with increasing the doping concentration going from 3.5×10^{-11} s for pure CoPhOMe to 1.0×10^{-12} s for the highest doping concentration [83-84].

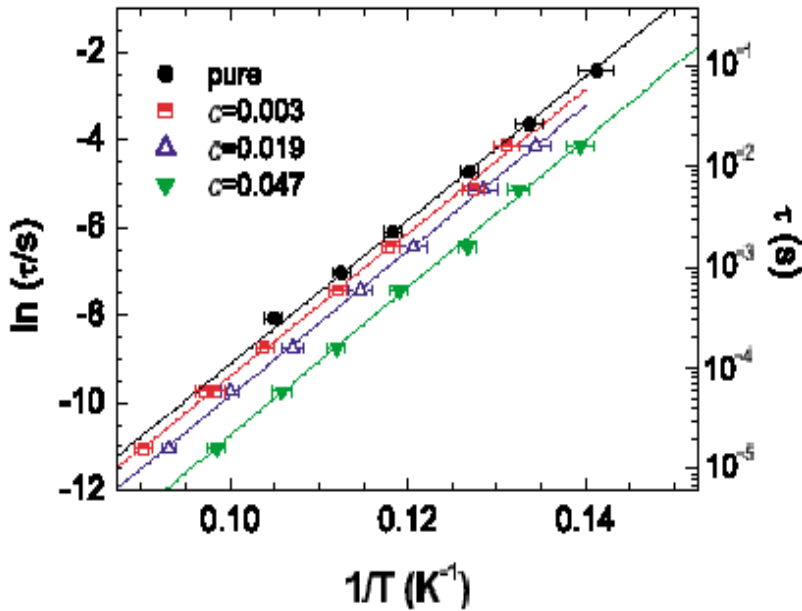


Fig.4.27 Temperature dependence of the relaxation time τ extracted from the imaginary part of the AC susceptibility for pure CoPhOMe and for three different concentrations of Zn-doped samples [83].

An important remark to be made is related to the slope of the curves: from a theoretical point of view the slope should be halved for doped samples, when ξ becomes larger than segments length L , while here the slope remains unaltered. We can conclude that also for pure compound the presence of unwanted *intrinsic defects* reduces the average chain length below the

4. Pure and Zinc-Doped CoPhOMe

correlation length value.

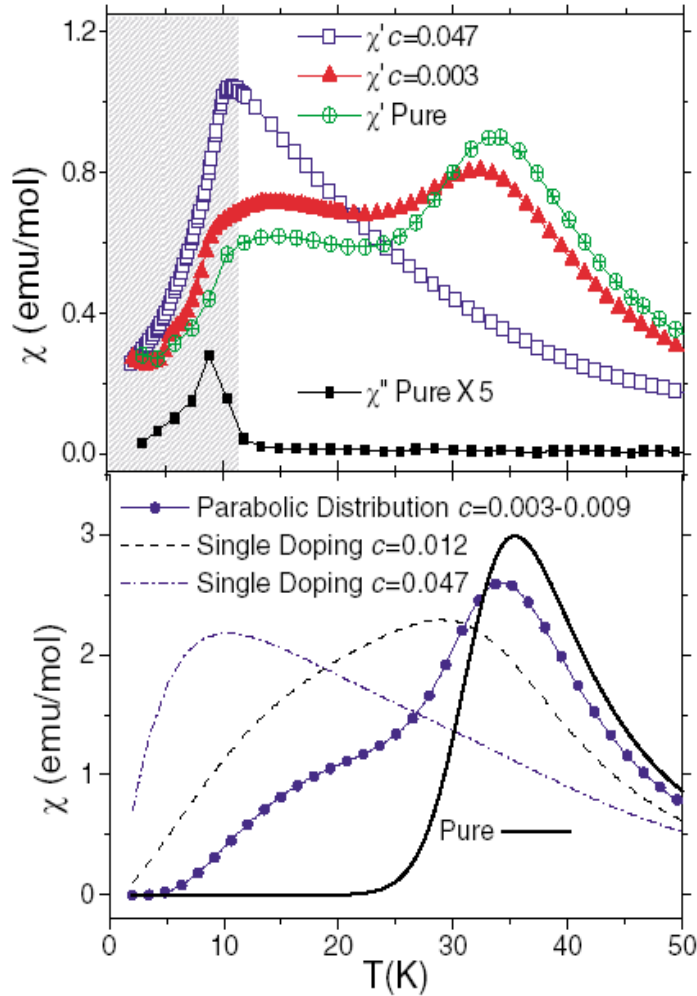


FIG.4.28 ABOVE: Longitudinal magnetic AC susceptibility as a function of temperature for different Zinc-doped CoPhOMe samples and for pure compound for a static magnetic field of 2kOe and for an AC field of 10Oe of frequency 2.4kHz; in the shaded region AC susceptibility is frequency dependent. **BELOW:** susceptibility calculated through transfer matrix calculations for pure and various doped CoPhOMe samples [83][84].

4. Pure and Zinc-Doped CoPhOMe

As regards the real component χ' of the AC susceptibility, this new run of measurements has shown important new features. For the first time the curves present two peaks, while previously just one peak had always been detected, resembling the behaviour detected by spin-lattice relaxation rate in NMR measurements on pure sample.

As can be seen from FIG. 4.28 (upper part) also for pure compound the curve shows a structure with a pronounced peak at $T \sim 33\text{K}$ and a shoulder for $T \sim 14\text{K}$. Both these temperatures are above the blocking temperature where also in this case χ'' becomes *frequency dependent* also for doped samples: this can be still ascribed to dynamic effects. Let's quickly analyse the behaviour of the peaks with respect to the diamagnetic concentration. The peak at higher temperature is the one expected for the *infinite chain*: this is suggested also by its decreasing with increasing the doping concentration. It also shifts to lower temperature while it decreases. Instead the peak at lower temperature seems to be related to *finite-size effects*: in fact it increases with increasing the impurity concentration and for $\text{Zn}=4.7\%$ the left shoulder becomes the only surviving peak. One of the most striking feature in the real part of AC susceptibility is the presence of the broad shoulder at low temperature also for the pure compound: this confirms that also in the pure compound the defects play a fundamental role and the chains behave just as long segments as previously predicted by the slope for pure CoPhOMe in FIG.4.27. From a theoretical point of view the structure detected in measurements is predicted by the sample Hamiltonian valid also for pure compound:

$$H = \sum_i J \left(\vec{S}_{2i}^{\xi} \cdot \vec{S}_{2i+1}^{\xi} + \vec{S}_{2i}^{\xi} \cdot \vec{S}_{2i-1}^{\xi} \right) - \mu_B H^{\xi} \sum_i \left(g_{Co} \vec{S}_{2i}^{\xi} + g_{rad} \vec{S}_{2i-1}^{\xi} \right). \quad (4.21)$$

4. Pure and Zinc-Doped CoPhOMe

Treating this Hamiltonian with transfer matrix method the conclusion is that for pure sample just the peak at $T \sim 34\text{K}$ is predicted while for doped samples a second peak arises at $T \sim 15\text{K}$: this theoretical analysis is in good agreement with experimental results obtained. Calculations for various concentrations are shown in FIG.4.28 (lower part): the further assumption for a closer correspondence between data and calculation consists in taking into account a parabolic spatial distribution for diamagnetic dopant as suggested by PIXE measurements [85] shown in FIG. 4.24.

NMR MEASUREMENTS

4.6.5 Introduction

In the previous paragraphs the main magnetic properties of the compounds have been investigated with the tools of magnetization and susceptibility (DC and AC) measurements: in this way the magnetic properties have been displayed by means of macroscopic quantities with the detection of the homogeneous response (i.e. the generalized response functions at $q=0$) of the system to external perturbations. Nuclear Magnetic Resonance (NMR), instead, makes use of a *local probe* represented by nuclei for the investigation of the magnetic properties, mediated by the *hyperfine interactions* between nuclei and electrons. Nuclear Spin Lattice Relaxation Rate (NSLR) parameter is a suitable probe of local spin dynamics, since it is related to the integral along all the branches of low-energy excitations at different wave vectors. NMR measurements have been performed on CoPhOMe samples doped with two different concentrations of Zinc diamagnetic ions ($\text{Zn}=1.9\%, 5.4\%$) on

4. Pure and Zinc-Doped CoPhOMe

Hydrogen nucleus (^1H , commonly called simply proton) for two different magnetic fields of 0.35Tesla and 1.65Tesla, corresponding to Larmor frequencies of about 14.9MHz and 70.2MHz respectively, in the temperature range 1.5-300K. These measurements consist in the detection of *absorption spectra* and in the determination of the *NSLR*.

4.6.6 ^1H NMR Spectra

We have collected spectra performing the Fourier Transform of half of the echo signal thus obtaining the absorption NMR spectrum.

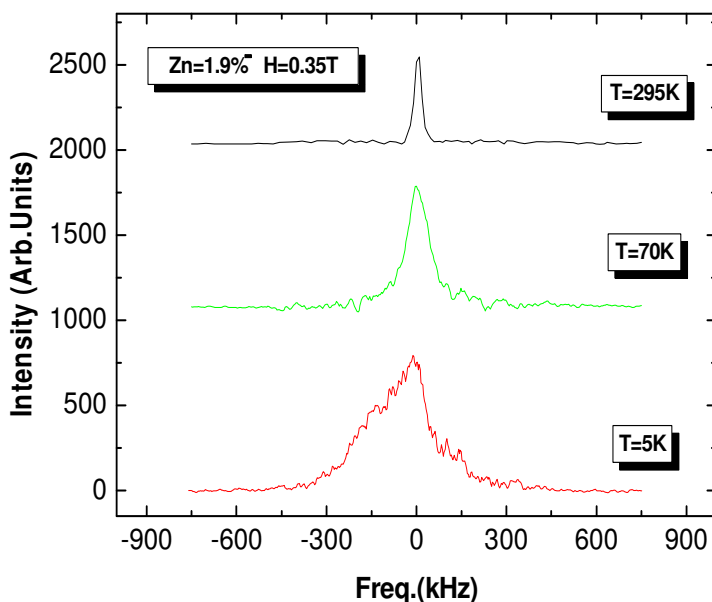


FIG.4.29 ^1H NMR absorption spectra of CoPhOMe doped with Zinc ions with a percentage of $\text{Zn}=1.9\%$ in an applied field of $H=0.35\text{T}$ for three different temperatures ($T=295\text{K}$; 70K ; 5K).

4. Pure and Zinc-Doped CoPhOMe

Results are displayed in FIGS.4.29-4.30. As can be clearly seen for all the samples investigated, the spectra become broader as the temperature is lowered. This line broadening is due mainly, as for the pure compound, to hyperfine interactions.

These interactions cause the nuclear spins to feel various local internal magnetic fields at nuclear sites with a total field which can be written in terms of the Larmor precession frequency for i -th nucleus

$$\vec{\omega}_L^i = \gamma_H (\vec{H}_0 + \vec{H}_{loc}^i) \quad (4.22)$$

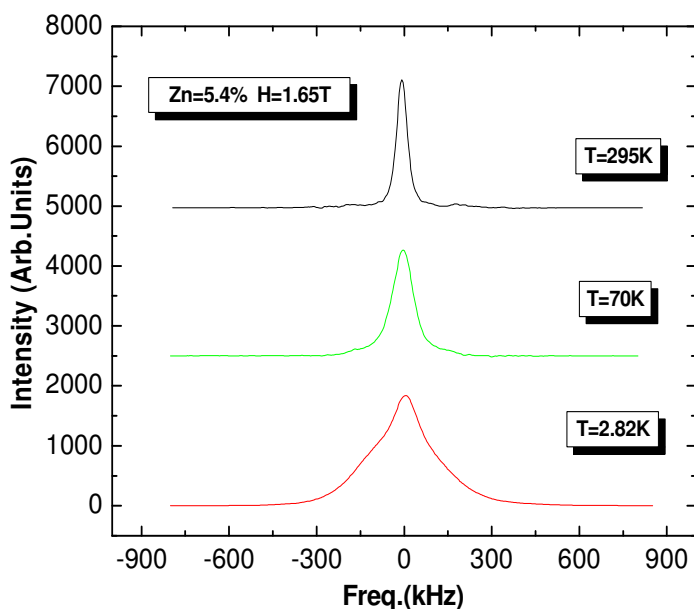


FIG.4.30 ^1H NMR absorption spectra of Zinc-doped CoPhOMe (Zn=5.4%) in an applied field of $H=1.65\text{T}$ for three different temperatures ($T=295\text{K}$; 70K ; 2.82K).

4. Pure and Zinc-Doped CoPhOMe

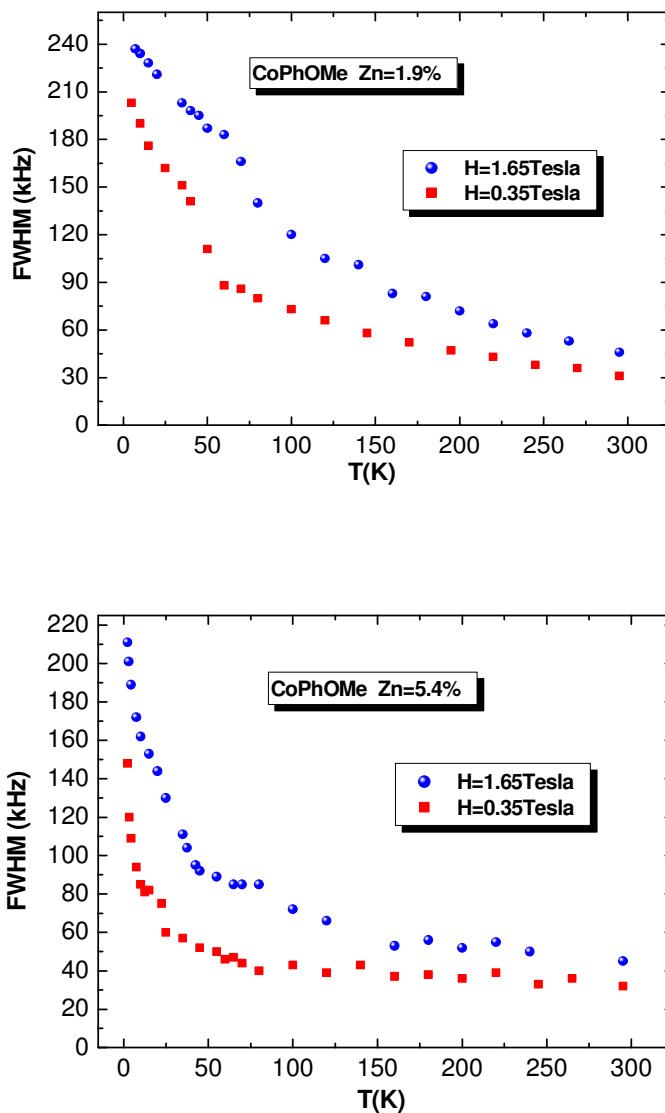


FIG.4.31 Full Width at Half Maximum (FWHM) as a function of temperature for CoPhOMe doped with Zn=1.9% (ABOVE) and Zn=5.4% (BELOW) for H=0.35T, 1.65T. The line broadening with decreasing temperature is evident.

4. Pure and Zinc-Doped CoPhOMe

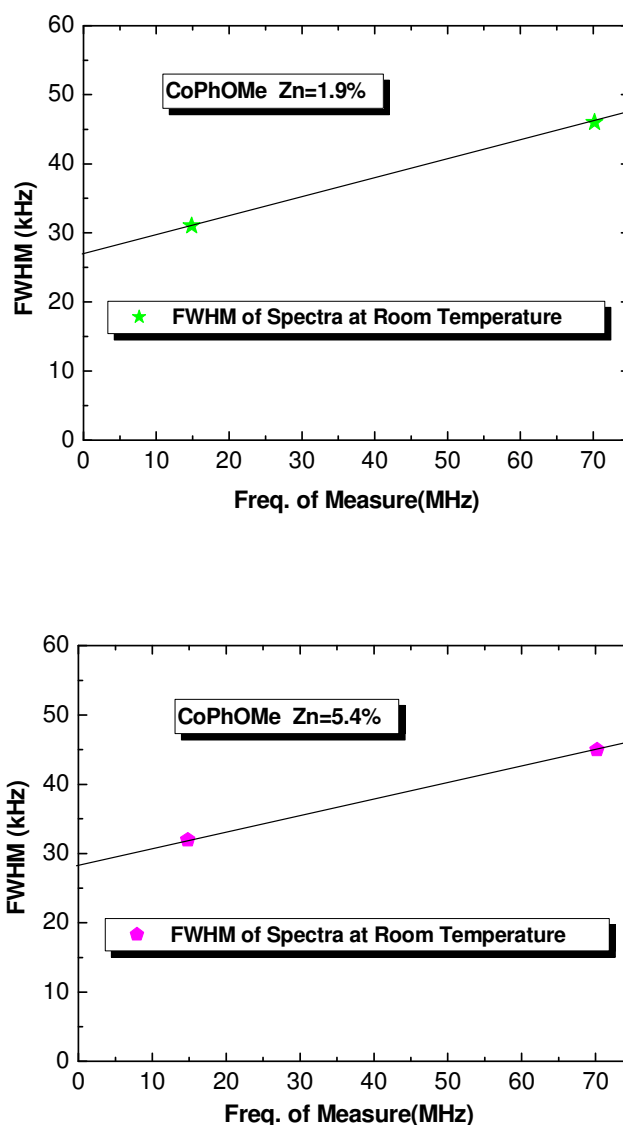


FIG.4.32 FWHM at Room Temperature for CoPhOMe doped with Zn=1.9% (ABOVE) and Zn=5.4% (BELOW) at the two magnetic fields used for measurements (the correspondent frequencies are reported on x-axis). The value extracted at $H=0$ Tesla from the straight line connecting the data collected gives us a rough estimation of the nuclear dipolar contribution to the line-width.

4. Pure and Zinc-Doped CoPhOMe

In FIG.4.31 the Full Width at Half Maximum (FWHM) of the spectra is plotted as a function of temperature.

The *broadening* observed in FIG.4.31 on lowering the temperature is *inhomogeneous* i.e. is due to a *distribution of local fields* due to the presence in the chain of many non equivalent proton sites [56].

Since the local field is proportional to the average local moment of the magnetic ions, this contribution is proportional to the susceptibility and thus it increases on lowering the temperature. It is also proportional to the applied magnetic field as shown in FIG.4.32.

The zero field intercept represents the contribution to the line width arising from *nuclear dipole-dipole interaction* which is temperature and field independent.

The *dipolar contribution* to the spectral width is estimated to be around 25kHz.

This value is of the same order of magnitude as the one obtained before for pure CoPhOMe and for all *molecular nanomagnets* [2-7] as expected, since the nuclear dipolar line width depends on the proton distribution in the organic groups which are similar in all molecular magnets.

The inhomogeneous part of the NMR line width is given approximately by the measured FWHM to which we subtract the nuclear dipolar contribution . This contribution to the width is proportional to the *local magnetic moment* which in turn is given by χ_{loc} B. Thus the inhomogeneous contribution to the NMR line-width divided by the field B is a microscopic measurement of the local susceptibility χ_{loc} .

In FIG.4.33 we have plotted for both the samples investigated in this section and for both the field applied in the measurements the difference between the FWHM and the FWHM due to the

4. Pure and Zinc-Doped CoPhOMe

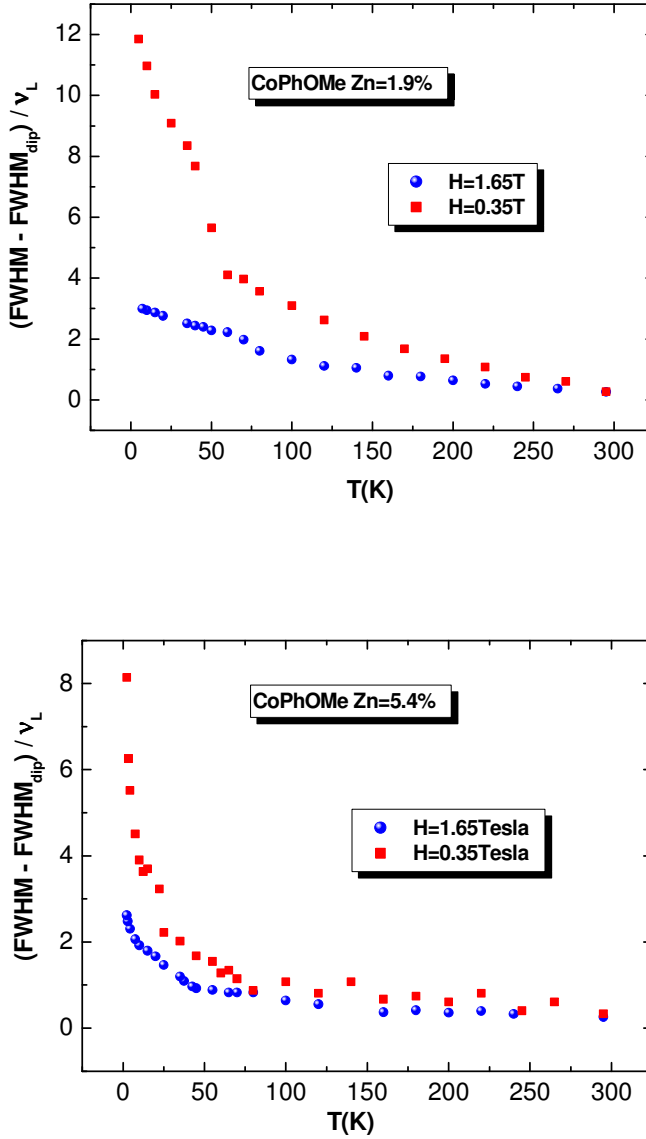


FIG.4.33 $(FWHM-FWHM_{dip})/v_L$ as a function of temperature for CoPhOMe doped with Zn=1.9% (ABOVE) and Zn=5.4% (BELOW) for both the applied fields ($H=0.35, 1.65T$). From these data we can obtain the behaviour of χ_{loc} for the samples investigated.

4. Pure and Zinc-Doped CoPhOMe

dipolar contribution estimated before at room temperature in Zero-Field applied divided by the Larmor frequency. This quantity is proportional to *local susceptibility* of the sample, as just said: as can be seen from FIG.4.33 (lower part) the experimental local susceptibility is coincident for the two fields applied only around the room temperature while for the sample with higher doping (FIG.4.33 upper part), within the experimental error, the two local susceptibilities are coincident only above 75K. It is noted that for a simple paramagnetic system the susceptibility (both local and macroscopic) should be field independent at temperatures where the slowing down of the magnetization is not yet active. This is a very striking result and it indicates a departure from simple paramagnetic behaviour. The theoretical analysis of this result has not been yet completed.

4.6.7 Spin-Lattice Relaxation Rate T_1^{-1}

Typical *nuclear magnetization recovery curves* for the Zinc-doped samples investigated are shown in FIG.4.34. The plots show the nuclear longitudinal magnetization recovery plotted in the form $\frac{M(\infty)-M(t)}{M(\infty)}$ where $M(\infty)=M(t \rightarrow \infty)$ is the value of the longitudinal magnetization when it has recovered completely its position along the z -axis.

As for the case of pure CoPhOMe, the recovery curves are strongly non-exponential.

For doped samples the relaxation time has been read at $1/e$ of the decay of the nuclear magnetization. The results for samples with Zn=1.9%, 5.4% for magnetic fields of $H=0.35, 1.65$ Tesla are shown in FIGG. 4.35-4.36.

Before analysing the experimental data, we recall briefly the

4. Pure and Zinc-Doped CoPhOMe

derivation of the theoretical formula for the NSLR used for the interpretation of the data.

Let's start from the general expression [90]:

$$\frac{1}{T_1} = \frac{\gamma^2}{2} \int \langle h^\pm(t) h^\pm(0) \rangle \exp(-i\omega_L t) dt \quad (4.23)$$

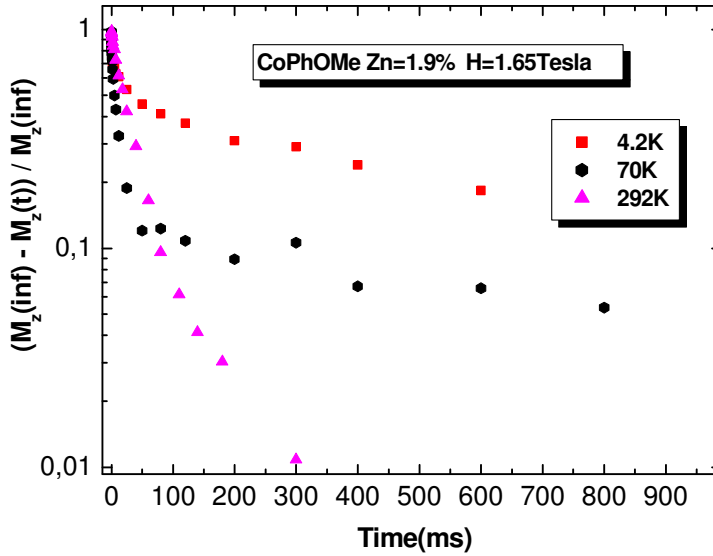


FIG.4.34 Relaxation curves of nuclear longitudinal magnetization performed on ^1H for three different temperature on Zinc-doped CoPhOMe with Zn=1.9% and H=1.65T. The deviation from the exponential behaviour is evident.

where, as already discussed in Chapter 2, γ is the *gyromagnetic ratio*, $h^\pm(0,t)$ are the *transverse hyperfine fields* at the nuclear sites and ω_L is the *Larmor frequency*.

Rewriting the expression in the wave-vectors space and for different wave-vectors \vec{q} it results:

4. Pure and Zinc-Doped CoPhOMe

$$\frac{1}{T_1} = C(T) \left[\sum_q \alpha_q \chi^+(\vec{q}) J_q^+(\omega_e) + \beta_q \chi^z(\vec{q}) J_q^z(\omega_L) \right] \quad (4.24)$$

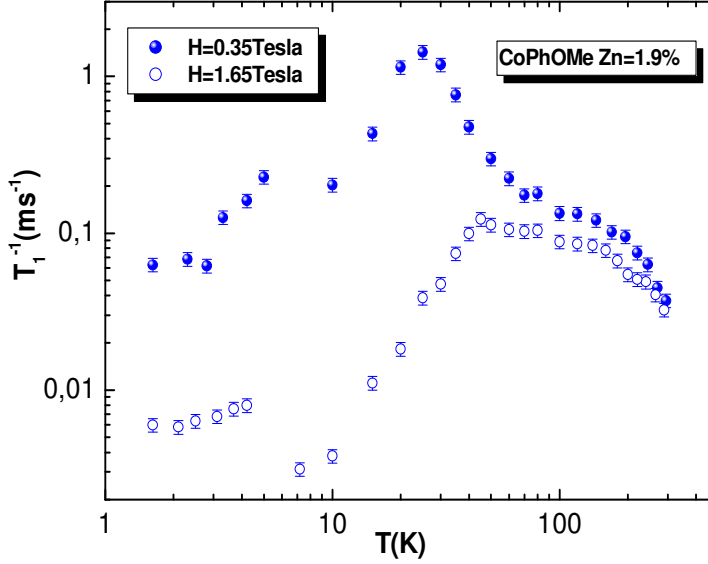


FIG.4.35 Temperature dependence of nuclear spin-lattice relaxation rate for CoPhOMe doped with Zn=1.9% for static magnetic fields applied of H=0.35, 1.65 Tesla.

with $C(T) = \frac{\gamma^2 h^2}{4\pi} \frac{k_B T}{g^2 \mu_B^2}$. In (4.11) $\chi^{+,z}(\vec{q})$ and $J_{\vec{q}}^{+,z}(\omega_L, \omega_e)$ are

the transverse and longitudinal components of *ω -integrated generalized susceptibility* and of the *collective spectral density* respectively with ω_e the electronic Larmor frequency.

Approximating $\chi(\vec{q}, \omega)$ with $\chi(\vec{q}, 0)$, neglecting $\alpha_q \chi^+(\vec{q}) J_q^+(\omega_e)$ (which has a low value) and assuming a correlation function decaying exponentially through the expression

4. Pure and Zinc-Doped CoPhOMe

$$g(t) = g(0) \exp(-t/\tau) \quad (4.25)$$

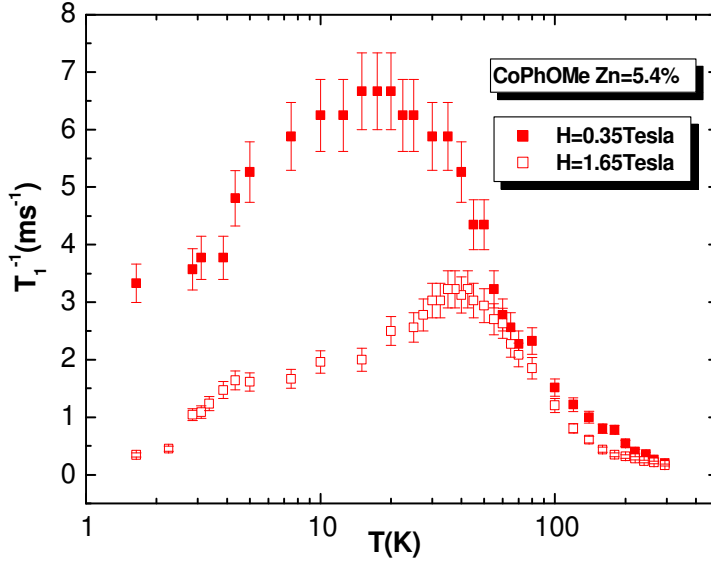


FIG.4.36 Inverse of spin-lattice relaxation time as a function of temperature for Zinc-doped CoPhOMe with Zn=5.4% for H=0.35, 1.65Tesla.

one can obtain, through the application of the time *Fourier Transform*, the simplified equation

$$\frac{1}{T_1} = A^2 \frac{2\tau}{1 + \omega_L^2 \tau^2} \quad (4.26)$$

where A^2 is the mean square value of fluctuations of the hyperfine field at nuclear sites.

The equation for the relaxation time τ has the expression of the Arrhenius law, as predicted by Glauber dynamics [1] for 1D

4. Pure and Zinc-Doped CoPhOMe

Ising systems. Also in this case nuclei have been assumed to be sensitive to electronic spin dynamics through the magnetization. As mentioned before, the previous results obtained from macroscopic measurements on doped samples suggested that the behaviour of the short segments is the same as in the pure compound, i.e. the thermally activated mechanism for the relaxation of the magnetization does not change the energy barrier and it is still Arrhenius-like

$$\tau = \tau_0 \exp\left(\frac{\Delta}{T}\right) \quad (4.27)$$

with the pre-exponential factor becoming shorter by about one order of magnitude with respect to the one in the pure compound [83-84][86], as discussed before.

Since both the NSLR results in pure CoPhOMe and in the Zn doped samples show the same qualitative behaviour as a function of temperature, we use the same fitting procedure used for pure CoPhOMe except for the introduction of a distribution of activation energies also for the fit of the high temperature peak which appears broader than in pure CoPhOMe (see FIGS. 4.37-4.38)

The fitting function can be thus written

$$\frac{1}{T_1} = \sum_{i=1,2} (A_i \gamma_i)^2 \left\{ (1/2 \omega_L \ln b_i) [\arctg(b_i \omega_L \tau_i) - \arctg(\omega_L \tau_i / b_i)] \right\} \quad (4.28)$$

with $b_i = \exp(\delta_i/T)$, $\tau_i = \tau_{0i} \exp(\Delta_i/T)$ and $(A_i \gamma_i)$ is the hyperfine coupling constant.

Results of the fits are shown in FIGS. 4.37-4.38 for both samples. As can be clearly noticed the fits are acceptable only for the sample doped with lower concentration. The fitting parameters

4. Pure and Zinc-Doped CoPhOMe

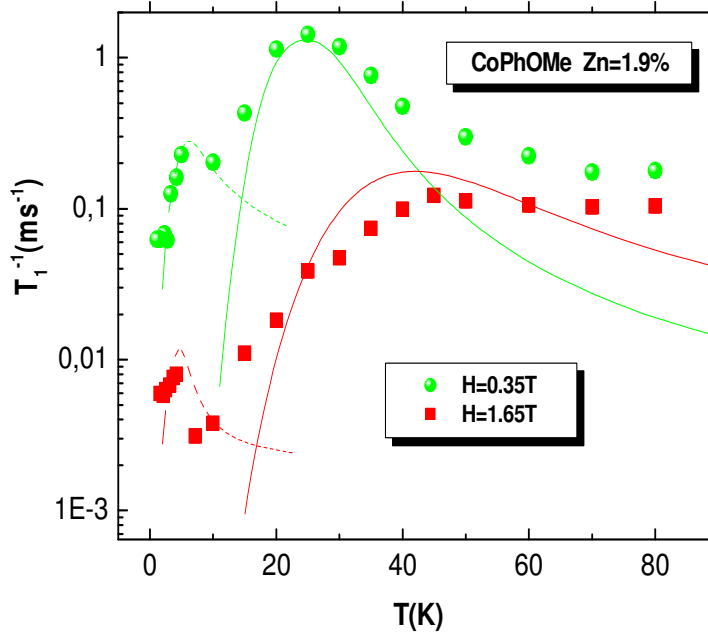


FIG.4.37 Temperature dependence of spin-lattice relaxation rate for CoPhOMe doped with Zn=1.9% for $H=0.35$; 1.65T . The dashed and solid lines represent the function fitting separately the two anomalies detected as explained in the text.

obtained are displayed in Table 4.1: in order to reduce the number of fitting parameters we used for the energy barriers the ones obtained in susceptibility measurements on pure sample. In order to get a reasonable fit we have to assume a magnetic field dependent pre-factor τ_0 . The physical meaning of this unexpected result is not yet presently understood.

In the light of the comparison of the NSLR results in pure CoPhOMe and Zn doped samples we argue that the origin of the two peaks may be different from what postulated above for pure CoPhOMe, namely as due to different relaxation mechanisms

4. Pure and Zinc-Doped CoPhOMe

related to the two sublattices. In fact while the higher temperature peak could be due to “*bulk*” *contribution* with thermally activated mechanism as pointed out in AC susceptibility, the lower temperature shoulder could be related to *finite-size effects* which become more and more important as the concentration of dopant becomes higher.

Parameters→ Samples ↓	Δ_1	δ_1	Δ_2	δ_2	ω
Zn=1.9%H=0.35T	150K	35K	17K	10K	14.87MHz
Zn=1.9%H=1.65T	150K	35K	17K	10K	70.14MHz
Zn=5.4%H=0.35T	150K	65K	10K	4K	14.87MHz
Zn=5.4%H=1.65T	150K	65K	10K	4K	70.15MHz

Table 4.1 Principal parameters as indicated in eq.(4.28) used in NMR fits for both the samples and both the applied fields in measurements.

In very short segments and low temperature *collective spin reversal* of all the spin of a segments can also take place [84]: the *Cole–Cole plot*, which is no longer a semicircle [83], accounts for this mechanism.

Let’s explain how this new channel for relaxation is detected also in dynamic susceptibility.

For a segment of N spins the relaxation time can be written [87]

4. Pure and Zinc-Doped CoPhOMe

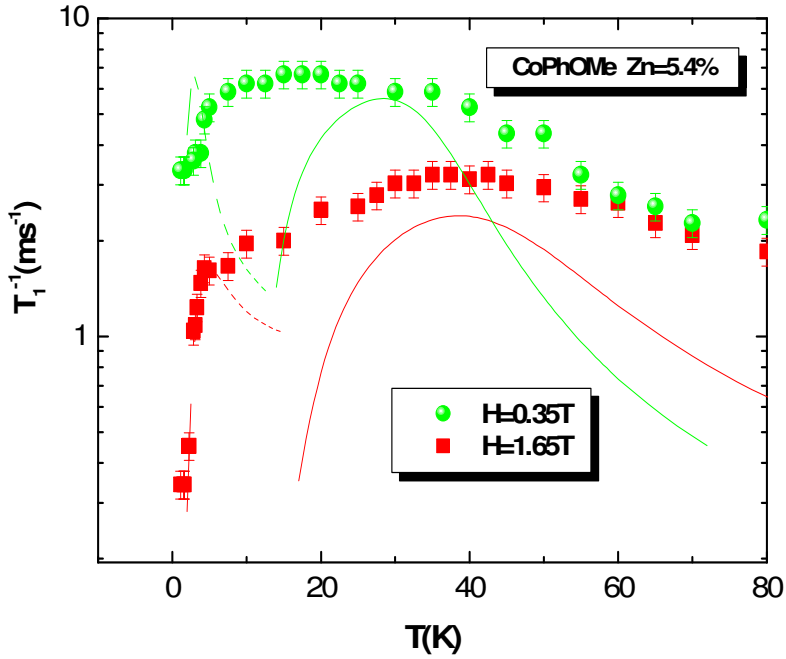


FIG.4.38 Spin-lattice relaxation rate as a function of temperature for CoPhOMe with Zn=5.4% for $H=0.35$; 1.65Tesla , the dashed and solid lines are the best fit as explained in the text.

$$\frac{1}{\tau_N} = \frac{1}{\Delta t} \left[\frac{2q}{N-1} \exp\left(\frac{2J}{k_B T}\right) + q^N \right] \quad (4.29)$$

where q is the probability of a single spin reversal in the time interval Δt , $1/N-1$ is the probability for a domain wall to propagate from side to side of a segment without being destroyed. If collective reversal of the segments is not taken into account, the dynamic susceptibility should drop to zero below the blocking temperature since the spins are not able to follow the oscillating field, i.e. when $\omega\tau_N > 1$, and the segments that can

4. Pure and Zinc-Doped CoPhOMe

follow this field are the ones shorter than \hat{N} , which can be extracted from the equation [87]

$$\omega\Delta t = q^{\hat{N}} \quad (4.30)$$

The inclusion of the collective reversal of the magnetization leads to a frequency cut-off in the equation

$$\chi(\omega, T) = \frac{c^2}{Z_c} \sum_{N=1}^{\infty} \frac{\chi_N(\omega, T)}{1 - i\omega\tau_N} (1 - c)^N \quad (4.31)$$

similar to eq.(4.19) where, in this case, the length L of the segment has been substituted by the number N of spins of the segments.

It was found that $\chi'T$ vs T plots have a polynomial behaviour below T_b as predicted for a q obeying the thermally activated law [87]

$$q = \exp\left(-\frac{\varepsilon}{T}\right) \quad (4.32)$$

where ε is the energy barrier. The comparison between experimental and theoretically calculated data [87] suggests that for CoPhOMe ε/J results to be of the order of 0.05.

The frequency cut-off is given by

$$\hat{N} = -\log(\omega\Delta t) \frac{k_B T}{\varepsilon} \quad (4.33)$$

in fact all the curves obtained at various frequencies can be superimposed if plotted as a function of $-\log(\omega\Delta t)T$ (see FIG. 4.39).

4. Pure and Zinc-Doped CoPhOMe

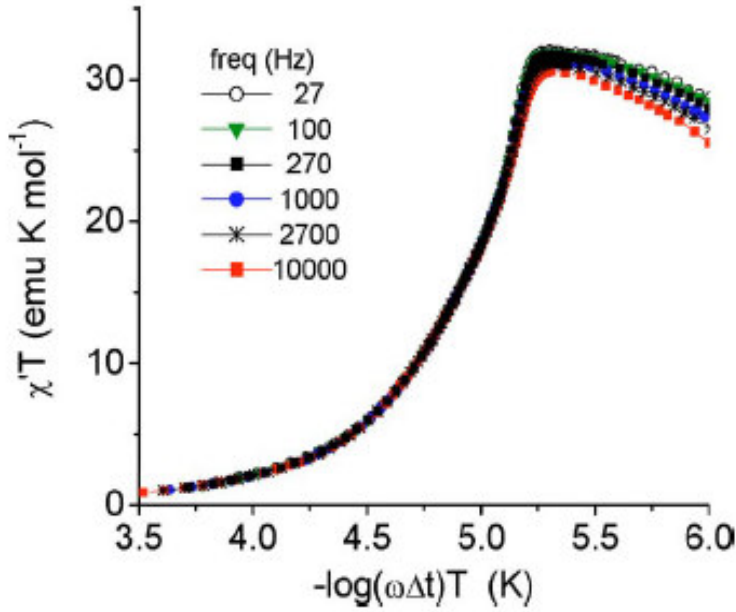


FIG.4.39 χ' data extracted from AC susceptibility and plotted as a $\chi'T$ as a function of scaling variable $-\log(\omega\Delta t)T$ for CoPhOMe doped with Zn=4.7% with $\Delta t=5.1\text{ps}$: all the curves overlap as expected for a thermally activated behaviour of q at low temperature for high doped samples taking into account collective reversal of all the spins of the segment [87].

In the light of the discovery of this new channel for relaxation at low temperature, also the NSLR data collected for $T < 15\text{K}$ for the samples investigated must be reinterpreted as due to collective spin reversal. In fact in the analysis done previously to justify the low-temperature shoulder in spin-lattice relaxation rates, we have used a distribution of energy barriers, possibly related to the excitation at different wave vectors in the generalized susceptibility, but with values of ΔE of few Kelvin (see Table 4.1). These energy barriers values used for fits in NSLR are in good agreement with the evaluation of the ratio ϵ/J just discussed

4. Pure and Zinc-Doped CoPhOMe

above and extracted from the susceptibility measurements and calculations [87]. This coincidence suggests that the thermally activated mechanism detected for $T < 15\text{K}$ in T_1^{-1} measurements should be attributed to the Arrhenius-like behaviour in the framework of the *collective spin reversal* instead of the slowing down of the magnetization within a modified *BPP law*. This hypothesis is still a debated issue; in fact we have to prove how finite-size effects and this new relaxation mechanism acts from a microscopic point of view and how they are related to the behaviour of spin-lattice relaxation rate.

4.7 Conclusions

In order to investigate the effect of finite-size on the spin dynamics of ferrimagnetic **Zn-doped CoPhOMe** samples, a comparison has been made among the behaviour of the pure and doped samples performing new measurements of magnetic properties also for pure compound. While *DC measurements* show for doped samples the same behaviour already discussed in the first part of this chapter for pure CoPhOMe, the real part of the *AC susceptibility* [83-84][86] measurements displays novel features also for pure CoPhOMe consisting in a structure in the temperature dependence of χ' . The structures consist of a peak at $T \approx 33\text{K}$ which shifts at higher temperature with increasing field, smoothens for higher doping and disappear for $\text{Zn} = 4.7\%$, and a broad shoulder at $T \approx 14\text{K}$ which remains the only anomaly for higher doped samples. The first anomaly is the one expected for infinite chains and diminishes when the segments become really short (~ 20 spins of length for $\text{Zn} = 4.7\%$), while the low temperature shoulder can be related to finite-size effects, as confirmed by theoretical transfer matrix calculations starting from eq.(4.21). Also the relaxation time extracted from the

4. Pure and Zinc-Doped CoPhOMe

imaginary part χ'' of the AC susceptibility, confirmed that *finite-size effects* are present also in pure compound: all the compounds displayed the thermally activated relaxation time through the *Arrhenius-like behaviour* with different *pre-exponential factors* that diminish progressively for higher doping, but with the same energy barrier, differently from what expected from a theoretical point of view. In fact for an infinite system, as in the case of pure compound, the progressive reversal of the chain starts from a “bulk” spin inside the chain with an activation energy of $\Delta=4J$ and the other reversal occurs with no energy cost; instead, for segments of chain, the reversal starts from an edge spin and $\Delta=2J$. That’s why the energy barrier should be halved in doped samples. The conclusion is that also in the pure sample the occurrence of natural defects makes impossible the treatment of the system as infinite.

Our *microscopic measurements* performed through the local probe of proton nuclei with NMR have given some new unexpected results which have not yet been fully understood. The study of 1H NMR spectra showed that for the two doped samples investigated a line broadening occurs with decreasing temperature and this is associated with a distribution of local fields at the proton sites due to the local magnetic moments of the Cobalt ions and of radical centres. The *local susceptibility* extracted from the NMR line-width displays a field dependence over most of the temperature range. A field dependence of the local susceptibility is expected only in the range of temperature where the spin freezing takes place and the local field becomes weakly field dependent. This discrepancy between the behaviours of the local NMR susceptibility and the macroscopic susceptibility could have implications on the description of the spin dynamics but it is not presently understood.

The behaviour of the *spin-lattice relaxation rate* for the two

4. Pure and Zinc-Doped CoPhOMe

doped samples is qualitatively similar to the one of the pure CoPhOMe with the only difference that the high temperature peak is broader in the doped samples.

An attempt to fit the NSLR data in doped compounds by using the same formulas used for the pure CoPhOMe showed a poor agreement with the experimental data, even when a distribution of activation energies was introduced for the high temperature peak.

The interpretation of the shoulder in the real part of the AC susceptibility as due to finite size-effects, led us to reformulate the interpretation of the NMR data of pure CoPhOMe. In fact we should assume that the peak at higher temperature is due mainly to *bulk contribution* characterized by Arrhenius thermally activated behaviour, while the shoulder in NSLR could signal the presence of *finite-size effects* at low temperature.

In particular for high percentage of dopant ($\text{Zn} > 4\%$) at low temperature, below the *blocking temperature* $T_b \approx 12\text{K}$, the most important finite-size effect is related to the *collective reversal of all the spins* of the segment [84] with a probability which has been found to be thermally activated too.

In conclusion the open questions related to the NMR measurements consist in the interpretation of the mechanisms causing the anomalous line broadening in ^1H absorption spectra especially for $T > 60\text{K}$ and of the two anomalies detected in NSLR, which don't seem to be necessarily related to the relaxation times of the two different sublattices of the compounds, but eventually also to finite-size effects.

CHAPTER 5

Gd(hfac)₃NITR Chains

5.1 Gd(hfac)₃NITR

5.1.1 Introduction

In this chapter the 1D molecular magnetic chain Gd(hfac)₃NITR composed by a mixing of organic and inorganic components will be described. The change of physical properties, when different organic radicals moieties are inserted in these systems, have made possible the creation of systems with novel and unexpected features, which are still subject of theoretical debate. The properties of these compounds will be discussed and a theoretical explanation for the interpretation of the experimental data will be proposed. In the framework of the current thesis, where one-dimensional and quasi-one-dimensional real systems composed by similar building blocks are investigated, this family of compounds can be put in the class of *helimagnetic frustrated systems* due to competing interactions occurring along the chain direction.

The discussion of general features will be based mainly on results obtained by experimentalists and theorists of the University of Firenze (Dept. of Physics, Dept. of Chemistry), of CNR and of the University of Modena (Dept. of Physics).

5.1.2 Structural and Magnetic Properties

The structural properties of the compounds presented in this chapter, have been studied by X-ray diffractometry performed on single crystals.

5. Gd(hfac)₃NITR Chains

As anticipated, the chemical formula of the investigated molecular-based magnets is Gd(hfac)₃NITR (where hfac is hexafluoro-acetylacetonate and NITR is 2-R-4,4,5,5-tetramethyl-4,5-dihydro-1H-imidazolyl-1-oxyl 3-oxyde, with R= Isopropyl (iPr), Ethyl (Et), Phenyl (Ph), Methyl (Me)). The chain develops along *b* crystallographic axis and it is constituted by Gd³⁺(hfac)₃ moieties, alternated to *nitronyl-nitroxide organic radicals R*. Gd³⁺ possesses a spin $S=7/2$, while for radical centres $s=1/2$ [17][91-92]. At variance with CoPhOMe chains, here the radical groups are alternated to a *rare-earth* instead of a metal *ion*.

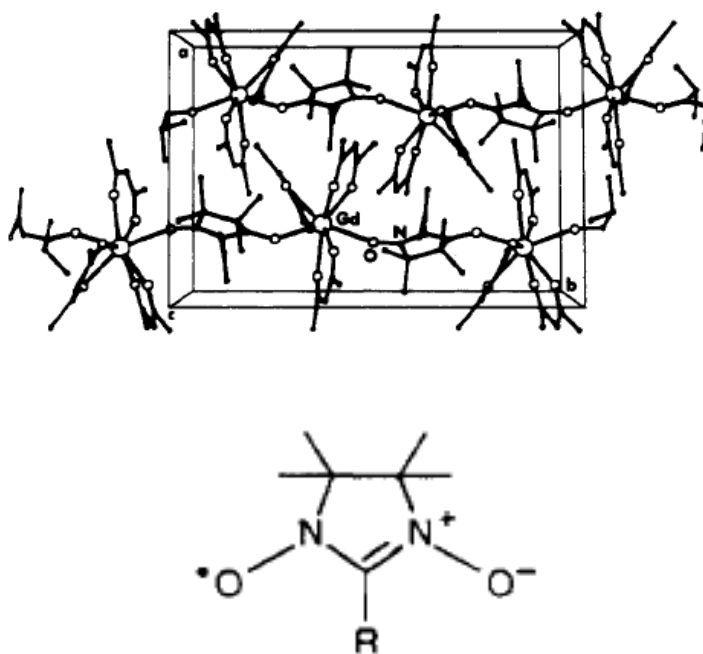


FIG.5.1 ABOVE: General sketch of the structure of Gd-R chains.
BELOW: Structure of the Radical Group NITR.

As in the case of pure and doped CoPhOMe the bulky ligands

5. $\text{Gd}(\text{hfac})_3\text{NITR}$ Chains

play a crucial role as they assure the adjacent chains to be well-separated, saving the 1D behaviour of the system till very low temperatures. In fact, as the shortest interchain distance between Gadolinium ions is of about 10.5\AA , just very weak dipolar interactions are present between chains. As suggested from measurements performed on Mn analogues, the $J_{\text{inter}}/J_{\text{intra}}$ ratio is lower than 10^{-5} [91].

A clear evidence of the 1D character of these compounds comes from single-crystal EPR measurements [17]: the angular dependence of the line width of EPR spectra at room temperature shows a maximum along b axis and a minimum at 50° from that direction, close to the value of the so-called magic angle (54.7°), as predicted for a 1D magnetic systems in the high-temperature limit.

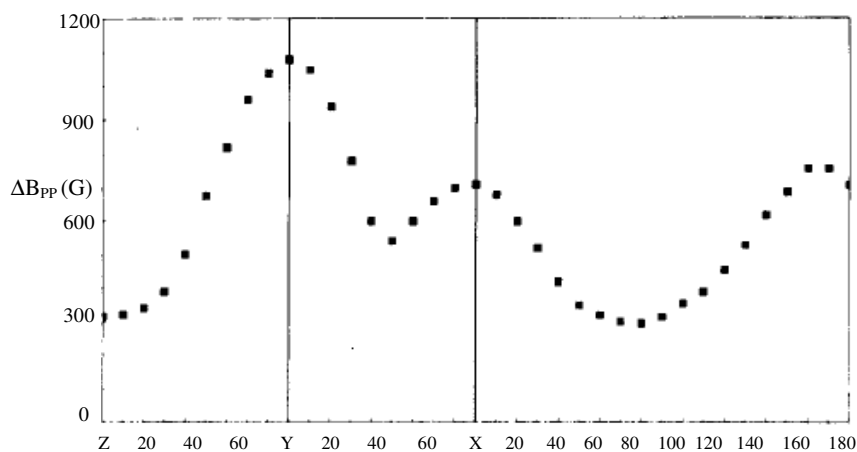


FIG.5.2 Angular dependence of the line-width of the X-band EPR spectrum at room temperature on $\text{Gd}(\text{hfac})_3\text{NITet}$ [17].

The main problem to be faced for the interpretation of the physical properties of these compounds has been related to the

5. Gd(hfac)₃NITR Chains

understanding of inter- and intrachain interactions acting in the system.

First magnetic measurements showed that the *molar susceptibility* multiplied for temperature in Gd-Et and Gd-iPr decreased with decreasing temperature, suggesting an overall *antiferromagnetic behaviour*.

In fact this feature corresponds neither to a system of uncoupled spins, where $\chi_M T$ would be constant with temperature, nor to a chain with ferromagnetic or antiferromagnetic interactions, since in both the cases $\chi_M T$ would diverge at low temperature.

A second run of χ measurements [93] (applied field of 1kG) for all the compounds described in this work confirmed the early results (see FIG. 5.3).

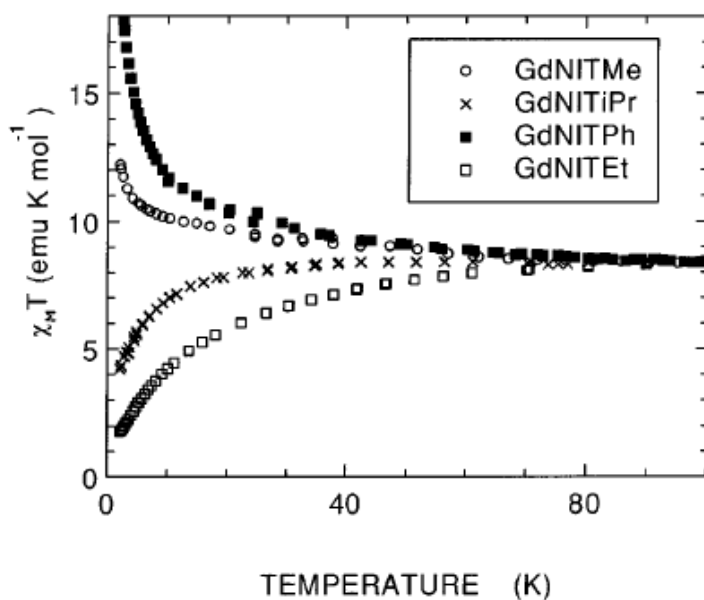


FIG.5.3 Plot of molar susceptibility multiplied by temperature as a function of temperature for the four Gd-R compounds [93].

5. $\text{Gd}(\text{hfac})_3\text{NITR}$ Chains

As can be clearly seen, the four compounds behave in two different ways; in fact while for Methyl and Phenyl derivatives $\chi_{\text{M}}T$ increases and diverges with decreasing temperature, while for Gd-Et and Gd-iPr decreases at low temperature.

The experimental evidences led to the conclusion that no model, taking into account just nearest-neighbour interactions, could explain the behaviour displayed by these systems. This anomalous behaviour can be justified only taking into account also next nearest-neighbour interactions. The model suggested

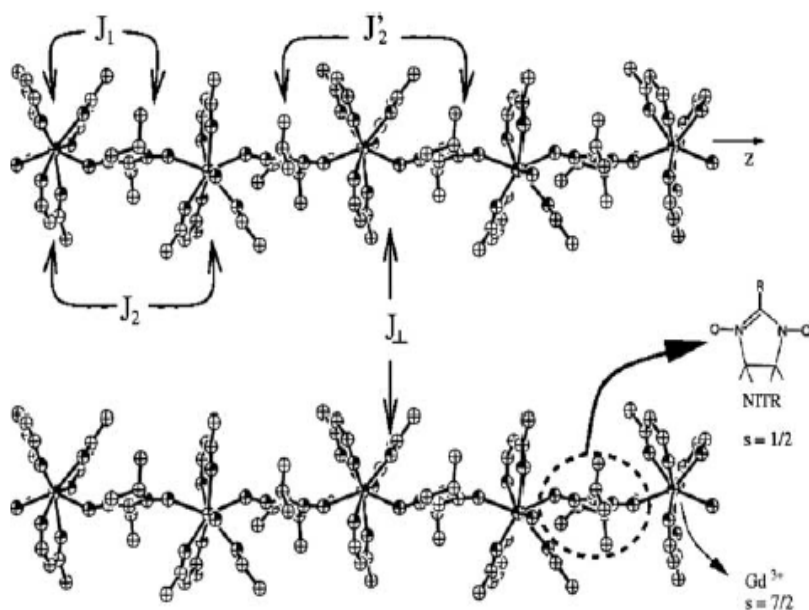


FIG.5.4 Pictorial view of the Gd-R chains where various exchange coupling constants are indicated as described in the text [94].

(next section) [95] introduces a *competition* between nearest-neighbour and next-nearest-neighbour interactions. In particular in the case of Isopropyl and Ethyl compounds the overall antiferromagnetic behaviour is due to dominant *nnn*

5. Gd(hfac)₃NITR Chains

antiferromagnetic exchange interactions in competition with *nn* ferromagnetic ones, leading to a strong frustration in the system; for the samples with R=Me, Ph the frustration is much weaker as suggested by the increase of $\chi_M T$ with decreasing temperature.

5.1.3 Hamiltonian and Model of Interpretation

The qualitative explanation given above can be expressed in the Hamiltonian of interaction which results to be, as already discussed in Chapter3,

$$H = H_{intra} + H_{inter} \quad (5.1)$$

where [57-58][95]

$$H_{i,intra} = \sum_{i=1}^M \sum_{n=1}^{N/2} \left\{ -J_1 (\vec{S}_{i,2n-1} \cdot \vec{S}_{i,2n} + \vec{S}_{i,2n} \cdot \vec{S}_{i,2n+1}) - J_2 (\vec{S}_{i,2n-1} \cdot \vec{S}_{i,2n+1}) + \right. \\ \left. - J'_2 (\vec{S}_{i,2n} \cdot \vec{S}_{i,2n+2}) - g\mu_B \vec{H} \cdot \vec{S}_{i,2n-1} - g'\mu_B \vec{H} \cdot \vec{S}_{i,2n} + D(S_{i,2n-1}^z)^2 \right\} \quad (5.2)$$

and

$$H_{inter} = \sum_{\langle i,j \rangle} \sum_{n=1}^N \left[-J_{\perp} (\vec{X}_{i,n} \cdot \vec{X}_{j,n}) \right] \quad (5.3)$$

where $J_1 > 0$ is the nearest-neighbour exchange coupling constant, $J_2 < 0$ and $J'_2 < 0$ are next-nearest-neighbour constants between metals and between radicals respectively and J_{\perp} represents the interchain exchange interaction, g and g' are Landé factors of the

5. Gd(hfac)₃NITR Chains

spins S and s respectively, $D>0$ is a single-ion anisotropy constant term and $\vec{X}_{j,n} = \vec{S}_{j,n}, \vec{s}_{j,n}$ (see also par.3.4).

To obtain the thermodynamic properties, transfer matrix calculations [56] have been performed starting from this Hamiltonian, approximating the spins with classical planar rotators in the x - y plane.

Harada [25][26][27] predicted that the competing interactions can favour a helical ground state two-fold degenerate (because of clockwise or counterclockwise turns of the spin along the chain axis) giving rise to excitations of the chiral domain walls separating two domains characterized by opposite chirality. In this thesis we will shortly present just the zero field case, since when a magnetic field is applied, the spin arrangement becomes very complicated [96].

From the previous theoretical discussion in Chapter 3 results that for $T=0$ and $H=0$, the system shows two different behaviours, depending on the relative strength of the nn and nnn interactions: in fact for $2(\delta+\delta')<1$ the system orders as a ferromagnet, while for $2(\delta+\delta')>1$ it undergoes a helical order.

The above parameters δ and δ' are defined as (see also Chapter 3 Par.3.4)

$$\delta = \frac{|J_2|S^2}{J_1Ss}, \quad \delta' = \frac{|J'_2|s^2}{J_1Ss}, \quad (5.4)$$

where the ratio between intrachain interactions are taken into account. The conditions written above suggest that if next-nearest- neighbour exchange interactions are strong enough, the helical ground state is favoured.

A discriminant parameter is the helix pitch Q defined as:

5. Gd(hfac)₃NiTR Chains

$$\pm Qa = \pm \cos^{-1} \left[\frac{1}{2(\delta + \delta')} \right] \quad (5.5)$$

where a is the lattice step and the sign $+$ or $-$ are respectively related to the clockwise or anticlockwise turn of the spins of the chain. In this framework, a *chirality order parameter* can be defined, related to a nn spin pair, whose expression is [26][29][68]:

$$K_{2n} = \frac{s_{2n} \times S_{2n+1}}{[\sin(Qa)]} \quad (5.6)$$

Depending on the model used for the interpretation of the data, this parameter has different features: for the Heisenberg model it is a three dimensional vector [27], while for the planar model (used in this case) it becomes a parameter with just one component whose value is ± 1 for clockwise or anticlockwise direction of the spins respectively, at $T=0$ [26]. The use of the planar model has been suggested by the fact that at low temperatures, the dipolar intrachain interactions are active (and no more negligible) causing the spins to lie in the x - y plane, as taken into account in the Hamiltonian in eq.(5.2) by the term

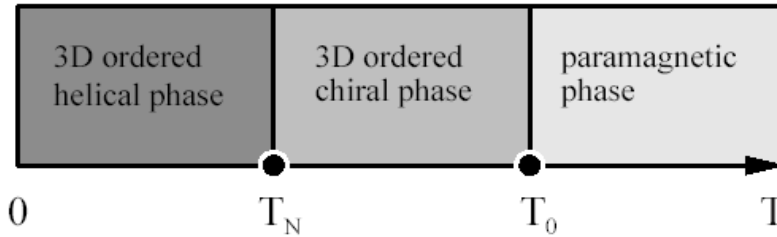


FIG.5.5 Representation of the phase diagram of fully frustrated quasi-1D planar helimagnets as predicted by Villain in 1978.

5. $\text{Gd}(\text{hfac})_3\text{NITR}$ Chains

containing the single ion anisotropy. As a consequence, these systems could experimentally verify the Villain's conjecture [29] predicted in 1978 for the so-called quasi-1D xy helimagnets. He stated that in addition to the usual *3D helical long range phase* (present at temperature $T < T_N$), when the interchain interactions (J_\perp) are no more negligible, and to the high temperature paramagnetic (disordered) phase, at intermediate temperatures a stable *chiral phase*, characterized by the breaking of the translational invariance but with no violation of the invariance regarding spin rotations and time reversal, is established (see FIG.5.5).

In the chiral phase the spins can be depicted as a collection of corkscrews turning all clockwise or counterclockwise in the x - y plane but with phases randomly distributed.

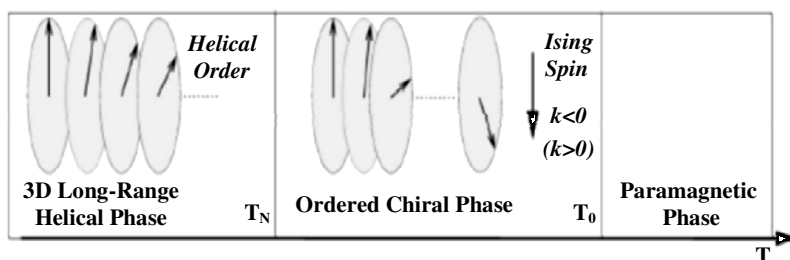


FIG.5.6 Pictorial view of the spins arrangements in the Chiral and in the Helical Phase [94].

5.1.4 DC Susceptibility Measurements

Low temperature measurements of molar susceptibility [93], more refined with respect to the early ones, were carried out.

As can be pointed out from TABLE 5.1, the calculation of the coupling constants for the four samples shows the competition

5. Gd(hfac)₃NITR Chains

between nn and the nnn exchange interactions: from the values indicated, a full frustration in the iPr and Et sample is evident, leading to a *helical order* with $Q=\pm 0.399\pi$ and $Q=\pm 0.397\pi$ respectively, very close to the value $\pm\pi/2$ expected in the limit for $\delta, \delta' \rightarrow \infty$. For systems with R=Me, Ph the frustration is much weaker and the helical range order would be characterized by $Q=\pm 0.206\pi$ and $Q=\pm 0.175\pi$ respectively. This behaviour is confirmed also by the exponents of the fitting function $\chi_M \sim CT^{-\alpha}$. They were found to be [97]:

SAMPLE	$J_1(\text{Gd-R})$	$J_2(\text{Gd-Gd})$	$J'_2(\text{R-R})$
Gd(hfac)₃NITPh	1.85K	-0.33K	-4.49K
Gd(hfac)₃NITMe	6.10K	-0.14K	-19.9K
Gd(hfac)₃NITPr	6.02K	-0.12K	-18.7K
Gd(hfac)₃NITet	5.05K	-0.98K	-7.67K

TABLE 5.1 Exchange coupling constants calculated from transfer matrix method for Gd(hfac)₃NITR compounds, as extracted from molar susceptibility.

$$\begin{array}{ll}
 \alpha=1.33 & \text{for R=Ph} \\
 \alpha=1.17 & \text{for R=Me} \\
 \alpha=0 & \text{for R=Et} \\
 \alpha=0.44 & \text{for R=iPr.}
 \end{array}
 \tag{5.7}$$

5. Gd(hfac)₃NITR Chains

In no cases the magnetic behaviour is proper of a ferro- or antiferromagnetic chain: the dominant overall behaviour is antiferromagnetic for Isopropyl and Ethyl compounds while it is ferromagnetic-like for chains containing Methyl and Phenyl.

5.1.5 Specific Heat Measurements

Further information have been obtained from *specific heat measurements*: in FIG. 5.7 experimental results are reported [93]. Also in this case the different behaviour of the two pairs of samples is clear. In FIG. 5.7(a) the specific heat of the derivatives with R=Me, Ph (*weakly frustrated systems*) are plotted. In the high temperature region $C_p/R \propto T^3$, as expected from the *lattice contribution*. At low temperature ($T < 1\text{K}$) this contribution is two orders of magnitude smaller than the magnetic one. The most important low-T feature is the presence of a *neat peak* for both samples, at $T \sim 0.6\text{K}$ and in particular at $T = 0.6\text{K}$ for Phenyl compound and at $T \sim 0.68\text{K}$ when R=Me. This anomaly is in good agreement with the one displayed by susceptibility measurements where a *change in the slope* of the curve occurred [93] (data not reported).

In the temperature range below the peak, the behaviour $C_p/R \propto T^{3/2}$ is typical of a 3D *quantum spin-wave contribution*. In the light of these findings and taking into account the λ -shape of the peak, a transition to a 3D phase of ferromagnetic nature occurs at $T \sim 0.6\text{K}$.

The values of the so-called *total anomalous entropy* (calculated by subtracting lattice contribution to the low temperature extrapolation) resulted $\Delta S/R = 2.76(7)$ and $2.65(8)$ for Gd-Me and Gd-Ph respectively, close to the value $4\ln 2$ expected for a system constituted by two sublattices with $S=7/2$ and $s=1/2$ [93].

5. Gd(hfac)₃NITR Chains

In FIG.5.7(b) data for Gadolinium chains with R=iPr, Et are reported. In this case the behaviour of the specific heat is deeply different from the one for weakly frustrated systems. In fact these *fully frustrated systems*, do not present the T^3 temperature dependence at high temperatures and a peak occurs for both compounds, at $T \sim 2$ K. At low temperatures the behaviour of the

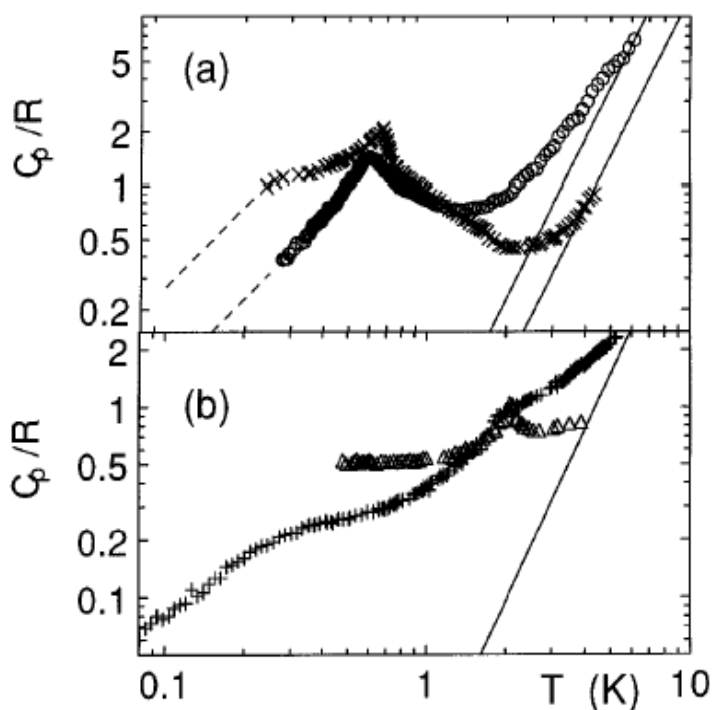


FIG.5.7 Preliminary experimental data of specific heat as a function of temperature for the four samples investigated. In (a) $R=Ph$ (o) and $R=Me$ (x) are reported, while (b) refers to $R=iPr$ (Δ) and $R=Et$ (+) [93].

specific heat tends to a plateau for both compounds around $T=500$ mK. At very low temperatures, the data on Gd-Et show an almost linear behaviour ($C_p(T) \sim 0.8T$).

5. $\text{Gd}(\text{hfac})_3\text{NITR}$ Chains

The total entropy extracted is $\Delta S/R=2.74(4)$, close to the total value $4\ln 2$: this means that, also in these measurements, all the magnetic contribution has been evidenced. It has to be remarked that the peak does not signal a Schottky anomaly related to hyperfine interactions or magnetic impurities, because the calculations give unrealistic values for the anisotropy of Gadolinium ion [95].

In the next section we will analyze the nature of the anomalies in both compounds.

5.2 Spin Dynamics

To investigate the spin dynamics in the low temperature region, where anomalies are present in χ and C_p , novel and more accurate measurements of χ , C_p and longitudinal muon relaxation rate λ , have been performed. Here below we present the results for three compounds of the family. These new measurements have been performed also to verify the occurrence of Villain's conjecture [29].

5.2.1 $\text{Gd}(\text{hfac})_3\text{NITPh}$

Specific Heat

The ability of specific heat measurements [94] to detect λ -peaks in correspondence to the phase transitions was extensively used. The results are shown in FIG. 5.8.

One can notice the presence of a sharp λ -peak at temperature $T_N \approx 0.63\text{K}$ [94] in very good agreement with the early

5. $\text{Gd}(\text{hfac})_3\text{NITR}$ Chains

measurements. Transfer matrix calculations performed treating the interchain interactions in the *mean field approximation*, gave $T_N=0.64\text{K}$. This is a clear indication that the peak displayed in

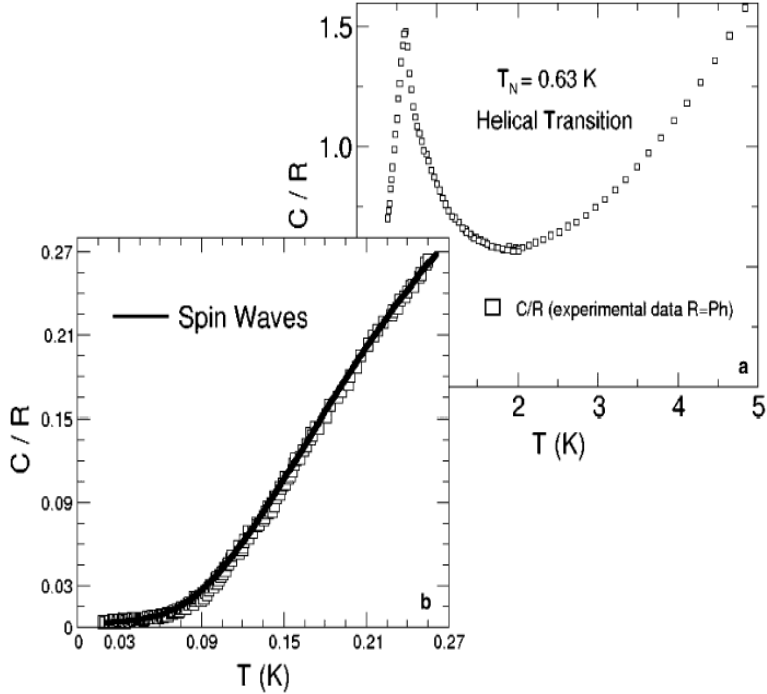


FIG.5.8 Specific heat data as a function of temperature: the 3D helical transition is signalled by the λ -peak at $T_N=0.63\text{K}$ (RIGHT). Very low temperature behaviour of specific heat as a function of T is well-fitted by a 3D spin waves model with strong anisotropic interactions (LEFT) [94].

this curve is related to the *3D helimagnetic phase transition*.

The behaviour of C/R as a function of temperature below the peak gives a definitive support: in fact $C/R \propto T$ just below the peak, while at lower temperatures $C(T) \propto T^\alpha$ where $2 < \alpha < 3$: this is

5. Gd(hfac)₃NITR Chains

typical of *free 3D spin-waves* characterized by *strong anisotropic interactions* [98].

μSR

μSR measurements on Gd(hfac)₃NITPh have been performed [58] at Paul Scherrer Institute facility on the LTF beam line. The *powder sample* used have been inserted in a small and soft sample holder made up of mylar for a good thermalization, mounted on the edge of the probe and then put in the cryostat where the experiment takes place. Measurements have been performed in *Zero Field* in the temperature range 0.02K<T<40K.

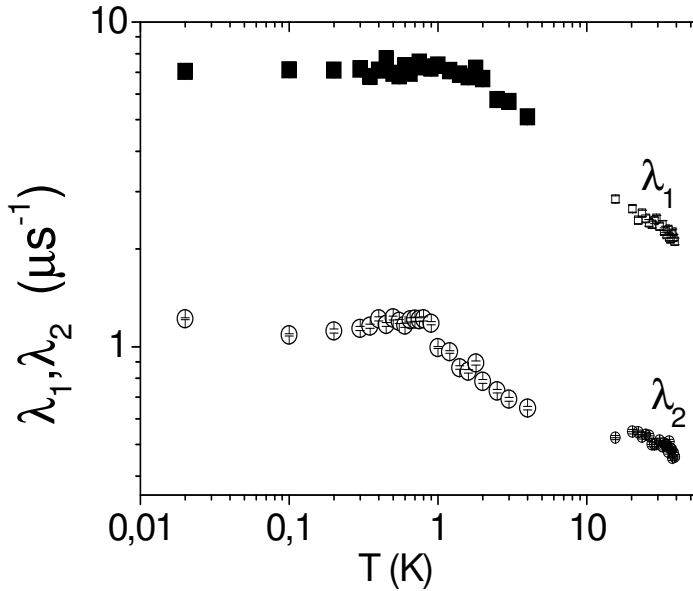


FIG.5.9 Zero-field measurements of muon longitudinal relaxation rates (fast λ_1 and slow λ_2 components) as a function of temperature for Gd(hfac)₃NITPh extracted from muon asymmetry [58].

5. Gd(hfac)₃NITR Chains

The muon asymmetry a_0 in all the temperature range investigated, after the subtraction of the background contribution, can be fitted by the function

$$a_0 = a_1 \exp(-\lambda_1 t) + a_2 \exp(-\lambda_2 t) \quad (5.8)$$

where λ_1 and λ_2 are the fast and slow relaxation rates, respectively, and $a_1/a_2 \sim 2$. The *bi-exponential behaviour* of the depolarization function suggests the presence of, at least, two muon implantation sites giving rise to two relaxation times due to different environments. The relaxation rates are plotted in FIG. 5.9.

As can be clearly seen, both λ_1 and λ_2 show the same qualitative temperature dependence: in the temperature range investigated they increase progressively, pass through a shoulder and reach a plateau at $T \sim 0.75\text{K}$; the flattening persists till the lowest temperature measured.

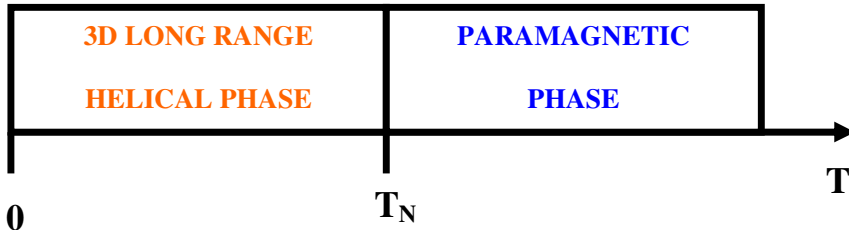


FIG.5.10 Phase diagram for weakly frustrated systems (Gd-Ph and Gd-Me chains).

The temperature at which the shoulder occurs ($T \sim 0.75\text{K}$) corresponds roughly to the 3D helimagnetic transition

5. Gd(hfac)₃NiTR Chains

temperature displayed in the specific heat ($T \sim 0.6\text{K}$). The difference in the temperature at which the anomalies occur in λ and C/R is ascribed to the low precision of the thermometer and the low thermal conductivity of the powder sample in the μSR measurements.

The expected peak in the muon relaxation rate (see section 5.2.3, Gd-Et case, for a more detailed discussion) is probably quenched by the insurgence of low temperature ($T < 0.75\text{K}$) *spin excitations* occurring at frequency near to the precession frequency of the muon polarization, which is of the order of 10kHz (i.e. $\sim 0.5\text{Oe}$) in our case. The flattening of $\lambda(T)$ suggests that these spin excitations have a quantum origin. The presence of an anomaly in C/R and $\lambda(T)$ is typical of a phase transition where the two-spin ($\propto \lambda(T)$) and the four-spin ($\propto C/R$) correlation functions diverge.

5.2.2 Gd(hfac)₃NiTiPr

Susceptibility

The preliminary susceptibility measurements which didn't show any anomaly in these systems needed a confirmation.

A run of magnetic susceptibility measurements very accurate (steps of 0.02K) around the temperature $T \sim 2\text{K}$ (where C_p displays a peak, see also next sub-paragraph) has been recently performed. The results are plotted in FIG.5.11 for Gd-iPr derivative at a very low field of 5.5Gauss [58][99]: this value has been chosen in order to be far from the critical field ($H_c = 2.06\text{T}$), where the system changes its spin configuration because of distortion effects caused by the external field itself. As can be clearly seen especially in the inset of FIG.5.11, where the data

5. $\text{Gd}(\text{hfac})_3\text{NITR}$ Chains

around $T=2\text{K}$ are shown, no anomaly has been found. This is a confirmation of the insensitivity of the susceptibility to the physical mechanism giving rise to the specific heat peak.

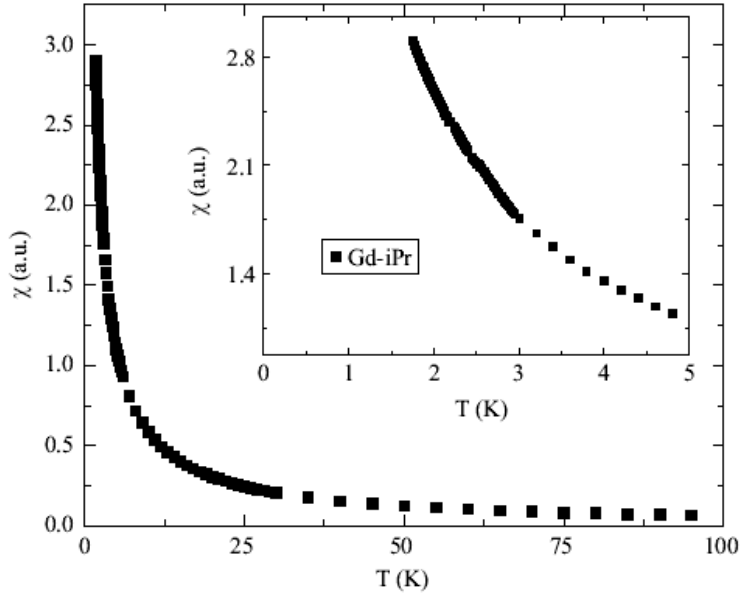


FIG.5.11 Susceptibility data as a function of temperature for $\text{Gd}(\text{hfac})_3\text{NITiPr}$. INSET: susceptibility plot around 2K: no anomaly is present.

Specific Heat

Since preliminary specific heat measurements gave the most interesting results, new experiments [57] have been performed in different periods on samples deriving from different batches and with different age (see FIG.5.12).

The most striking property evidenced from FIG.5.12 is still the peak occurring at $T=2.09(\pm 0.01)\text{K}$ for all the samples measured.

5. $\text{Gd}(\text{hfac})_3\text{NITR}$ Chains

The differences between the five curves depend on the *age of the compound*. In fact, the newer the sample the higher the peak: ageing effects are evident as the lability of the organic radicals causes the chains to cut in shorter segments, loosing most of

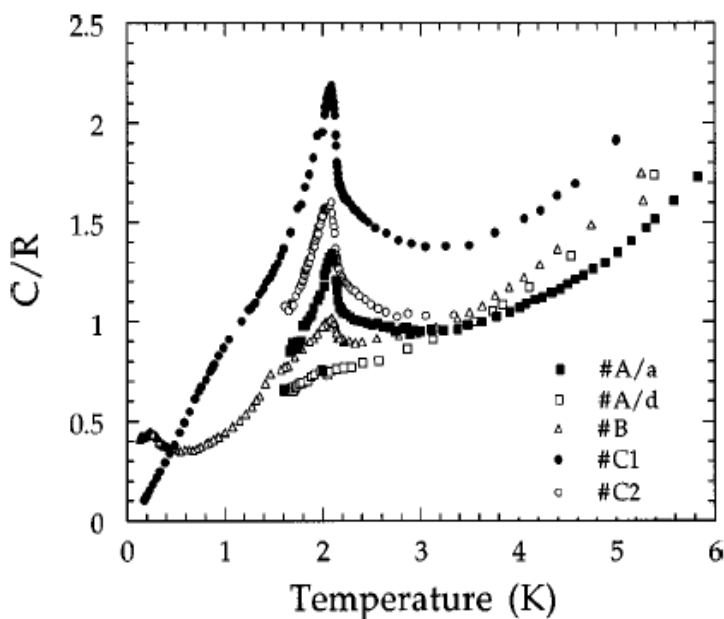


FIG.5.12 Specific heat measurements as a function of temperature for $\text{Gd}(\text{hfac})_3\text{NITiPr}$ performed in various runs on samples from different batches and with different ages and pressure [57].

their properties, as will be explained in the following discussion. For instance differences between the results obtained in first (*A/a*) and second run (*A/d*) performed four months later, on sample *A* of FIG.5.13 are clear; looking at the results on *B* sample we notice that the peak becomes rounded and tends to vanish when the sample becomes older.

Another parameter that alters the quality of the samples is the *compression*; in fact the samples *C1* and *C2* come from the same

5. $\text{Gd}(\text{hfac})_3\text{NITR}$ Chains

batch and measured at the same time, but the pellets for the measurements have been prepared pressing the powders with two different pressures, respectively 1tonn/($\phi=8\text{mm}$) for *C1* and 2tonn/($\phi=8\text{mm}$) for *C2*.

The most reliable information can be obtained from sample *C1*

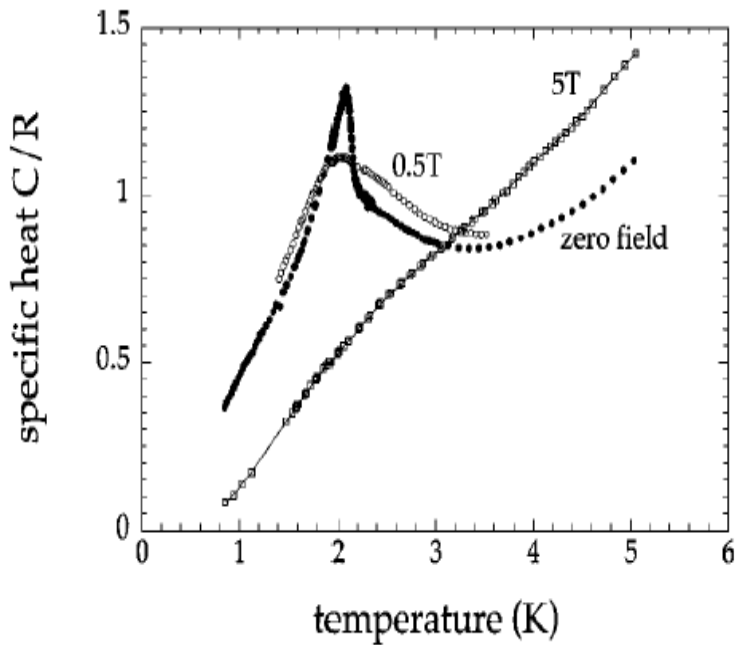


FIG.5.13 Specific heat data versus temperature for $\text{Gd}(\text{hfac})_3\text{NITiPr}$ performed in Zero Field and in two different applied field ($H=0.5\text{T}$, 5T). The smoothing of the peak with increasing field demonstrates the magnetic origin of the anomaly [100].

since all of the procedures regarding preparation have been the best ones. In this sample, the curve below the peak decreases almost linearly with temperature between 1K and 175mK, as already noticed in preliminary measurements of Gd-Et , which is characteristic of systems with strong antiferromagnetic

5. $\text{Gd}(\text{hfac})_3\text{NITR}$ Chains

interactions. The dependence of the specific heat behaviour on the sample quality rules out that the peak is related to the excitations of chiral domain walls and suggests, instead, that it originates from a real phase transition.

In a further run of specific heat measurements [100] performed about three years after the previous one (see FIG.5.13), the robust and neat λ -peak is still reproducible in the same position around $T=2\text{K}$ and below the anomaly the behaviour is still almost linear as a function of the temperature, which confirms that the system remains 1D also below the phase transition.

These measurements have been performed in Zero Field (ZF) and for $H=0.5\text{T}$ and $H=5\text{T}$: the peak smoothens with increasing field,

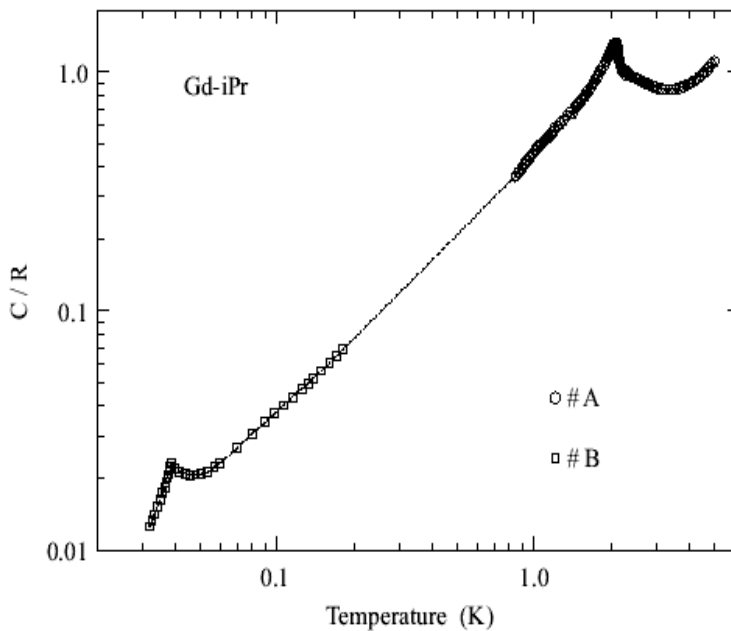


FIG.5.14 Temperature dependence of specific heat data in an enlarged scale. At very low temperature, a new neat λ -peak has been detected, suggesting the presence of a phase transition.

5. $\text{Gd}(\text{hfac})_3\text{NITR}$ Chains

indicating the *magnetic origin* of the anomaly. All these experimental observations suggest that the peak observed could be due to the insurgence of the *chiral phase transition* at temperature T_0 defined by Villain [29]. In this case the four-spin correlation function (proportional to C) should show a neat λ -peak in C/R data as typical of a genuine phase transition, while the two-spin correlation function (proportional to the magnetic susceptibility) shows no anomaly.

To investigate the possible occurrence of a low-temperature phase transition, very low-T specific heat data were collected (see FIG.5.14 [99]).

As can be seen from the plot (FIG.5.14), new data taken from 300mK to 29mK, represented by open squares, show a second anomaly (in the form of λ -peak) occurring at $T=39\text{mK}$. The actually accepted hypothesis is that the peak is due to the occurrence of the Villain's transition to the *3D long-range helical order* ($T_N \approx 39\text{mK}$). Again the sharp form of the peak suggests the presence of a phase transition; the association of this anomaly to a Schottky-like contribution has been ruled out [99].

μSR

For a complete understanding of the spin dynamics of fully frustrated systems, we have also performed μSR measurements [58] at ISIS Muon Facility and at PSI Muon Facility on powder samples in the temperature range 0.04-300K in Zero Field and in a longitudinal field of 500Oe.

Information can be obtained from *Muon Asymmetry*, which probes the interactions between muons and lattice.

Muon asymmetry A , shown in FIG. 5.15 at $T=4\text{K}$, has been fitted in the entire temperature range by a single stretched exponential

5. Gd(hfac)₃NiTR Chains

decay function whose expression is

$$f(t) = C e^{-(\lambda t)^{0.5}} \quad (5.9)$$

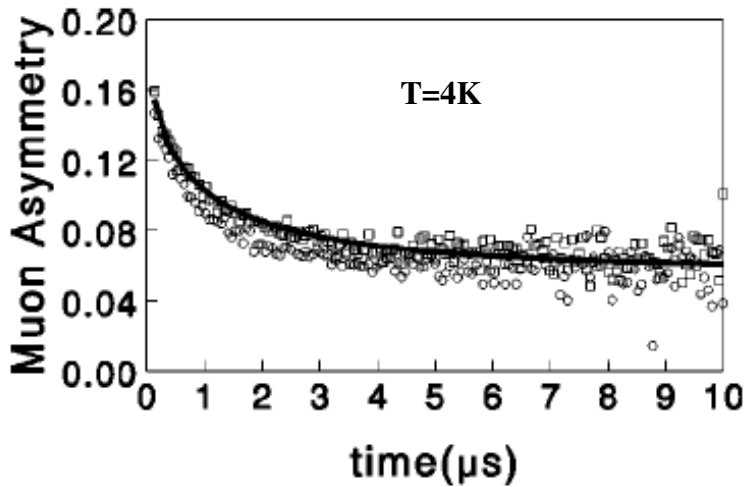


FIG.5.15 Muon asymmetry as function of time at T=4K for Gd(hfac)₃NiTiPr. The solid line represents the fit obtained by a stretched exponential function.

where C is the total asymmetry depending on the experimental geometry (at ISIS ~ 0.25 , at PSI ~ 0.30).

This analysis already gives us at least two important information: (i) the stretched behaviour suggests the presence of a distribution of relaxation rates in the sample related to different sites in the sample where muons implant; (ii) the regular behaviour of the asymmetry curves signals the absence of local fields caused by long-range magnetic order at muons sites, since in this case loss of asymmetry or an oscillation (or a Kubo-Toyabe function) in the asymmetry would be expected, due to the precession of the muon spin around the local field.

5. Gd(hfac)₃NiTiPr Chains

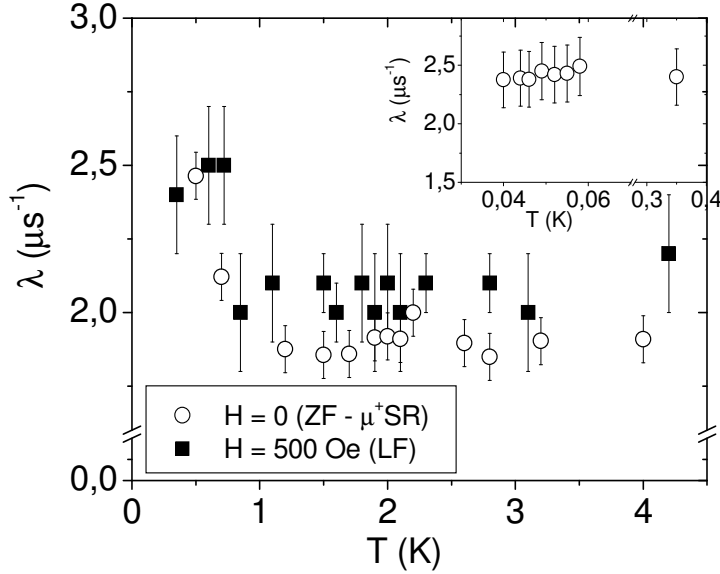


FIG.5.16 Muon longitudinal relaxation rate for Gd(hfac)₃NiTiPr powder sample as a function of temperature in Zero Field and in a longitudinal field of 500Oe. No anomalies related to possible phase transitions have been detected in 0.04-300K temperature range investigated. INSET: data taken at very low temperature in Zero Field.

Muon relaxation rate as a function of temperature (extracted from eq.5.9) is reported in FIG.5.16 in Zero Field and in a longitudinal field $H=500\text{Oe}$. The behaviour of this parameter does not show any anomaly in the whole temperature range investigated, especially around $T_0=2.08\text{K}$, but a rapid increase of λ for $T<1\text{K}$ is observed. Because of experimental limits and of the temperature sensor calibration, we could not reach $T_N\cong 39\text{mK}$ (the nominal 0.04K is probably a higher T). For this reason from measurements of λ , no support to specific heat data that show an anomaly at 39mK can be given. The increase of λ for $T<1\text{K}$ can be related to a “resonance” with a *spin-wave mode* with

5. Gd(hfac)₃NITR Chains

progressive increase of correlation lengths [100]. It should be also noticed the flattening of λ for $T < 0.5\text{K}$. As regards the absence of anomalies at T_0 , the data are coherent with susceptibility data, since, both susceptibility and μSR measurements probe the spin-pair correlation function which is not sensible to chiral order as discussed above.

5.2.3 Gd(hfac)₃NITet

The recent data [101] on Ethyl derivative have shown evidences of Villain's conjecture [29] as discussed below. Also in this case susceptibility, specific heat and μSR measurements have been performed.

Susceptibility

Susceptibility measurements on this compound have been performed with a SQUID Magnetometer in the temperature range between 300K and 1.75K with steps of 0.01K around $T \sim 2\text{K}$. New information can be obtained from the curve shown in FIG. 5.17: in fact an *abrupt increase* in the slope of susceptibility, as a function of temperature, is clearly visible at $T \approx 1.87\text{K} \pm 0.02\text{K}$. As

for Gd-iPr sample, susceptibility was measured as $\chi = \left(\frac{M}{H} \right)_{H \rightarrow 0}$ in

a very small field of 5.5Gauss. The sample has been measured in Field Cooled (FC) and Zero Field Cooled (ZFC) conditions: within experimental error, the two curves superimpose, i.e. no mechanism driven by slow relaxation of magnetization, as it happens for *superparamagnets* and *spin glasses*, is present in the temperature range investigated. The anomaly detected can be ascribed to the onset of a 3D phase transition, since, as already

5. Gd(hfac)₃NITR Chains

mentioned, no measurable effects can be detected by two spin correlation function related to susceptibility as regards the chiral

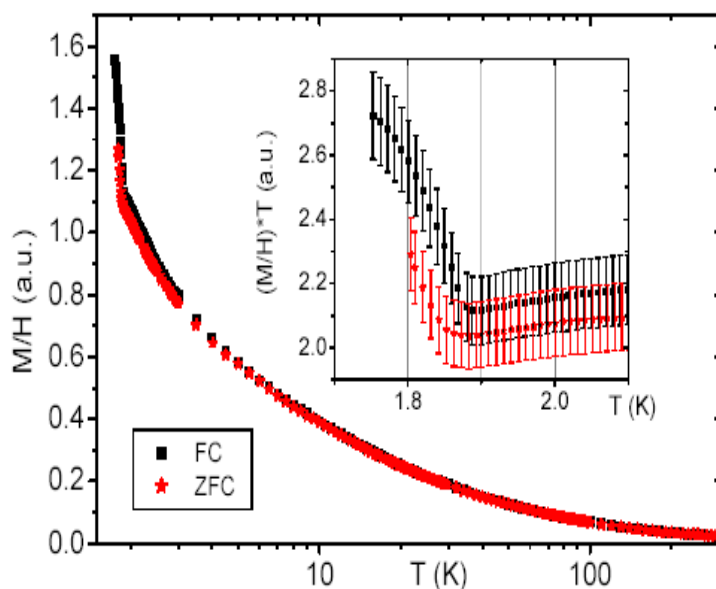


FIG.5.17 Magnetic susceptibility *vs* temperature of Gd(hfac)₃NITet performed with ZFC and FC techniques from 300K to 1.75K. INSET: detail of the anomaly displayed by the powder sample at $T_N=1.87$ K in the plot of $\chi \cdot T$ *vs* T .

long range order. This hypothesis is confirmed and supported by the data reported in the following sections.

Specific Heat

Specific heat measurements have been performed on microcrystalline powder in the temperature range 175mK-100K,

5. Gd(hfac)₃NITR Chains

to exploit the behaviour of C/R in all the three phases predicted theoretically by Villain [27-29]. The accuracy of the measurements was kept within 1% of the absolute temperature value measured.

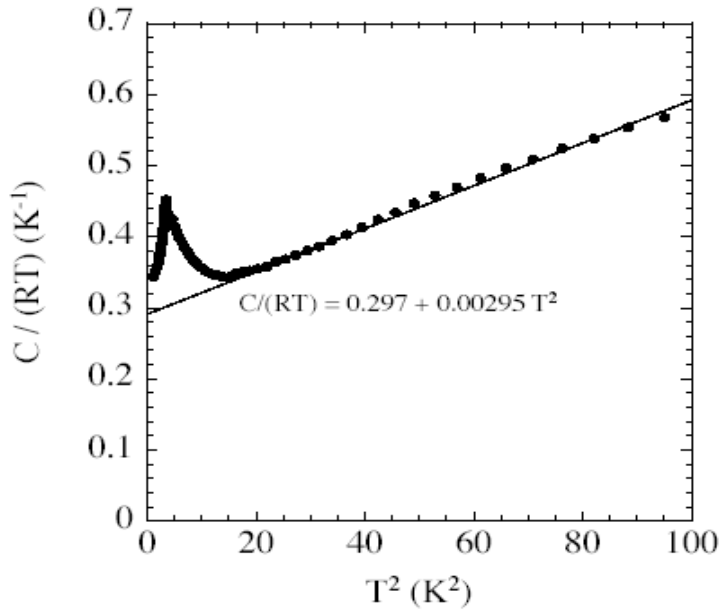


FIG.5.18 Specific Heat data as a function of temperature for Gd(hfac)₃NITet powder sample plotted as $C/(RT)$ vs T^2 . The solid line represents the fitting function of the high temperature data; the fit equation is also reported.

In FIG. 5.18 the specific heat normalized to the *gas constant* ($R=8.314\text{Jmol}^{-1}\text{K}^{-1}$) is shown. Plotting specific heat as $C/(RT)$ vs T^2 , it can be shown that, in the range between 4K and 10K, data are well-fitted by the function

$$C/(RT)=0.297+0.00295T^2. \quad (5.10)$$

5. Gd(hfac)₃NITR Chains

Eq.5.10 is the result of two different contributions to the specific heat: the second term in eq.(5.10) is the *Debye-like lattice contribution* ($C_p \propto T^3$ at high temperature), while the first term is related to the presence of *spin waves*. This overall behaviour had

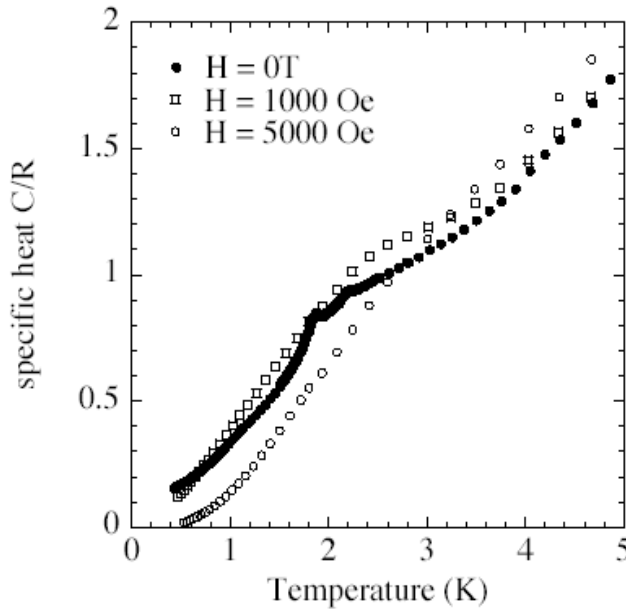


FIG.5.19 Specific Heat normalized to the gas constant as a function of temperature for Gd(hfac)₃NITet: these recent measurements have been performed for H=0, 1000, 5000Oe and they display two λ -peaks signalling the two phase transitions researched.

been detected also for Gd-iPr derivative (see section 5.2.2 Specific Heat [57][99-100]) and it is peculiar for 3D helimagnets in this range of temperature.

Let's analyze now the low-temperature region (FIG. 5.19): the most important feature is the presence of two anomalies in the temperature range $1.8\text{K} < T < 2.2\text{K}$: the first bump has been

5. Gd(hfac)₃NITR Chains

detected at $T_0=2.19\pm0.02\text{K}$ and the second (λ -peak) at $T=1.88\pm0.02\text{K}$, as predicted by transfer matrix calculations for the phase transition temperatures T_N and T_0 (Villain's conjecture [28-29]).

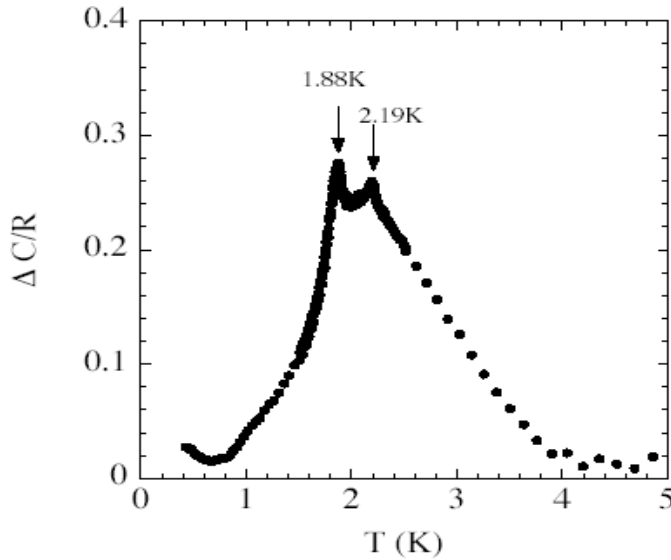


FIG.5.20 Excess of specific heat normalized to the gas constant R obtained from the subtraction of the contributions eq. (5.9) from the total specific heat at $H=0\text{T}$ of $\text{Gd}(\text{hfac})_3\text{NITet}$; the two λ -peaks are clearly observed.

By repetitive measurements both peaks have been detected reproducibly.

In FIG.5.20 we have plotted the *excess of specific heat*, i.e. the specific heat obtained from the subtraction of the term $C/R=0.297T+0.00295T^3$ from the total C/R . The two anomalies are now more evident. The order of the transitions has been inferred from the fact that no hysteresis has been detected with

5. Gd(hfac)₃NITR Chains

cycling temperature: this means that both the transitions are of an order higher than the first one. The measurements performed with various fields applied to the sample and shown in FIG. 5.19, confirm also in this case the magnetic origin of the transitions signalled by λ -peaks: in fact the peaks disappear when the magnetic field is applied.

μ SR

The μ SR measurements give unique information about phase transitions as the muons are a local probe. Measurements have been done at Paul Scherrer Institute in Villigen (CH) on GPS beam line. We have investigated the temperature range between 1.5K and 10K in Zero Field (ZF) configuration on a powder sample. The muon asymmetry is well-fitted in the whole range by the sum of two exponential components after the subtraction of the *background contribution*. The corresponding expression of the depolarization curves is:

$$a_0 = a_1 \exp(-\lambda_1 t) + a_2 \exp(-\lambda_2 t) \quad (5.11)$$

where λ_1 and λ_2 represent the *muon relaxation rates* related to, respectively, a fast and a slow relaxing component. The occurrence of two different relaxation rates for muons means, also in this case, that they implant at least in two different sites inside the sample.

Following the temperature dependence of a_0 , we can obtain the T-behaviour of the relaxation rates. Before going to details, let's introduce the theoretical background of the relaxation rate behaviour in presence of phase transitions.

In the *weak-collision approach*, that is when fluctuations are

5. Gd(hfac)₃NITR Chains

faster than muon (or nuclear) resonance frequency, the general expression for muon relaxation rate λ is (see also [48][100]):

$$\lambda \propto \gamma^2 [J_+(\omega_L) + J_-(\omega_L)] \quad (5.12)$$

where ω_L is the muon resonance frequency, γ the muon gyromagnetic ratio and

$$J_{\pm} = \int dt e^{-i\omega_L t} \langle h_{\pm}(t) \cdot h_{\pm}(0) \rangle \quad (5.13)$$

are the spectral densities related to the correlation functions for *dipolar* and *contact field components* in the transverse directions.

Rewriting eq.(5.12) in terms of *collective spin components* $\vec{S}_{\vec{q}}$ and $\vec{S}_{\vec{q}}$ respectively for organic radicals and Gadolinium ions spins, whose fluctuations are supposed to be isotropic, and considering three different correlation functions involving two spins (\vec{S} with \vec{S} , \vec{S} with \vec{S} and \vec{S} with \vec{S}), eq.(5.12) becomes

$$\lambda \propto \gamma^2 \frac{1}{N} \sum_{i,j=1,2} \sum_q |h_q|^2 \int dt \langle \vec{\sigma}_{iq}^+(0) \vec{\sigma}_{iq}^-(t) \rangle = \gamma^2 \frac{1}{N} \sum_{i,j=1,2} \sum_q |h_q|^2 |\vec{\sigma}_{iq}| |\vec{\sigma}_{jq}| \frac{1}{\Gamma_q} \quad (5.14)$$

with $\vec{\sigma}_1 = \vec{S}$, $\vec{\sigma}_2 = \vec{S}$, $\vec{h}_{\vec{q}}$ is the Fourier Transform of the lattice functions, coupling muons to the spins of the magnetic ions and

$\Gamma_{q_i} = \frac{\omega_e}{\xi_i^z} g(x)$ is the *decay rate* of the *collective spin fluctuations*. Here ω_e^i are the so-called *Heisenberg exchange frequencies* and $f(x)$ and $g(x)$ are homogeneous function in x ($x=q_i \xi_i$ with ξ_i being the correlation lengths).

5. Gd(hfac)₃NITR Chains

Let's investigate now the behaviour of the relaxation rate above a phase transition temperature which will be referred as T_c . Starting from eq.(5.14) and expanding the expression of $\vec{h}_{\vec{q}}$ around the \vec{Q} critical wave-vector of the long-range order below T_c , using scaling arguments and after some algebra the expression for muon relaxation rate is

$$\lambda \propto \sum_i^3 (\gamma h_{eff}^i)^2 \frac{1}{N} \sum_{q_i} \frac{\xi_i^{2-\eta_i} f(x)}{\omega_e^i \xi_i^{-z_i} g(x)} \quad (5.15)$$

where h_{eff}^i represents hyperfine fields felt at muons sites (due to Gadolinium and radical spins arrangement) in the ordered configuration and \vec{q}_i are wave vectors. Converting the summation in eq.(5.15) in an integral which converges to unity, λ can be rewritten as

$$\lambda \propto \sum_i^3 (\gamma h_{eff}^i)^2 \frac{1}{\omega_e^i} \xi_i^{z_i-d+2-\eta_i} \quad (5.16)$$

and, since $\xi_i \propto (T-T_c)^{-\nu_i}$, one would expect a divergence at T_c i.e.:

$$\lambda \propto \sum_i^3 (T-T_c)^{-\eta_i} \quad (5.17)$$

with $\eta_i = \nu_i(z_i - 1 - \eta_i)$ where η_i is the *critical exponent* introduced by Fisher (1967) as a correction to the static two-spin correlation function with respect to its behaviour in the *mean field approach* (here $\eta=0$ and $\eta \approx 0$ in 3D systems), while ν_i and z_i are further critical exponents.

The most important feature to be pointed out from the μ SR data

5. Gd(hfac)₃NITR Chains

(FIG.5.21) is an abrupt increase of both muon relaxation rates below $T \sim 3\text{K}$ with a flattening for $T < 1.9\text{K}$ persisting till 1.5K , the lower temperature investigated.

The ratio between the values of both relaxations rates at $T = 3\text{K}$ and the values at $T = 1.88\text{K}$ where the plateau occurs is

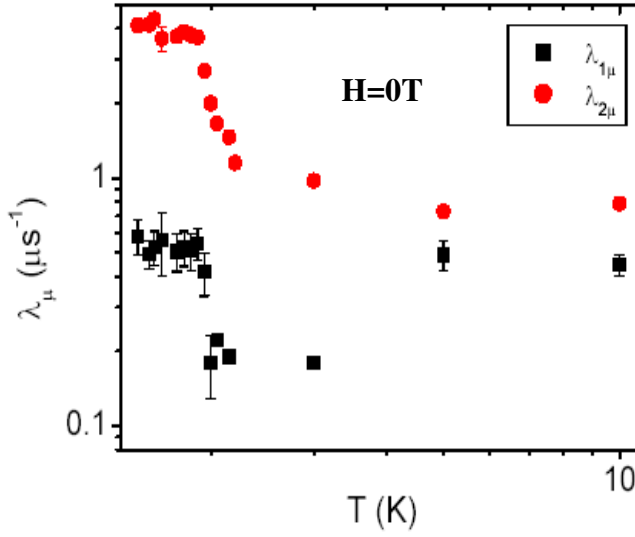


FIG.5.21 Fast (λ_1) and slow (λ_2) components of the muon relaxation rates as a function of temperature in Zero-Field in Gd(hfac)₃NITiEt.

$$\lambda_{ratio} = \frac{\lambda_{i\mu}(T = 1.88K)}{\lambda_{i\mu}(T = 3K)} \cong 4 \quad (5.18)$$

suggesting a divergence due to the phase transition to 3D long-range helical order. The flattening observed for $T \leq 1.85\text{K}$ is possibly related to *low-energy excitations*, like e.g. spin-waves, as previously detected also in Gd-iPr derivative [58]. We can

5. Gd(hfac)₃NITR Chains

thus conclude that the abrupt increase marks the 3D long-range order phase transition occurring at the same temperature of the change in the slope of magnetic susceptibility and the anomaly detected at $T=1.87\text{K}$ in specific heat measurements. Also in this case no muon precession has been detected in the temperature range investigated, i.e. local spins fluctuations are faster than muon precession (for $H=0.5\text{mT}$ $\nu_{\mu}\approx 60\text{kHz}$) also in the 3D helimagnetic phase.

Finally we conclude that the peak observed at higher temperature $T_0=2.19\text{K}$ in C/R is ascribed to the transition to chiral phase. This observation allows to verify entirely the Villain's conjecture [28-29].

5.3 Conclusions

In this chapter a thorough experimental study of quasi-one dimensional *frustrated molecular chains* has been done.

In particular the attention was focussed on four compounds of the family of Gd(hfac)₃NITR chains containing, in the radical centre, Iso-Propyl (iPr), Phenyl (Ph), Ethyl (Et) or Methyl (Me) groups. They display properties never observed before from an experimental point of view in magnetic systems: in fact they are characterized by competition between nearest-neighbour (nn) ferromagnetic coupling interactions ($J_1>0$) and next-nearest-neighbour (nnn) antiferromagnetic interaction between Gd³⁺ ions ($J_2<0$, $S_{\text{Gd}}=7/2$) and between radicals ($J'_2<0$, $s_{\text{Rad}}=1/2$) which are dominant. They also have weak dipolar intrachain and exchange interchain (J_{\perp}) interactions which become relevant at low temperature.

These derivatives can be classified into two different groups: the samples with $R=\text{Ph, Me}$ named *weakly frustrated systems*, and

5. Gd(hfac)₃NITR Chains

The samples containing R=iPr, Et called *fully frustrated systems*. This classification has been done taking into account the strength of the exchange coupling: when the ratio between *nnn* and *nn* interactions exceeds a certain value ($2(\delta+\delta')>1$), the system is fully frustrated, otherwise the system is weakly frustrated.

For Phenyl and Methyl compounds a change in the slope of $\chi(T)$ has been detected at $T\sim 0.6\text{K}$ for both samples in preliminary measurements [93], in correspondence to a peak in specific heat data at the same temperature for Gd-Ph and at $T\approx 0.68\text{K}$ for Gd-Me [93]. Further investigation on Gd-Ph performed through μSR measurements confirmed this feature. In fact a sharp increase of the muon longitudinal relaxation rate λ for T approaching 0.6K was observed. For $T<0.6\text{K}$ spin waves excitations possibly occur and λ tends to flatten. The overall ferromagnetic behaviour of susceptibility and the $T^{3/2}$ temperature dependence of the specific heat in the region below the detected peak, characteristic of a 3D ferromagnetic quantum spin-wave contribution [94], led to the conclusion that the Gd-Ph system simply undergoes 3D long range phase transition of ferromagnetic type at $T\sim 0.6\text{K}$.

A more complex situation is instead found in **fully frustrated systems Gd-iPr and Gd-Et**: the strong competition between *nnn* and *nn* interactions and the presence of intrachain dipolar interactions creates an easy plane of magnetization in x - y plane perpendicular to the chain direction. Susceptibility, specific heat and μSR measurements demonstrated the occurrence of Villain's conjecture [29] in Gd-Et. Such conjecture can be described by a complex phase diagram including three magnetic phases; the novelty with respect to conventional quasi one-dimensional systems is related to the presence of an intermediate magnetic phase between the high temperature paramagnetic phase and the low temperature 3D long range magnetic ordered phase.

5. $\text{Gd}(\text{hfac})_3\text{NITR}$ Chains

Summarizing, it is assumed that in the different temperature regions the system is in the following different phases:

- $T > T_0 \rightarrow \text{PARAMAGNETIC PHASE}$
- $T_N < T < T_0 \rightarrow \text{ORDERED CHIRAL PHASE}$ (spins can be depicted as a collection of corkscrews turning all clockwise or counterclockwise in the x - y plane with phases randomly distributed)
- $T < T_N \rightarrow \text{3D ORDERED HELICAL PHASE}$

The temperature T_0 has been experimentally signalled by a neat λ -peak in specific heat at $T_0 \sim 2.08\text{K} \pm 0.01\text{K}$ for Gd-iPr and at $T_0 \sim 2.19\text{K} \pm 0.02\text{K}$ for Gd-Et [99][101]. The magnetic origin of this transition has been verified by measuring the specific heat in Zero Field and in different applied magnetic fields [100-101]: the peak rounded and vanished as the field magnitude was increased. The indication for a transition to chiral order at T_0 was further probed by the T -dependence of the specific heat below the peak, almost linear, i.e. proper of a 1D quantum spin-wave contribution and by the fact that for $T < T_0$ the residual magnetic entropy is of 59% of the total magnetic entropy [94], which is a too high value for a long-range ordered phase (for instance in TMMC for $T < T_N$ the residual magnetic entropy is 1%). The magnetic origin (chiral) of the transition has been finally proved by the absence of anomalies at T_0 in quantities testing the spin-pair correlation function, i.e. the magnetic susceptibility and the muon longitudinal relaxation rate λ .

Very low temperature specific heat measurements [99] performed on **Gd-iPr** revealed the existence of a 3D helical

5. $\text{Gd}(\text{hfac})_3\text{NITR}$ Chains

phase transition through a peak at $T \cong 39\text{K}$ where interchain interactions cannot be neglected. The difficulty in detecting this phase transition was ascribed to two main factors: first the entropy removed below this phase transition is really low and its observation is, consequently, subtle; secondly the degree of sample damage is often relevant preventing the transitions to take place. In fact ageing effects act on chains by cutting them into shorter segments and the coherence for 3D transition is destroyed; on the other hand the less strict requirement consisting in the establishment of the same chirality for each segment is, in practice, not influenced.

As regards the compound containing Ethyl, specific heat, susceptibility and μSR measurements gave clear indications for a transition to 3D long range order transition at $T_N \cong 1.88\text{K}$. More in details: (i) C/R shows a λ -peak at $T_N = 1.88 \pm 0.02\text{K}$ [101] thus suggesting a phase transition whose magnetic origin is assured by the fact that by applying a magnetic field during measurements, the peak smoothened; (ii) the 3D origin is, instead, assured by the abrupt increasing in the T -dependence of the susceptibility at $T_N = 1.87\text{K}$ [101] and confirmed by the increase of the muon longitudinal relaxation rate λ at the same temperature. Below T_N the presence of low energy excitations causes a plateau in $\lambda(T)$. These experimental evidences for Gd-iPr and Gd-Et are in agreement with theoretical predictions about different phase transitions predicted in the framework of the Villain's conjecture [28][29]: (a) the chiral phase transition, being the results of a randomly distributed phase configuration of the spins, can only be detected by specific heat measurements which probe the four-spin correlation function; (b) on the other hand no anomalies must be found both in susceptibility and in μSR data, which probe the two-spin correlation function related to long-range order phase transitions.

5. Gd(hfac)₃NITR Chains

The relative position in temperature of T_N and T_0 is confirmed and supported by theoretical calculations where it is predicted $T_N < T_0$. This is related to the Ising nature of the chirality; in fact chiral correlation length ξ_k , related to chirality-chirality correlation function through the expression

$$\langle k_1 k_{n+1} \rangle \approx A \exp(-na / \xi_k) \quad (5.19)$$

diverges exponentially with decreasing temperature as follows

$$\xi_k \approx \exp(|J|/T) \quad (5.20)$$

where J is the exchange coupling constant. On the other hand the spin correlation length ξ_s , related to spin-spin correlation function by the relation

$$\langle S_1 \cdot S_{n+1} \rangle \approx A' \exp(-na / \xi_s), \quad (5.21)$$

diverges as a power law with the following expression

$$\xi_s \approx |J|/T. \quad (5.22)$$

The final result is that chirality-chirality correlation function is stronger than the spin-spin correlation function, thus giving $T_N < T_0$.

In Table 5.2 the results obtained on the samples treated in this chapter are summarized.

5. Gd(hfac)₃NITR Chains

SAMPLE	TYPE	T _N	T ₀
Gd(hfac) ₃ NITPh	Weakly Frustrated System	~0.63K	No chiral phase
Gd(hfac) ₃ NITMe	Weakly Frustrated System	~0.68K	No chiral phase
Gd(hfac) ₃ NITiPr	Fully Frustrated System	~39mK	2.08K±0.01K
Gd(hfac) ₃ NITt	Fully Frustrated System	1.88K±0.02K	2.19K±0.02K

Table 5.2 Schematic summary of the crucial properties of the four compounds studied in this chapter.

General Conclusions

In this thesis we have studied, in collaboration with the University of Firenze and the University of Modena, some *1D molecular magnets* belonging to the class of the low dimensional systems which nowadays are available as a result of the improvement in synthesis methods of molecular chemistry. The experimental investigation was done by means of *magnetization measurements* and of *NMR* and μ *SR techniques*. In particular these two last techniques are very useful in complementing the macroscopic measurements, since they probe the microscopic electronic spin dynamics via the *hyperfine interactions* coupling the nuclei (muons) with the magnetic moments of the system.

We have focussed our attention on *CoPhOMe single chain magnets* (pure and “doped”) and on the *Gd(hfac)₃NITR* family of *frustrated helimagnetic quasi one-dimensional spin systems*.

CoPhOMe is the first single chain magnet which showed the slow dynamics predicted by the *Glauber Ising Kinetic Model* [1]. The characteristics of the slowing down of the magnetization at low temperatures have been investigated and found to follow a *thermally activated Arrhenius-like behavior* $\tau = \tau_0 \exp\left(\frac{\Delta}{T}\right)$. In the first part of this thesis we have studied the behavior of CoPhOMe doped with various concentrations of Zinc diamagnetic impurities.

Susceptibility measurements performed in Firenze [83-84][86] had shown that in the doped samples the Arrhenius behavior is still valid with an *energy barrier* Δ , equal to that of the pure sample but with a shorter *pre-exponential factor* τ_0 . The shorter the segments, the shorter τ_0 . It was also noticed that with increasing the dopant concentrations the *finite-size effects* are more and more relevant. In particular it was pointed out that finite-size effects were present also in the pure compound (the

General Conclusions

estimated length is about 3000/4000 spins). This conclusion was inferred by the fact that the predicted reduction by a factor two of the energy barrier expected in doped samples was not observed. Our NMR *Spin-Lattice Relaxation measurements* have added additional information about the spin dynamics. In the doped samples investigated the spin-lattice relaxation rate T_1^{-1} of protons has been found to display a maximum for $15\text{K} < T < 50\text{K}$ and a shoulder for $T < 15\text{K}$. This result is qualitatively similar to the one found in pure CoPhOMe (indicating two different relaxation mechanisms) but the same heuristic model used for CoPhOMe did not yield a satisfactory fit for the data. Furthermore the ^1H NMR *spectra* as a function of temperature show an anomalous broadening of the line width with decreasing temperature even above the temperature ($\cong 60\text{K}$) where the spins start to freeze, according to susceptibility data. Thus the initial interpretation of the two peaks in pure CoPhOMe based on the presence of two different thermally activated relaxation mechanisms related to two different sublattices in the system [58][79-80] has to be partially reconsidered in the light of the new data in the doped samples. Moreover new data showed that even in the nominally pure compound the finite-size effects introduced, in this case, by intrinsic natural defects are present. As a consequence regarding the shoulder observed at lower temperature in nuclear relaxation we propose tentatively that it is due to the collective reversal of all spins in each segment [87]. As regards the maximum at higher temperature we still claim that it is due to the slowing down of the Glauber spin dynamics but affected by the size of finite chains. Both these interpretations are only qualitative and speculative at this stage. Detailed quantitative model to describe the nuclear relaxation including finite-size effects and soliton-like type excitations needs to be developed.

General Conclusions

In the second part of this work we have investigated a family of compounds which presents a complicated puzzle of competing interactions, the **Gd(hfac)NITR molecular chains**, where R=Me, Ph, iPr and Et. We have studied only the last three derivatives. These compounds are characterized by the alternation of Gd³⁺ ions ($S=7/2$) and radical groups ($S=1/2$) along the chains. The resulting Hamiltonian consists in a term deriving from the easy-plane anisotropy normal to the direction of the chains, and three different intrachain interactions [58]: a ferromagnetic nearest-neighbor exchange coupling and two antiferromagnetic next-nearest-neighbor interactions involving the two different species of magnetic centers (Gd and R) along the chain. Depending on the relative strength of these interactions, the compounds can be classified into two different groups. The first group includes Me and Ph derivatives: they present a phase diagram constituted by two different phase, the paramagnetic one for $T>T_N$ and the 3D phase of ferromagnetic type for $T<T_N$. The *frustration* effects due to *competing interactions* are not strong in these systems, which are called *weakly frustrated*. We have investigated in particular the Gd-Ph chain through *specific heat* and μ SR measurements. Our experimental work has confirmed the occurrence of a 3D phase transition of ferromagnetic nature as clearly manifested by the neat λ -peak at $T_N \cong 0.63\text{K}$ [94] in specific heat measurements and by the abrupt increase in the *muon longitudinal relaxation rates* when the temperature is decreased toward $T_N \cong 0.75\text{K}$. The experimental data are also in excellent agreement with the theoretical predictions (the theoretical value for the transition temperature obtained through *transfer matrix calculations* is $T_N \cong 0.64\text{K}$).

The second group includes Gd-iPr and Gd-Et compounds: these systems are named *fully frustrated*, because in this case the ratio

General Conclusions

between *nnn* and *nn* interactions exceeds a critical value (see Chapter 5 Par.5.1.3) and the frustration effects are dominant. The latter systems show the complex phase diagram theoretically predicted by J. Villain [29]: at high temperature ($T > T_0$), the systems are in the *paramagnetic phase*; at low temperature ($T < T_N$) a *helical 3D phase* is observed; at intermediate T ($T_N < T < T_0$) the compounds are in a *chiral phase*, where the spins can be described as a collection of corkscrews in the x - y plane turning all clockwise or anticlockwise but with phases randomly distributed. All these predictions have been tested and confirmed by susceptibility, specific heat and μ SR measurements.

In Gd-iPr the two transitions have been clearly evidenced by the two pronounced peaks in the *specific heat* measurements at $T_0 \cong 2.08\text{K}$ [57][93-94][99-100], signalling the *chiral transition*, and at $T_N \cong 39\text{mK}$ [99] where the *helical long range ordered phase* takes place. This peak was attributed to 3D helical order and it was shown that it is not due to a *Schottky-like contribution*. For this sample neither susceptibility ($1.7\text{K} < T < 300\text{K}$ the investigated T -range) nor μ SR muon relaxation rate ($0.04\text{K} < T < 10\text{K}$) (related to two-spin correlation function) showed an anomaly in the whole temperature range investigated as both quantities are insensitive to the chiral phase transition. The limited range of temperature investigated by means of χ and λ measurements, prevented the detection of the 3D helical phase transition at $T_N \sim 39\text{Mk}$. The fact that only the specific heat is able to detect both transition temperatures is justified from a theoretical point of view: in fact only the *four-spin correlation function* probed by specific heat is able to detect, besides the 3D ordered phase, also the chiral transition characterized by randomly distributed phases, while the *spin-pair correlation function*, probed by susceptibility and μ SR measurements, can only detect a long range ordered phase transition.

General Conclusions

In Gd-Et the *Villain's complex phase diagram* [29] was also confirmed by the observation of both peaks in the *specific heat* at $T_0 \cong 2.19\text{K}$ and $T_N \cong 1.88\text{K}$ [101]. As expected for the reasons indicated above, also in this case, neither susceptibility nor μSR detect the chiral phase. On the other hand, the long range ordered magnetic transition at lower temperature was signaled by both *susceptibility* at $T_N \cong 1.87\text{K}$ and μSR at $T_N \cong 1.9\text{K}$.

APPENDIX A

A.1 NMR Pulsed Sequences

In this section the most common NMR pulsed sequences will be described [102-103].

In the entire following discussion the *RF pulse* is supposed to have the shape of a square wave (from transmitter to probe) and the length τ of the RF pulse to be much shorter than relaxation times T_1 and T_2 . In this way, no relaxation of the nuclear system takes place during τ .

A.1.1 T_2 Sequences

As already mentioned (see Chapter 2), the most common procedure to detect a *NMR signal* is the application of $\pi/2$ RF pulse along x' axis of the rotating frame. As a consequence, magnetization \vec{M} entirely lies along y' axis. Since the *receiver coil* is placed in the x - $y \equiv x'$ - y' plane, the observed signal (called *Free Induction Decay*, because spin are free to precess with no RF pulses applied) consists in the intensity of M_{xy} which decays to zero after the occurrence of *transverse decay* with the time constant T_2 . In real systems the measure of T_2 is often not possible with a simple $\pi/2$ pulse, because many factors interfere with the free precession of the spin. This is mainly related to the *inhomogeneity* of the *static magnetic field*. In fact nuclei in different parts of the sample feel different fields due either to the external applied field or to the different dipolar internal fields, varying from site to site, with a total distribution having an average width ΔH_0 . The relationship between T_2 and the effective (shorter, because of inhomogeneity of fields) relaxation

Appendix A

time T_2^* is

$$\frac{1}{T_2^*} = \frac{1}{T_2} + \gamma \frac{\Delta H_0}{2}. \quad (\text{A.1})$$

As a consequence of field inhomogeneity, nuclei precess at different frequencies and tend to dephase with each other faster; for this reason T_2^* is shorter than T_2 .

To measure the intrinsic T_2 an ingenious method was proposed by *Hahn*: pulse sequence used is $\pi/2 - \tau - \pi$. Let's describe step by step the magnetization configuration: $\pi/2$ RF pulse along x'

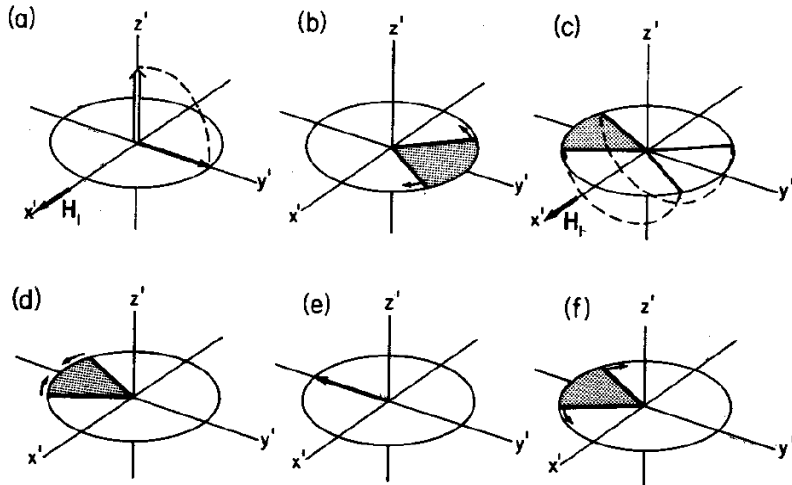


FIG.A.1 Magnetization configurations during Spin Echo Sequence in rotating reference frame [102].

drives magnetization along y' lying in x - y plane; after the time interval τ , during which spins *dephase* progressively, feeling a distribution of magnetic fields $\vec{H}_0 \pm \Delta \vec{H}_0$, another π pulse still

Appendix A

along x' is applied. The result is that spins still stand in the x - $y \equiv x'-y'$ plane but reverse their dephasing thus reconstructing a signal called *echo*.

The magnetization vector will be “built” again to a value decreased by the $(\exp(-2\tau/T_2))$, which takes into account irreversible T_2 decay processes, caused by *spin-spin nuclear interaction*.

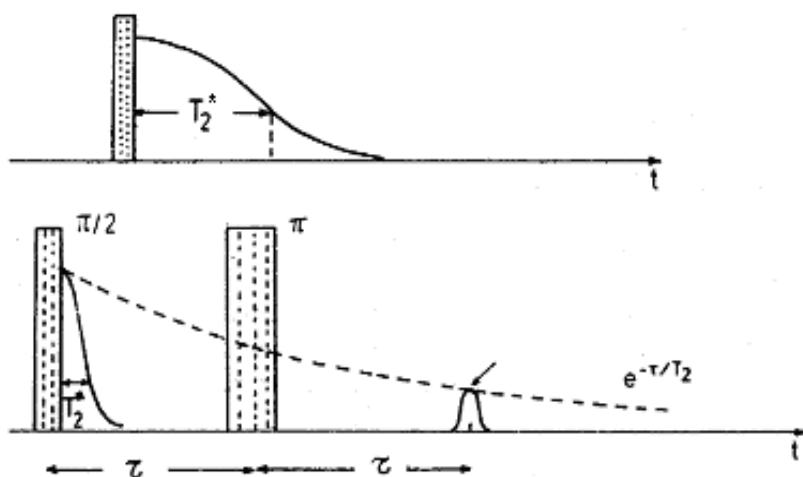


FIG.A.2 Representation of the sequence characterized by $\pi/2$ pulse and the subsequent FID signal (ABOVE) and Hahn Spin-Echo Sequence for evaluation of spin-spin relaxation time with the detection of the “reduced” echo signal (BELOW).

A.1.2 T_1 Sequences

As regards T_1 the most common sequences, used also in this work, are the so called *saturation* and *inversion recovery sequences*.

Appendix A

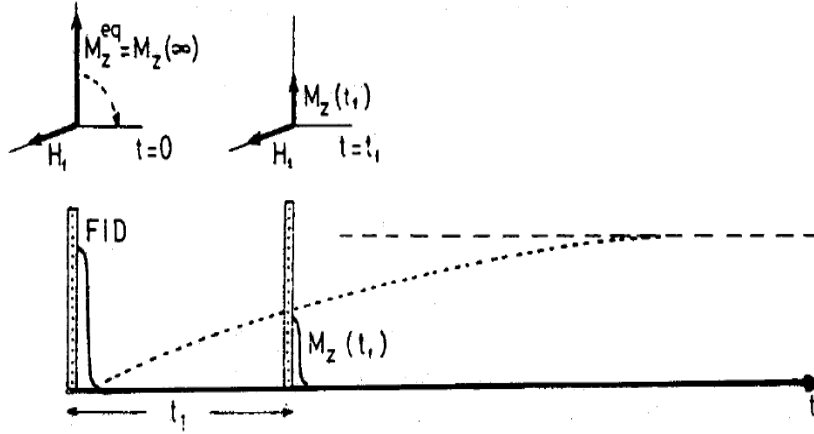


FIG.A.3 Classical Saturation Recovery Sequence for the detection of the longitudinal relaxation time.

In the saturation recovery sequence a $\pi/2$ pulse places the nuclear magnetization in the x' - y' plane and then a *reading sequence* performed at various delays τ from saturation pulse detects the reconstruction of the longitudinal component of $M(t)$; in the inversion recovery, instead, the “reading sequence” follows a π pulse which inverts the magnetization along z direction.

In the data presented in this thesis we have used, instead, a *Hahn echo sequence* ($\pi/2-\pi$ reading pulse) preceded by a *comb of saturation $\pi/2$ pulses*.

The initial comb of $\pi/2$ pulses is applied to have the nuclear spin levels equally populated; in terms of quantum mechanics the temperature of the ensemble of spins is $T = \infty$. As said above, after the comb a delay τ is applied before a $\pi/2-\pi$ Hahn spin-echo. By varying τ , the recovery of the magnetization ($M(\tau)$) towards equilibrium is followed. In the vectorial model, after the comb of $\pi/2$ pulses, the nuclear magnetization stands in x' - y'

Appendix A

plane and, subsequently, the Echo Sequence detects the reconstruction along z axis ($H \parallel z$) of the nuclear magnetization. It should be noticed that in most of the exponential cases of the present thesis, the “reading” pulsed sequence $\pi/2-\pi$ is reduced to a $\pi/2-\pi/2$ one, to maximize the signal. The $\pi/2-\pi/2$ sequence is usually called *solid echo* and it is typically used in *paramagnetic systems*.

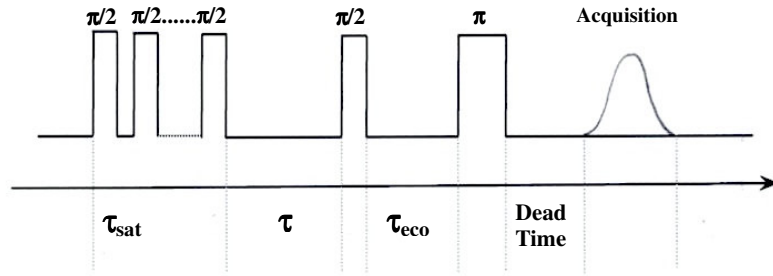


FIG.A.4 Sketch of the pulses in the saturation comb spin-echo sequence used in the T_1 measurements performed in this thesis. τ_{sat} is the time interval between $\pi/2$ saturation pulses, τ is the delay varied for the reconstruction of the longitudinal component of the nuclear magnetization, τ_{eco} is the time interval between the two pulses of the reading sequence and Dead Time is the time between the reading sequence and the acquisition.

APPENDIX B

B.1 NMR Experimental Equipment

B.1.1 NMR Spectrometer

In the current thesis we used a *Fourier Transform-pulsed spectrometer* to perform NMR experiments in the pulsed mode. The spectrometer allowed us to work in the frequency range from 5MHz and 450MHz. Digital pulses are created by a *pulse programmer* connected to a *calculator*, which permits to choose

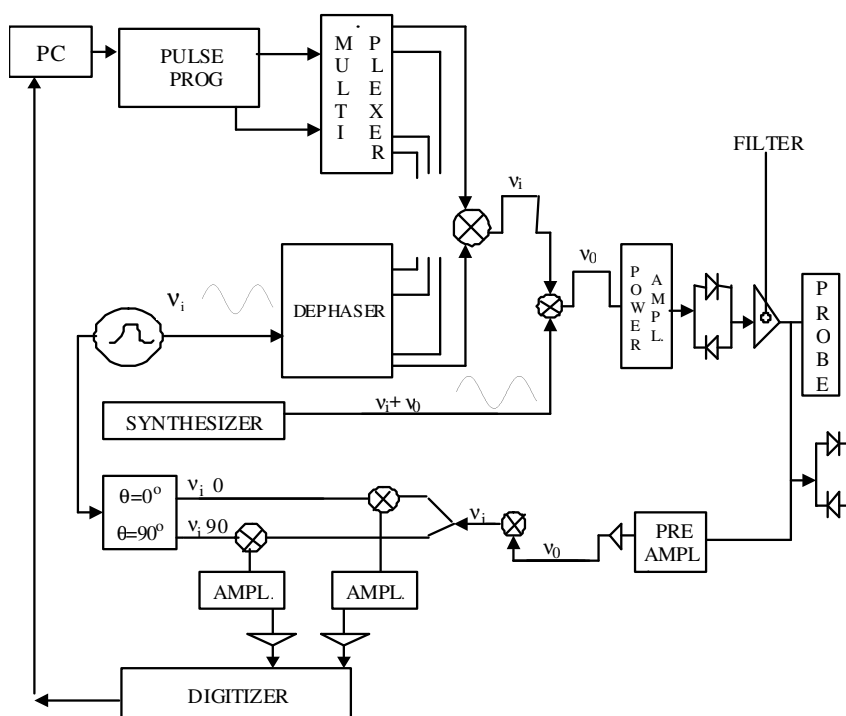


FIG.B.1 Sketch of a pulsed NMR spectrometer

Appendix B

separation and time length of the pulses, and to mix through a *multiplexer*, the generated pulses with one of the four (or more than four) *carrier waves* with different phases. These waves have their own frequency, named ν_i , independent from the frequency of measure: in this way it is not necessary that phases have to be calibrated anytime the measuring frequency is varied.

Radiofrequency pulse of frequency ν_i is mixed with a signal, called *reference signal*, whose frequency is $\nu_i + \nu_0$, being ν_0 the *Larmor frequency*. The resulting signal after passing through a filter which cuts the high frequencies, in this case represented by $\nu_i + 2\nu_0$, has frequency ν_0 (*irradiating frequency*). Before arriving to the probe, pulses are amplified by a *power amplifier* (generally 400W). The process of detection can be summarized as follows: a *diode bridges system* deviates the free precession signal coming from the irradiated nuclei and revealed by the coil, whose frequency is ν_0 , to an *output circuit* where a *preamplifier* is placed. In this way the signal is modulated with the one at $\nu_i + \nu_0$ frequency, split in two different channels and mixed with a frequency reference signal of frequency ν_i with phases $\theta=0^\circ$ in the first channel and $\theta=90^\circ$ in the second one: two *radio signals* in *quadrature* can be obtained. This method allows us to understand if the resonance frequency is higher or lower than ν_0 . The resulting signals have a low intensity, so that they need to be further amplified and filtered finally entering a *digitizer* connected to the calculator. If necessary the phase of the output signal can be alternated before the amplification.

B.1.2 NMR Probe

The *NMR probe* consists in a *RLC resonant circuit*, where L is the *inductance* of the coil surrounding the sample and C the

Appendix B

circuit capacitance controlled through two *variable capacitors*. The NMR probe has to satisfy three fundamental characteristics: (i) the resonant condition $\omega_0 = 1/\sqrt{LC}$; (ii) it has to present an *impedance* matching between the output amplifier and the probe (50Ω), to reduce the reflected wave: for this purpose in parallel to the *LC* circuit, an inductance or one or more capacitances which can be varied are used; (iii) an high *Q-factor* ($Q = R/(\omega_L L)$) requested to maximize the power reaching the coil.

B.1.3 Cryogenic Equipment

The *cryogenic equipment* used in this work for NMR measurements covers a temperature range between 1.5K and 360K. We used two different cryostats depending on the temperature range investigated: a *continuous flow cryostat* and a *bath cryostat*. In the first case, probe is placed inside the cryostat in the uniform static magnetic field and cooled down by direct contact with the *cryogenic liquid* or gas inserted in the same chamber. The thermal exchange between the sample and the environment at room temperature is reduced by a *vacuum jacket* (vacuum pressure of the order of 10^{-6} Torr) adjacent to the sample chamber where a superinsulating material is contained. This material has very low thermal conductivity and with high reflectivity and consists of *multilayers of mylar and aluminium*. The *pump system* is constituted by the combination of a *rotary pre-vacuum pump* and a *turbo-molecular pump* to reach high values of vacuum. The connection between pumps and the components where the vacuum is necessary, is assured by flexible tubes which are highly isolated from the surrounding environment.

In the continuous flow system the pathway of the cryogenic

Appendix B

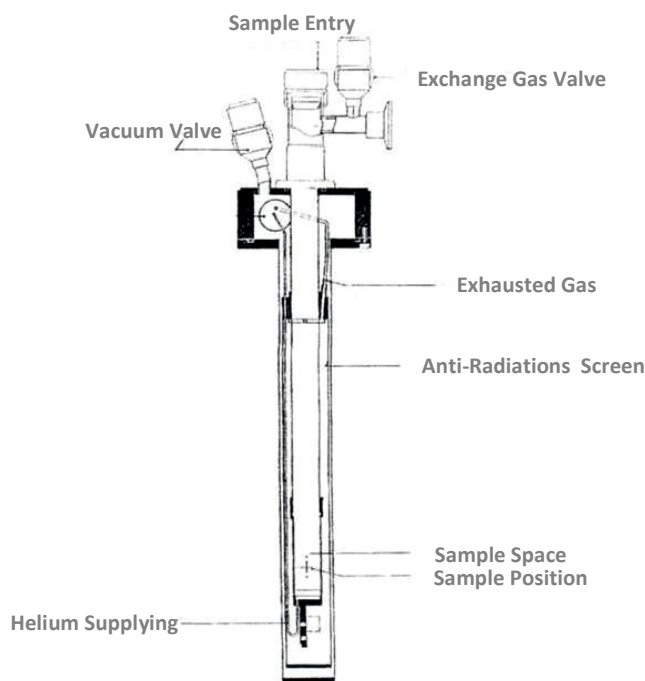


FIG.B.2 Sketch of a continuous flow cryostat used in NMR measurements (Oxford Instruments)

liquid is the following: the liquid contained in a supply *dewar* is picked up by a *transfer tube*, which connects the dewar and the cryostat, containing capillary tubes (thermally insulated by a high vacuum chamber), where the flow passes; then the liquid goes through the sample chamber where it is in contact directly with the sample. The exhaust gas is expelled from the system through a circuit coaxial with respect to the one where the gas is introduced. The circulation of the refrigerating liquid is assured by a pump. The liquid used for cooling the sample varies according to the temperature range to be investigated: *Nitrogen* is used from room temperature to 77.3K; to reach lower

Appendix B

temperatures till 4.2K, instead, *liquid Helium* is necessary. The temperature of the sample is monitored thanks by a *Au-Fe-Chromel thermocouple* whose reference temperature is 77.3K. As a common thermocouple it reads the voltage, displayed by a

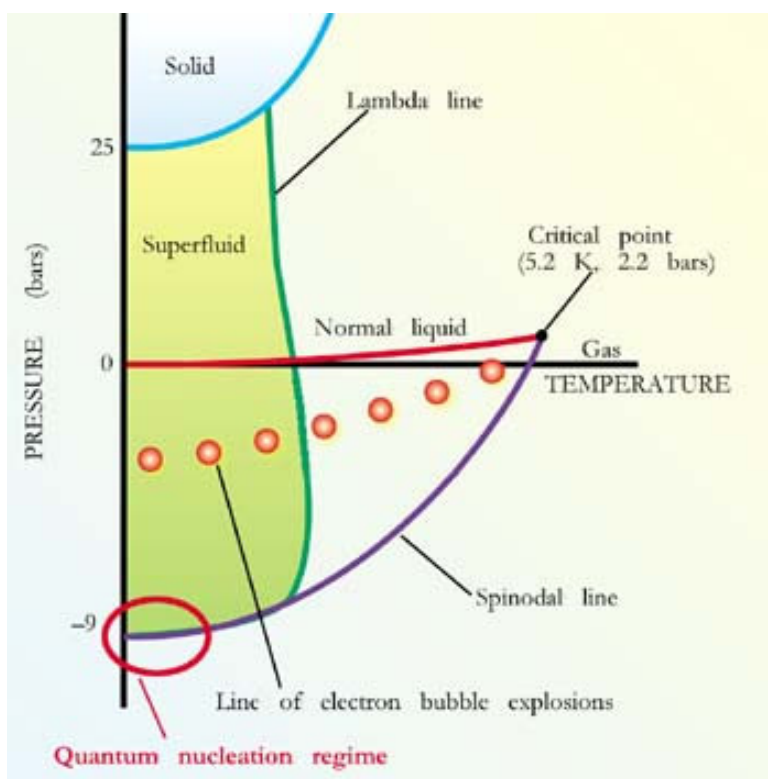


FIG.B.3 Phase diagram of He4 where its characteristics and critical temperatures are shown.

voltmeter and then converted in temperature units using a calibration table. In the sample chamber is also placed the so-called *heat exchanger*, consisting in a resistor which switches on when the refrigerating liquid flow has to be warmed up. The resistor and the heat exchanger are monitored and controlled by

Appendix B

an external *Intelligent Temperature Controller* (ITC) through which the temperature can be set at the desired value. This system allows rapid variations of temperature which can be stabilized with great precision ($\pm 0.05\text{K}$).

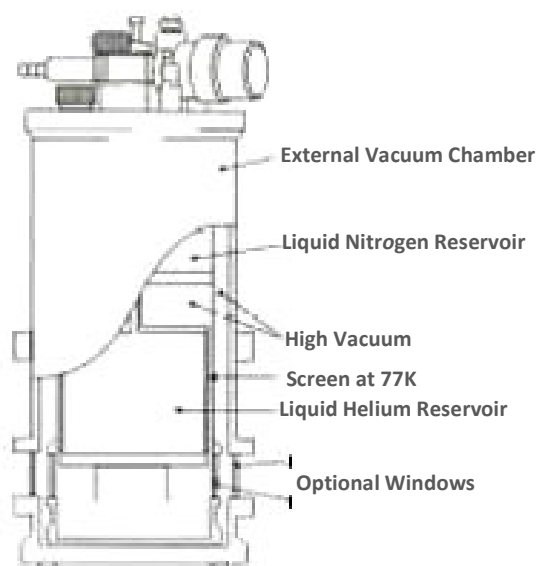


FIG.B.4 Schematic view of the bath cryostat used in NMR measurements (Oxford Instruments).

The *bath cryostat*, instead, works in a different way: it is made up of an internal chamber which must be filled with liquid helium ($T=4.2\text{K}$) where the sample is placed. This chamber is surrounded by a chamber containing liquid Nitrogen at 77K and another external vacuum chamber to “screen” the sample chamber from the external environment. The vacuum chamber contains a superinsulating material composed, also in this case, by foils of mixed mylar and aluminium. To cool down the

Appendix B

sample below 4.2K, a *high vacuum pump* is connected to the main chamber of the cryostat to lower adiabatically the pressure inside the chamber itself. Lowering the pressure over the liquid causes a decrease also of its temperature till values as low as $T \approx 1.5\text{K}$. The real temperature range of work of bath cryostats is 4.4K to 1.5K with a great stability of $\pm 0.01\text{K}$ for several hours.

B.1.4 Field Source Equipment

The static magnetic field used in the NMR experiments was provided by two different devices: an *electromagnet* and a *superconducting magnet*.

The first system is made up of two *field poles* each constituted by *electrical wire coils*. The current flowing in the coils is provided by a current source that rectifies the line AC current to obtain a pure direct current (DC). As well-known from the electromagnetism laws, a direct current produces a static magnetic field in the space between the poles where the sample is placed inside the cryostat.

The electromagnet is supplied by a 60A maximum direct current and 200V voltage. Varying the DC current and depending on the position of the field poles, the electromagnet can produce a maximum static magnetic field of about 2.3Tesla. The field produced is then measured by a *Hall effect gaussmeter*.

To perform higher magnetic field measurements ($H > 2\text{T}$) a *superconducting magnet* was used. It is constituted by a *Cu/NbTi coil* where NbTi alloy is the superconducting component ($T_c \approx 9\text{K}$) while Cu provides stability and protection to the wire and the coil. The coil is placed in a superinsulated chamber full of liquid helium and surrounded by another chamber containing liquid nitrogen for pre-cooling of the internal chamber. The instrument has an external chamber for superinsulation. To vary

Appendix B

the magnetic field, the coil has a small superconductive part that

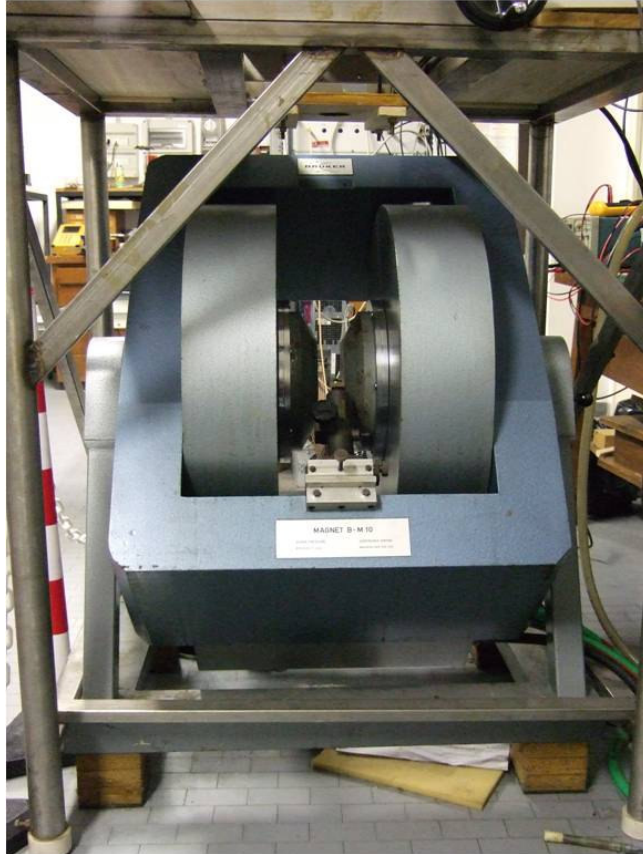


FIG.B.5 The electromagnet used for measurements in the NMR laboratories of the University of Pavia

can be warmed up by a heater, so the superconducting state is destroyed in that region, while the rest of the coil remains superconducting. At the edges of this warmed part, a current source is put inside the coil to reach the desired magnetic field. When the set current value is reached, the heater is turned off and

Appendix B

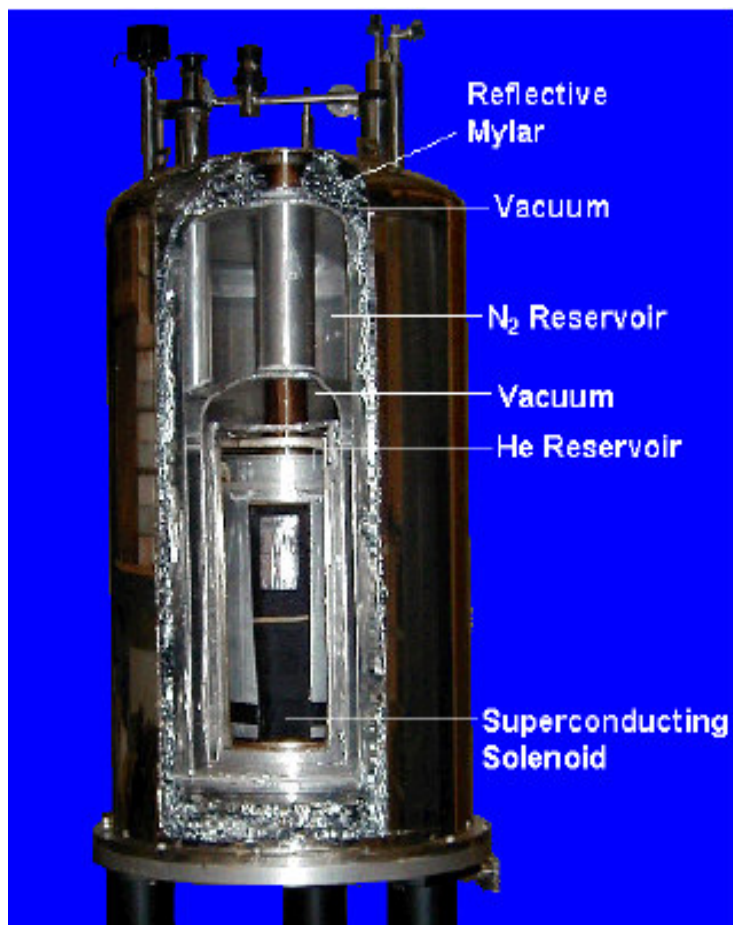


FIG.B.6 Internal view of the device containing the superconducting solenoid for the creation of high static magnetic fields with the indication of the N₂ and He reservoirs for keeping the solenoid in its supeconducting phase.

the coil becomes again entirely superconducting. The ratio between the static magnetic field produced and the current flow inside the coil is 1000Gauss per 1.03A. In fact using a current source reaching 90A, the maximum magnetic field that can be

Appendix B

produced in our laboratory is about 9Tesla.



FIG.B.7 Superconducting magnet used for NMR measurements at high magnetic fields in the NMR laboratory at University of Pavia.

B.2 μ SR Experimental Equipment

B.2.1 Introduction

μ SR measurements presented in this thesis have been performed at RAL (Rutherford Appleton Laboratory) Facility in Chilton, England, and at PSI (Paul Scherrer Institute) in Villigen, Switzerland. In particular at PSI two different equipments have been used depending on the temperature range of investigation: GPS (in the range $1.8\text{K} < T < 300\text{K}$) and LTF ($20\text{mK} < T < 1.8\text{K}$).

In this section we will describe just GPS equipment since the two systems work in a similar way.

B.2.2 Muon Beamline and GPS Instrument

The area of PSI Facility where there is the *beamline* dedicated exclusively to μ SR experiments and where GPS and LTF instruments are placed is called Area π M3 and its sketch can be observed in FIG.B.8.

The *protons beam* hit the target M made up of Berilium and placed at 22.5° with respect to the forward direction, where the muons produced by this collision are directed to π M3 line. They are then driven by a series of magnets, used for various purposes, along the line: the magnets are *quadrupoles*, *bending magnets*, *steering magnets* and *slits*: two of them are always fully open, while the *flow of muons* is controlled by a third slit close to the area of GPS instrument. Along the line, a 3m long *crossed-field separator* can be used either as a muon/electron separator in longitudinal geometry or as a *muon spin rotator* in transverse geometry (spin rotator consists in mutually perpendicular electrical and magnetic fields): in the first case the settings of the

Appendix B

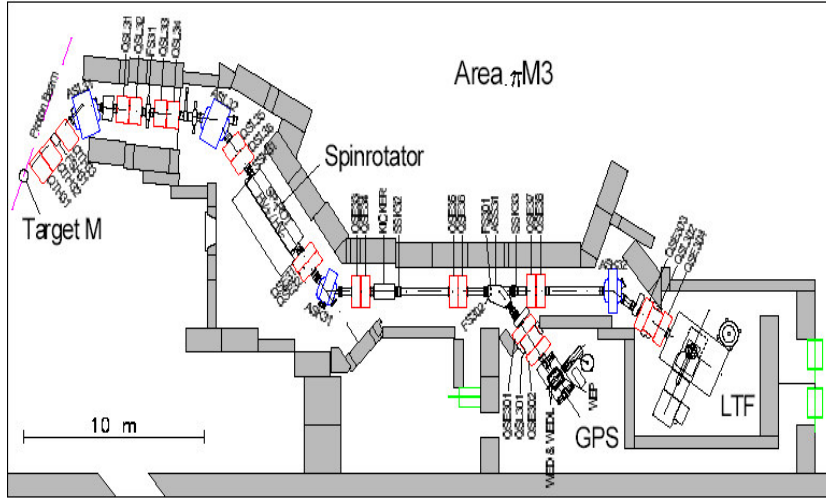


FIG.B.8 Scheme of the beam magnets in area $\pi M3$ from the target to GPS and LTF instruments. QXXNN are quadrupoles, ASXNN are bending magnets, SSKNN are steering magnets and FSNNN are slits.

two fields are correlated so that just muons of chosen velocity are transmitted; in the second case the spin rotator rotates the muon spin upward of about 50° with respect to its original direction. Finally muons reach the GPS instrument where the sample is placed and before impinging on it the muons go through various materials: two mylar windows ($2 \times 4 \mu\text{m}$), a detector made up of a scintillator material whose thickness is of 0.2 mm , two layers of superinsulation (aluminized mylar: $2 \times 10 \mu\text{m}$) and the cryostat titanium window ($10 \mu\text{m}$). The actual amount of material passed through by the muons and their distributions is roughly 130 mg/cm^2 of material, i.e. about 1.33 mm of water, 0.6 mm of silicon etc..

GPS Instrument is placed in area $\pi M3.2$: it is designed for *zero-(ZF)*, *longitudinal-(LF)* and *transverse-field (TF)* μSR experiments. Sample rotation is provided for the study of orientation-dependent effects in single crystals.

Appendix B

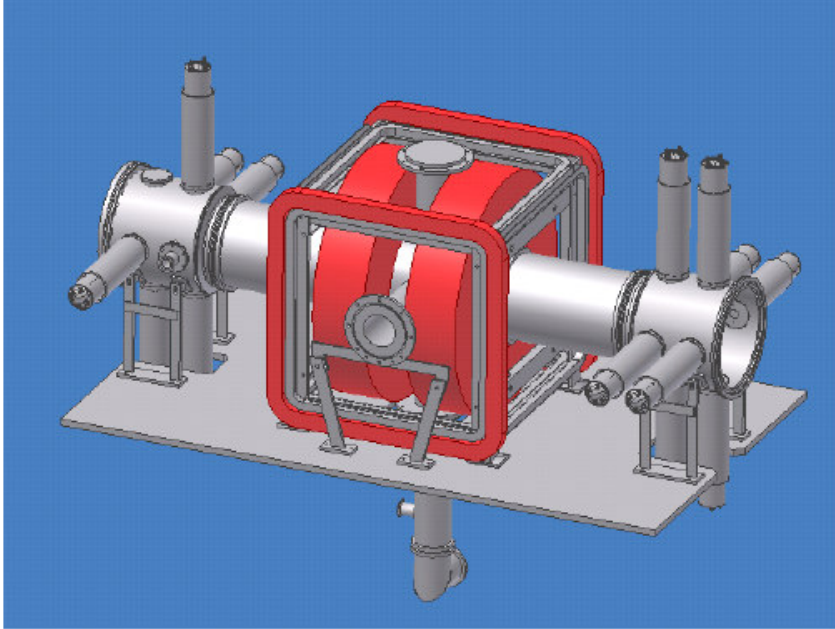


FIG.B.9 3D view of GPS instrument; muons enter from the right-hand side.

The arrangement of the *detectors* consists in:

- 1) a *muon detector* M (see FIG. B.10) of thickness 0.2mm (as already mentioned above) connected to two different photomultipliers
- 2) five *positrons detectors*: Forward (F), Backward (B), Up(U),Down (D), Right (R) with respect to the beam direction
- 3) a *Backward veto detector* (B_{veto}) whose purpose is to collimate the muon beam in a $7 \times 7 \text{ mm}^2$ spot and to reject the muons missing the aperture. It is made up of hollow *scintillators* pyramid ($B_{\text{veto}}^L, B_{\text{veto}}^R, B_{\text{veto}}^U, B_{\text{veto}}^D$) with a

Appendix B

7x7mm² hole facing the M counter.

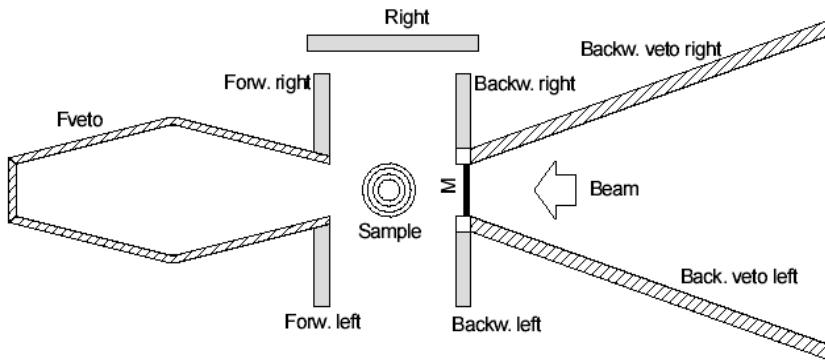


FIG.B.10 Sketch from the top of the main detectors around GPS instrument.

- 4) a *Forward veto detector* (F_{veto}) which rejects muons which have not stopped in the sample: it is mainly used with small samples. In fact for bigger samples, i.e. when all the muons have stopped in the sample, it can be added to the F detector to increase the forward solid angle of detection.

B.2.3 Cryogenic Equipment

For measurements performed at temperatures below room temperature, the QUANTUMCOOLER Continuous Flow Cryostat is used: it utilizes liquid helium as a coolant to provide stable, controllable sample temperature. The system consists of three components:

- 1) The QUANTUM continuous-flow cryostat

Appendix B

- 2) The QUANTUM return vapour-shielded liquid-helium transfer line
- 3) The QUANTUM removable Sample Stick (QUANTUMSTICK)

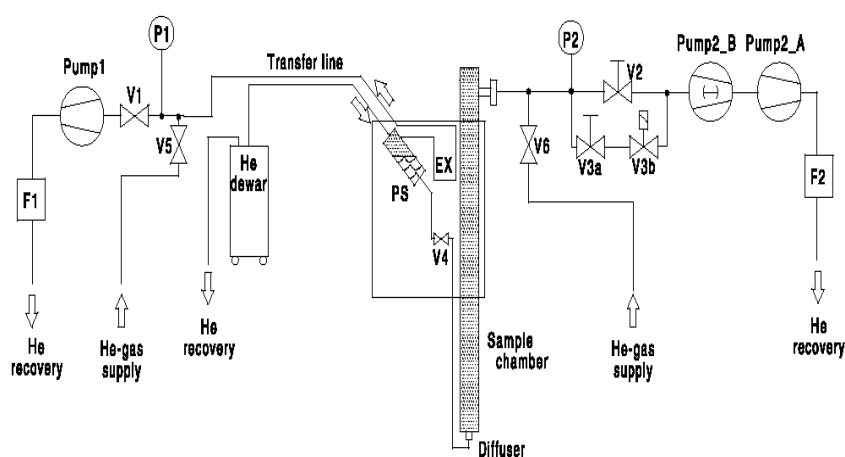


FIG.B.11 Diagram of the Quantum Cryostat used for refrigeration in GPS instrument. EX=Heat Exchanger, F=Flow, P=Pressure, PS=Phase Separator, V=Valve.

The *liquid Helium* flow is drawn from supply *dewar* and goes through the centre of the *transfer line*, enters the first component of the cryostat and the flow is then split in two different directions. The first part of flow enters the top of the *Phase Separator* (PS) and the liquid is expanded through the *needle valve* V4 and then is injected in the sample chamber, with the flow controlled by the *manual valve* V2, the *electromagnetic valve* V3b and the pumps PUMP2_A and PUMP2_B. The second flow enters the top of the Phase Separator, and the gas exiting

Appendix B

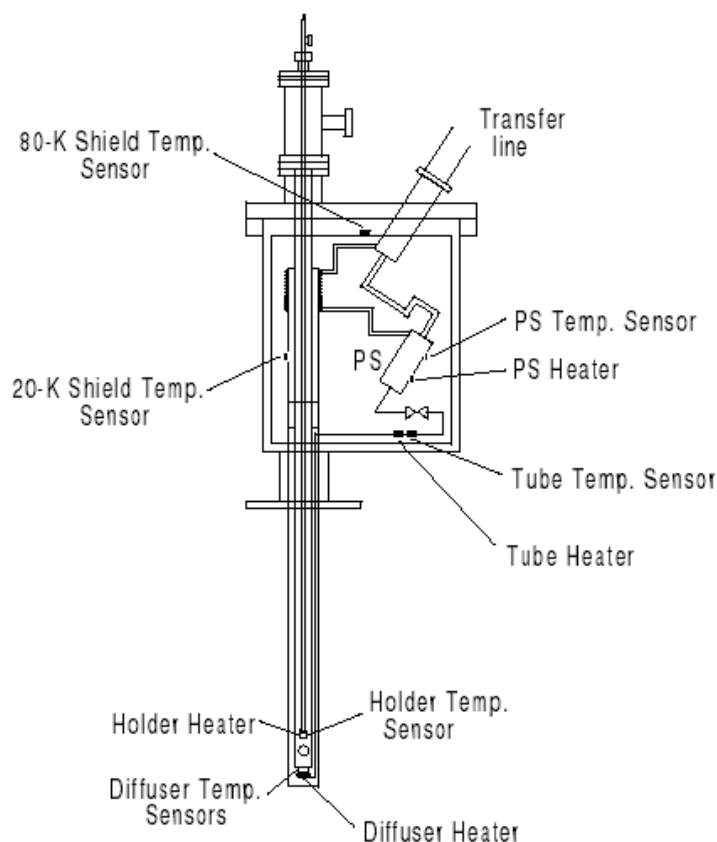


FIG.B.12 Scheme of the temperature heaters and sensors.

from the top of the PS is used to cool the sample chamber and the main *heat shields* (EX). The cold return gas is then used to cool the transfer line shield. In this case the flow is controlled by the valve V1 and the pump PUMP1.

The helium in the Sample Chamber is heated at the set temperature by the *Diffuser Heater* (DH) and its temperature is detected by a *Cernox temperature sensor*. The temperature range of operation of GPS Instrument is $1.8\text{K} < T < 300\text{K}$ which can be

Appendix B

divided into two different ranges ($1.8\text{K} < T < 10\text{K}$ and $5\text{K} < T < 300\text{K}$) where the preliminary setting procedures of the cryogenic equipment are different.

Inside the cryostat is placed the sample which is packed on the sample holder shown in FIG.B.13 and then connected to the probe, which enter the cryostat, with the use of two screws.

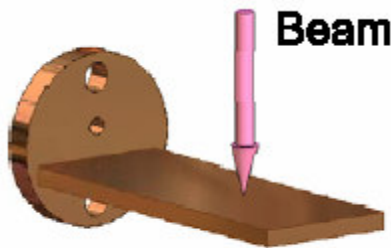


FIG.B.13 Support for the sample in μSR measurements with the indication of the direction of the muon beam.

B.2.4 Magnets in GPS instrument

To generate the magnetic field in the sample zone two sets of *Helmoltz coils* are available:

1a) WED: these coils are used for the production of a magnetic field along muon-beam direction used for both *Longitudinal Field* (where the magnetic field is parallel to the direction of muons polarization) and *Transverse Field studies* when the muon spin is rotated by the Spin Rotator. The magnetic field range with this power supply is $100\text{G} < H < 6.4\text{kG}$.

1b) WEDlow: with the same set of Helholtz coils, magnetic fields lower than 100G can be reached with high stability. The range with this kind of power supply is $T < 450\text{G}$.

Appendix B

2) WEP: this pair of coils produces a horizontal magnetic field perpendicular to the muon-bean direction. In this case the highest field that can be reached is $H=60\text{G}$. This kind of power supply is used for calibration, that is to say to determine the total asymmetry or the parameter alpha.

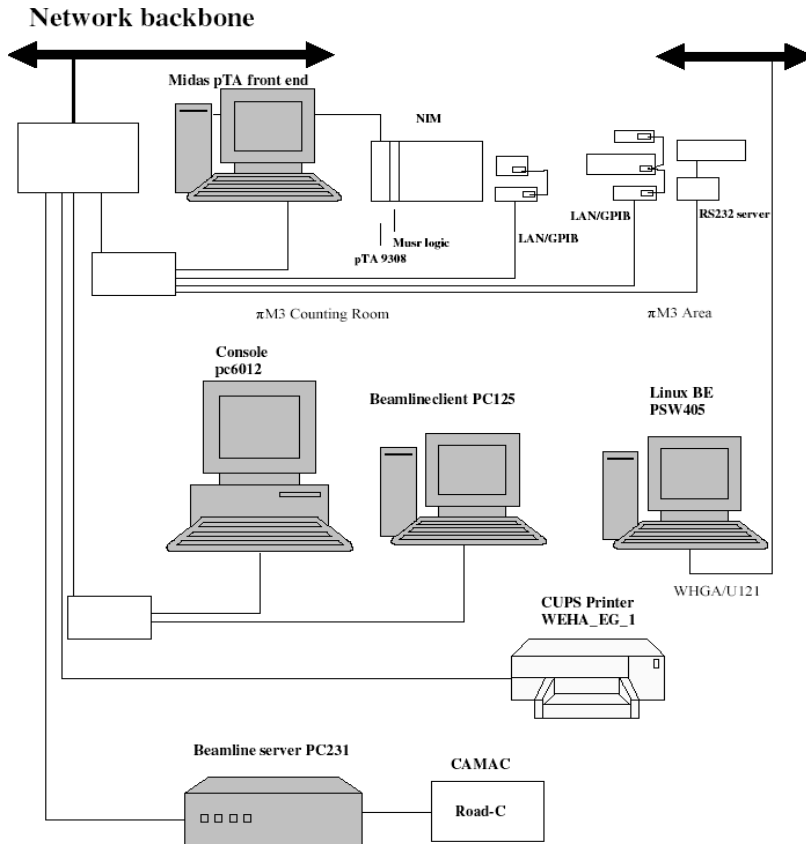


FIG.B.14 Scheme of the interconnections of the various hardware items for GPS instrument.

Appendix B

B.2.5 Computers

The main item is the *Linux console* (pc6012), which is the interface for the *back-end Linux system* (psw405) placed in the WHGA building and which runs the data-acquisition. The core of the electronics is the *pico-second Time Analyser* (pTA 9308-ORTEC) *module* which is connected to a μ SR *logic box* which provides the *pTA module* the appropriate label (“tag”) for a given muon or positron event. The so-called *MIDAS front-end*, which reads out the events and builds the *histograms*, controls the pTA module. Histograms are transferred then to the *back-end workstation* psw405. All the parameters such as temperature, magnetic field and number of events per measurement can be set by this system of computers (see FIG. B.14) directly from *counting room* above GSP experimental area.

Bibliography

- [1] R. J. Glauber, *J. Math. Phys.* 4 294 (1963)
- [2] S. H. Baek, M. Luban, A. Lascialfari, E. Micotti, Y. Furukawa, F. Borsa, J. van Slageren, A. Cornia, *Phys. Rev. B* 70, 134434 (2004)
- [3] P. Santini, S. Carretta, E. Livioti, G. Amoretti, P. Carretta, M. Filibian, A. Lascialfari, E. Micotti, *Phys. Rev. Lett.* 94, 077203 (2005)
- [4] E. Micotti, A. Lascialfari, F. Borsa, M. H. Julien, C. Berthier, M. Horvatić, J. van Slageren, D. Gatteschi, *Phys. Rev. B* 72, 020405 (2005)
- [5] D. Procissi, A. Lascialfari, E. Micotti, M. Bertassi, P. Carretta, Y. Furukawa, P. Kögerler, *Phys. Rev. B* 73, 184417 (2006)
- [6] E. Micotti, Y. Furukawa, K. Kumagai, S. Carretta, A. Lascialfari, F. Borsa, G. A. Timco, R. E. Winpenny, *Phys. Rev. Lett.* 97, 267204 (2006)
- [7] J. Lago, E. Micotti, M. Corti, A. Lascialfari, A. Bianchi, S. Carretta, P. Santini, D. Procissi, S. H. Baek, P. Kögerler, C. Baines, A. Amato *Phys. Rev. B* 76, 064432 (2007)
- [8] R. Sessoli, D. Gatteschi, A. Caneschi, M. A. Novak, *Nature* 365, 141 (1993)
- [9] W. Wernsdorfer, R. Sessoli, *Science* 284, 133 (1999)
- [10] L. Thomas, F. Lioni, R. Ballou, D. Gatteschi, R. Sessoli, B. Barbara, *Nature* 383, 145 (1996)

Bibliography

- [11] J. R. Friedman, M. P. Sarachik, J. Tejada, R. Ziolo, *Phys. Rev. Lett.* 76, 3830 (1996)
- [12] P. M. Richards, *Phys. Rev. Lett.* 28, 1646 (1972)
- [13] D. Hone, C. Scherer, F. Borsa, *Phys. Rev. B* 9, 975 (1974)
- [14] F. Borsa, M. Mali, *Phys. Rev. B* 9, 2215 (1974)
- [15] F. Borsa, J. P. Boucher, J. Villain, *J. Appl. Phys.* 49, 1326 (1978)
- [16] F. Borsa, M. G. Pini, A. Rettori, V. Tognetti, *Phys. Rev. B* 28, 5173 (1983)
- [17] C. Benelli, A. Caneschi, D. Gatteschi, L. Pardi, P. Rey, *Inorg. Chem.* 29, 4223 (1990)
- [18] C. Benelli, A. Caneschi, D. Gatteschi, R. Sessoli, *Adv. Mater.* 4, 504 (1992)
- [19] C. Benelli, A. Caneschi, D. Gatteschi, R. Sessoli, *Inorg. Chem.* 32, 4797 (1993)
- [20] C. Benelli, A. Caneschi, D. Gatteschi, R. Sessoli, *J. Appl. Phys.* 73, 5333 (1993)
- [21] L. Bogani, C. Sangregorio, R. Sessoli, D. Gatteschi, *Angew. Chem. Int. Ed.* 44, 5817 (2005)
- [22] K. Bernot, L. Bogani, A. Caneschi, D. Gatteschi, R. Sessoli, *J. Am. Chem. Soc.* 128, 7947 (2006)
- [23] A. Caneschi, D. Gatteschi, N. Laloti, C. Sangregorio, R. Sessoli, G. Venturi, A. Vindigni, A. Rettori, M. G. Pini, M. A. Novak, *Angew. Chem. Int. Ed.* 40, 1760 (2001)

Bibliography

- [24] D. Gatteschi, R. Sessoli, *Angew. Chem. Int. Ed. Eng.* 42, 268 (2003)
- [25] I. Harada, *J.Phys. Soc. Jap.* 52, 4099 (1983)
- [26] I. Harada, *J.Phys. Soc. Jap.* 53, 1643 (1984)
- [27] I. Harada, H. J. Mikeska, *Z. Phys. B* 72, 391 (1988)
- [28] J. Villain, *J. Phys. (France)* 38, 385 (1977)
- [29] J. Villain in *Chiral Order in Helimagnets*, Proceedings of the 13th IUPAP Conference on Statistical Physics, edited by C. Weil, D. Cabib, C. G. Kuper, I. Riess [*Ann. Isr. Phys. Soc.* 2 565 (1978)]
- [30] C. Kittel, *Introduction to Solid State Physics*, John Wiley et Sons, New York (1966) page 509
- [31] A. Abragam, *Principles of Magnetic Resonance*, Clarendon Press, Oxford (1965)
- [32] A. Rigamonti, *Introduzione alla Struttura della Materia*, La Goliardica Pavese, Pavia (1991)
- [33] N. Bloembergen, E. M. Purcell, R. V. Pound, *Phys. Rev.* 73, 679 (1948)
- [34] T. Moriya, *Prog. Theor. Phys.* 16, 23 (1956)
- [35] T. Moriya, *J.Phys. Soc. Jap.* 18, 516 (1963)
- [36] P. Carretta, PhD. Thesis, *NMR, NQR e μ^+SR in Superconduttori ad Alta T_C e in antiferromagneti Loro Precursori*, University of Pavia, 1992/1993

Bibliography

- [37] D. Wolf, *Spin-Temperature and Nuclear-spin Relaxation Matter – Basic Principles and Applications*, Clarendon Press, Oxford (1979)
- [38] L. B. Okun, *Weak Interaction of Elementary Particles*, Pergamon Press (1965), page63
- [39] A. Schenck , *Muon Spin Rotation Spectroscopy*, Adam Hilger Ltd, Bristol (1985), page9
- [40] N. Papinutto, Laureate Thesis, *Eccitazioni a Bassa Frequenza in Antiferromagneti Planari di Heisenberg $S = 1/2$ Frustrati*, University of Pavia (2001)
- [41] Y. J. Uemura, T. Ymazaki, D. R. Harshman, M. Senba, E. J. Ansaldo, *Phys. Rev. B* 28, 371 (1962)
- [42] S. J. Blundell, *Contemporary Physics* 40, 175 (1999)
- [43] R. Kubo, T. Toyabe, *Magnetic Resonance and Relaxation*, edited by R. Blinc, North Holland, Amsterdam (1967) page810.
- [44] B. Cywinski, *Muon Spin Relaxation Functions*, Training Course in Pulsed Muon Techniques, Lecture Notes (2003)
- [45] T. Moriya, *Prog. Theor. Phys.* 28, 371 (1962)
- [46] P. Carretta, *Scientifica Acta* Vol. VIII, 1 (1993)
- [47] C. J. O'Connor, *Magnetochemistry-Advances in Theory and Experimentation*, Wch.
- [48] F. Borsa, A. Rigamonti, *NMR and NQR in Fluids, Paramagnets and Crystal in Magnetic Resonance at Phase Transitions*, Academic Press, New York (1986)

Bibliography

- [49] P. M. Richards, F. Borsa, *Solid State Comm.* 15, 135 (1974)
- [50] M. E. Fisher, *Am. Jour. Phys.* 32, 343 (1964)
- [51] E. Ising, *Z. Phys* 31, 253 (1925)
- [52] M. Wortis, *Phys. Rev B* 10, 4665 (1974)
- [53] A. Vindigni, Laureate Thesis, University of Firenze (2001)
- [54] M. G. Pini, A. Rettori, *Phys. Rev. B* 76, 069903 (2007)
- [55] M. Blume, P. Heller, N. A. Laurie, *Phys. Rev. B* 11, 4483 (1975)
- [56] G. S. Joyce, *Phys. Rev.* 155, 478 (1967)
- [57] M. Affronte, A. Caneschi, C. Cucci, D. Gatteschi, J. C. Lasjaunias, C. Paulsen, M. G. Pini, A. Rettori, R. Sessoli, *Phys. Rev. B* 59, 6282 (1999)
- [58] M. Mariani, S. Aldrovandi, M. Corti, J. Lago, A. Lascialfari, E. Micotti, A. Rettori, F. Cinti, A. Amato, C. Baines, L. Bogani, A. Caneschi, S.P. Cottrell, D. Gatteschi, *Inorganica Chimica Acta* 360, 3903-3908 (2007)
- [59] E. Coqblin, *The Electronic Structure of Rare-earth Metals and Alloys*, Academic London (1977) pages122-127.
- [60] D. N. Zubarev, *Usp. Fiz. Nauk.* 71, 71 (1960)
- [61] D. N. Zubarev, *Sov. Phys. Usp.* 3, 320 (1960)
- [62] J. Villain, *J. Phys. (France)* 35, 27 (1974)
- [63] D. J. Scalapino, Y. Imry, P. Pincus, *Phys. Rev. B* 11, 2042 (1975)

Bibliography

- [64] H. Kawamura, *J. Phys.Soc. Jap.* 54, 3220 (1985)
- [65] H. Kawamura, *J. Phys.Soc. Jap.* 56, 474 (1987)
- [66] H. Kawamura, *J. Appl. Phys.* 63, 3086 (1988)
- [67] H. Kawamura, *Phys. Rev. B* 38, 4916 (1988)
- [68] H. Kawamura, *J. Phys.: Condens. Matter* 10, 4707 (1998)
- [69] A. Caneschi, D. Gatteschi, P. Rey, R. Sessoli, *Inorg. Chem.* 30, 3936 (1991)
- [70] E. F. Ullmann, J. H. Osiecki, D. G. B. Boobcock, R. Darcy, *J. Am. Chem. Soc.* 108, 900 (1986)
- [71] J. B. Goodenough, *J. Phys. Chem. Solids* 6, 287 (1958)
- [72] J. Kanamori, *J. Phys. Chem. Solids* 10, 87 (1959)
- [73] J. B. Goodenough, *Magnetism and the Chemical Bond*, Interscience, New York (1963)
- [74] G. Venturi, Laureate Thesis, University of Firenze (2001)
- [75] A. Vindigni, Laureate Thesis, University of Firenze (2001)
- [76] A. Caneschi, D. Gatteschi, N. Lalioti, C. Sangregorio, R. Sessoli, A. Vindigni, unpublished results
- [77] E. Micotti, Laureate Thesis, *Risonanza Magnetica Nucleare e Risonanza Muonica in Catene Magnetiche Metallorganiche*, University of Pavia (2001)
- [78] A. Caneschi, D. Gatteschi, N. Lalioti, C. Sangregorio, R. Sessoli, G. Venturi, A. Vindigni, A. Rettori, M. G. Pini, M. A. Novak, *Europhys. Lett.* 58, 771 (2002)

Bibliography

- [79] A. Lascialfari, E. Micotti, S. Aldrovandi, A. Caneschi, D. Gatteschi, *J. Appl. Phys.* 93 8749 (2003)
- [80] E. Micotti, A. Lascialfari, A. Rigamonti, S. Aldrovandi, A. Caneschi, D. Gatteschi, L. Bogani, *J. Magn. Magn. Mat.* 272-276 1087 (2004)
- [81] Y. Furukawa, K. Watanabe, K. Kumagai, Z. H. Jang, A. Lascialfari, F. Borsa, D. Gatteschi, *Phys. Rev. B* 62, 14246 (2000)
- [82] Y. Furukawa, K. Kumagai, A. Lascialfari, S. Aldrovandi, F. Borsa, R. Sessoli, D. Gatteschi, *Phys. Rev. B* 64, 094439 (2001)
- [83] L. Bogani, A. Caneschi, M. Fedi, D. Gatteschi, M. Massi, M. A. Novak, M. G. Pini, A. Rettori, R. Sessoli, A. Vindigni, *Phys. Rev. Lett.* 92 207204 (2004)
- [84] L. Bogani, R. Sessoli, M. G. Pini, A. Rettori, M. A. Novak, P. Rosa, M. Massi, M. E. Fedi, L. Giuntini, A. Caneschi, D. Gatteschi, *Phys. Rev. B* 72 064406 (2005)
- [85] M. Massi et al., *Nucl. Instrum. Methods Phys. Res. Sect. B* 190, 276 (2002)
- [86] A. Vindigni, L. Bogani, D. Gatteschi, R. Sessoli, A. Rettori, M. A. Novak, *J. Magn. Magn. Mat.* 272-276 297 (2004)
- [87] A. Vindigni, A. Rettori, L. Bogani, A. Caneschi, D. Gatteschi, R. Sessoli, M. A. Novak, *Appl. Phys. Lett.* 87 073102 (2005)
- [88] J. K. L. da Silva, A. G. Moreira, M. Silverio Soares, F. C. Sà Barreto, *Phys. Rev. E* 53, 4527 (1995)

Bibliography

- [89] J. H. Luscombe, M. Luban, J. P. Reynolds, *Phys. Rev. E* 53, 5852 (1996)
- [90] C. P. Slichter, *Principles of Magnetic Resonance*, Springer, Berlin (1992)
- [91] A. Caneschi, D. Gatteschi, P. Rey, R. Sessoli, *Inorg. Chem.* 27 1756 (1988)
- [92] C. Benelli, A. Caneschi, D. Gatteschi, L. Pardi, P. Rey, *Inorg. Chem.* 28 275 (1989)
- [93] F. Bartolomé, J. Bartolomé, C. Benelli, A. Caneschi, D. Gatteschi, C. Paulsen, M. G. Pini, A. Rettori, R. Sessoli, Y. Volokitin, *Phys. Rev. Lett.* 77 382 (1996)
- [94] F. Cinti, M. Affronte, A. Lascialfari, M. Barucci, E. Olivieri, E. Pasca, A. Rettori, L. Risegari, G. Ventura, M. G. Pini, A. Cuccoli, T. Roscilde, A. Caneschi, D. Gatteschi, D. Rovai, *Polyhedron* 24 2568 (2005)
- [95] C. Benelli, R. Sessoli, D. Gatteschi, A. Rettori, M. G. Pini, J. Bartolomé, F. Bartolomé, *J. Magn. Magn. Mat.* 140-144, 1649 (1995)
- [96] B. Carazza, E. Rastelli, A. Tassi, *Z. Phys. B* 84, 301 (1991)
- [97] C. Cucci, Laureate Thesis University of Firenze (1996)
- [98] Cinti, PhD Thesis, University of Modena (2003)
- [99] F. Cinti, A. Rettori, M. Barucci, E. Olivieri, L. Risegari, G. Ventura, A. Caneschi, D. Gatteschi, D. Rovai, M. G. Pini, M. Affronte, M. Mariani, A. Lascialfari, *J. Magn. Magn. Mat.* 310 1460 (2007)

Bibliography

- [100] A. Lascialfari, R. Ullu, M. Affronte, F. Cinti, A. Caneschi, D. Gatteschi, D. Rovai, M. G. Pini, A. Rettori, *Phys. Rev. B* 67 224408 (2003)
- [101] F. Cinti, A. Rettori, M. G. Pini, M. Mariani, E. Micotti, A. Lascialfari, N. Papinutto, A. Amato, A. Caneschi, D. Gatteschi, M. Affronte, submitted to *Phys. Rev. Lett.*
- [102] see for instance T. C. Farrar, E. Becker, *Pulse and Fourier Transform NMR-Introduction to Theory and Methods*, Academic Press New York (1971)
- [103] see for instance P. T. Callaghan, *Principles of Nuclear Magnetic Resonance Microscopy*, Clarendon Press (2004)

Acknowledgements

First of all I would like to thank my Supervisor, Prof. F. Borsa, for the useful discussions and suggestions during the analysis of the experimental results and during the draft of this work and Prof. A. Rettori for accepting to be my Referee: thanks to their experience they have helped me to make this thesis a better work. Thank you also to Prof. A. Lascialfari who has played a fundamental role in addressing and organizing my research when Prof. Borsa was not in Pavia and in correcting this thesis: “Thank you very much Alessandro!”. I’m grateful to Prof. M. Corti, to S. Aldrovandi and to Prof. P. Carretta for the help during the work in laboratory. A special thank to Prof. A. Caneschi for the synthesis of the samples, to Dr. L. Bogani for scientific discussions, to Dr. J. Lago and to my colleague, Dr. E. Bernardi, to help me respectively in μ SR and susceptibility measurements and all the other colleagues of the office: Marta, Edoardo, Nico, Francesca and Moreno. I cannot forget all the friends who have shared this piece of life with me: Stefano, Massimiliano, Ilaria, Marco G., Simone, Gemi, Massimo, Enrico, Mara, Angela, Federico, Concetta, Marco P., Davide. A special thank to Cristina, who I have known at the beginning of this adventure and that is a person I care for very much, even if, maybe, we are not so close as we were some time ago. And now I would like to thank once more the people this work is dedicated to: thanks to my parents who love me and who have always helped me in this new experience, in good periods as well as in the darkest ones and thanks to my brother Simone who has supported me in his way and because “my brother is always my brother!”...”I love you!”. And thank you from the bottom of my heart to Linda: “You are the best friend I have ever had, the most incredible person I have ever met; thank you for loving me, for caring for me and for supporting me everyday our special feeling is the

Acknowledgements

bridge that joins me to you across the ocean ... I love you!".

Ringraziamenti

Innanzitutto vorrei ringraziare il mio tutore, il Prof. F. Borsa, per le utili discussioni e i suggerimenti durante l'analisi dei risultati sperimentali e la redazione di questo lavoro e il Prof. A. Rettori per aver accettato di essere il mio supervisore esterno: grazie alla loro esperienza mi hanno aiutato a rendere questa tesi un lavoro migliore. Grazie anche al Prof. A. Lascialfari che ha giocato un ruolo fondamentale nell'indirizzare e nell'organizzare la mia ricerca quando il Prof. Borsa non era qui a Pavia e nel correggere questa tesi: "Grazie mille Alessandro!". Sono grato al Prof. M. Corti, a S. Aldrovandi e al Prof. P. Carretta per l'aiuto datomi durante il lavoro in laboratorio. Un ringraziamento speciale va al Prof. A. Caneschi per la sintesi dei campioni, al Dott. L. Bogani per le discussioni di carattere scientifico, al Dott. J. Lago ed al mio collega, il Dott. E. Bernardi, per avermi aiutato rispettivamente nelle misure di μ SR e di suscettività e a tutti gli altri colleghi dell'ufficio: Marta, Edoardo, Nico, Francesca e Moreno. Non posso dimenticare tutti gli amici che hanno condiviso con me questo periodo della mia vita: Stefano, Massimiliano, Ilaria, Marco G., Simone, Gemi, Massimo, Enrico, Mara, Angela, Federico, Concetta, Marco P., Davide. Un grazie speciale a Cristina che ho conosciuto all'inizio di questa avventura e che è una persona a cui tengo molto, anche se forse non siamo più così vicini come eravamo un po' di tempo fa. E ora vorrei ringraziare ancora una volta le persone a cui è dedicata questa tesi: grazie ai miei genitori che mi vogliono bene e che mi hanno sempre aiutato durante questa nuova esperienza, nei periodi positivi così come nei momenti più bui e grazie a mio fratello Simone che mi ha supportato a suo modo e perché "mio fratello è sempre mio fratello!"... "Vi voglio bene!". E grazie dal profondo del mio cuore a Linda: "Tu sei la migliore amica che io abbia mai avuto, la persona più incredibile che io abbia mai conosciuto;

Ringraziamenti

grazie perché mi vuoi bene, perché ci tieni a me e perché mi sostieni ogni giorno ... il nostro feeling speciale è il ponte che ci unisce sull'oceano ... ti voglio bene!"